Aus dem Institut für Physiologie und Pathophysiologie

Geschäftsführender Direktor: Prof. Dr. Dominik Oliver

des Fachbereichs Medizin der Philipps-Universität Marburg

The coincidence biosensor tubbyCT reveals local phosphatidylinositol-4,5-bisphosphate synthesis at endoplasmic reticulum-plasma membrane junctions

Inaugural-Dissertation zur Erlangung des Doktorgrades der Naturwissenschaften

dem Fachbereich Medizin der Philipps-Universität Marburg

vorgelegt von

Veronika Katharina Thallmair

aus München, Deutschland

Marburg, 2020

Angenommen vom Fachbereich Medizin

der Philipps-Universität Marburg

am: 19.10.2020

Gedruckt mit Genehmigung des Fachbereichs

Dekan i.V. der Prodekan: Herr Prof. Dr. R. Müller

Referent: Herr Prof. Dr. D. Oliver

1. Korreferent: Herr Prof. Dr. R. Jacob

Table of contents

ABBREVIATIONS.....5
ABSTRACT.....9
ZUSAMMENFASSUNG.....10
1 Introduction.....12
1.1 Cellular Membranes.....12
1.2 Phosphoinositides.....13
1.2.1 Phosphatidylinositol-4-phosphate.....14
1.2.2 Phosphatidylinositol-4,5-bisphosphate.....15
1.2.3 The PI cycle.....16
1.3 Membrane contact sites.....17
1.4 ER-PM junctions.....18
1.4.1 The role of ER-PM junctions in lipid homeostasis.....19
1.4.2 Extended Synaptotagmin-mediated and Nir-containing ER-PM junctions. .22
1.4.2.1 Extended Synaptotagmins.....23
1.4.2.2 Nir proteins.....25
1.4.2.3 VAMP-associated proteins.....27
1.5 Phosphoinositide binding domains.....28
1.5.1 The PI(4,5)P_2 sensor PLCδ1-PH.....28
1.5.2 The PI(4,5)P_2 sensor tubbyCT.....29
1.6 Aim of the study.....31
2 Methods.....33
2.1 Cell culture.....33
2.2 Molecular biology.....33
2.3 Detection of gene expression at mRNA level.....38
2.3.1 RNA extraction.....38
2.3.2 Reverse transcription polymerase chain reaction.....39
2.4 Co-immunoprecipitation.....42
2.4.1 Protein extraction and complex precipitation.....42
2.4.2 SDS-PAGE and Western Blot.....43
2.4.3 Quantification of co-immunoprecipitation.....44

2.5 Fluorescence Resonance Energy Transfer.....45
2.5.1 Experimental Set-up.....46
2.5.2 Background, bleed through and false excitation correction.....46
2.6 Total Internal Reflection Fluorescence Microscopy.....49
2.7 Plasma membrane protein cluster detection.....51
2.8 Chemicals.....53
2.9 Data analysis.....53
3 Results.....55
3.1 TubbyCT and PLCδ1-PH do not target mutually exclusive PI(4,5)P_2 pools.....55
3.2 TubbyCT clusters at the PM and shows PLCβ-induced PM recruitment.....57
3.3 TubbyCT recruitment occurs at regions with strong clustering.....60
3.4 TubbyCT membrane recruitment is DAG-independent and PI(4,5)P_2-dependent63
3.5 TubbyCT localizes to E-Syt3-rich ER-PM junctions.....65
3.5.1 TubbyCT co-localizes with the ER-PM junction protein E-Syt3.....65
3.5.2 TubbyCT is recruited to ER-PM junctions via interaction with E-Syt3.....69
3.5.3 Mapping the molecular interaction interface between tubbyCT and E-Syt3 73
3.6 Coincidence detection of E-Syt3 and PI(4,5)P_2 determines tubbyCT localization to ER-PM junctions.....76
3.7 TubbyCT recruitment reflects PLCβ-induced PI(4,5)P_2 synthesis at ER-PM junctions.....80
3.8 PI4P dynamics at ER-PM junctions do not differ from dynamics in the bulk PM 82
3.9 Local PI(4,5)P_2 increase during global PI(4,5)P_2 depletion maintains functionality of ER-PM junctions.....83
3.10 Study of diverging tubbyCT dynamics in CHO and COS-7 cells.....84
3.10.1 E-Syt dynamics in CHO and COS-7 cells.....85
3.10.2 Expression levels of ER-PM junctional proteins in CHO and COS-7 cells 88
3.10.3 Influence of E-Syt3 over-expression on tubbyCT dynamics.....88
3.10.4 Influence of Nir over-expression on tubbyCT localization and dynamics..90
3.11 Localization of tubby-like proteins to E-Syt3-rich ER-PM junctions.....91

4 Discussion.....95
4.1 Functionally distinct and spatially separated PI(4,5)P_2 pools.....95
4.2 Local synthesis of PI(4,5)P_2 at ER-PM junctions.....96
4.3 PI(4,5)P_2 content at ER-PM junctions.....98
4.4 Function of junctional PI(4,5)P_2 pools.....99
4.5 Existence of different types of E-Syt-tethered ER-PM junctions.....100
4.6 Cell type-dependent junctional recruitment of tubbyCT.....101
4.7 TubbyCT as junctional PI(4,5)P_2 pool-specific sensor.....102
4.8 Function of tubby and TULPs at ER-PM junctions.....104
4.9 Outlook.....105
5 References.....107
FIGURES.....118
TABLES.....120
DANKSAGUNG.....121
LEBENSLAUF.....122
PUBLIKATIONEN.....123
VERZEICHNIS DER AKADEMISCHEN LEHRER.....124
EHRENWÖRTLICHE ERKLÄRUNG.....125

ABBREVIATIONS

aa	amino acid
A_T	annealing temperature
AER	Acceptor Excitation Ratio
α-MSH	α-melanocyte-stimulating hormone
CCD	charge-coupled device
cDNA	complementary deoxyribonucleic acid
CDP-DAG	cytidine diphosphate diacylglycerol
CDS	CDP-DAG synthase
CFP	cyan fluorescent protein
CHO	Chinese Hamster Ovary
Co-IP	co-immunoprecipitation
COS	CV-1 in Origin, carrying SV40
CRAC	Ca^{2+}-release activated Ca^{2+}
DAG	diacylglycerol
DER	Donor Excitation Ratio
DGBL	diacylglycerol-binding like
DiC8	1,2-Dioctanoyl-sn-glycerol
DMEM	Dulbecco's Modified Eagle's Medium
DMSO	dimethyl sulfoxide
DNA	deoxyribonucleic acid
dNTPs	deoxynucleoside triphosphate
DTT	dithiothreitol
E-Syt	Extended Synaptotagmin
e.g.	exempli gratia
EDTA	ethylenediaminetetraacetic acid
EGFP	enhanced green fluorescent protein
ENTH	epsin N-terminal homology
ER	endoplasmic reticulum
E_{time}	elongation time

FERM	4.1/ezrin/radixin/moesin
FFAT	two phenylalanines in an acidic tract
For	forward primer
FRB	FKBP Rapamycin Binding
FRET	Fluorescence Resonance Energy Transfer
FYVE	Fab1, YOTB, Vac1, EEA1
GAPDH	glyceraldehyde 3-phosphate dehydrogenase
GFP	green fluorescent protein
GPCR	G protein-coupled receptor
GRAM	Rab-like GTPase activators and myotubularins
GTP	green fluorescent protein
HEPES	4-(2-hydroxyethyl)-1-piperazineethanesulfonic acid
HP	hairpin
i.e.	id est – that is
$I(1,4,5)P_3$	inositol-(1,4,5)-trisphosphate
IFT-A	intraflagellar transport complex A
INPP4B	Inositol Polyphosphate-4-Phosphatase Type II B
IQGAP1	IQ-motif-containing GTPase-activating protein 1
LAM	lipid transfer protein anchored at a membrane contact site
LB	lysogeny broth
LNS2	Lipin/Ned1/Smp2 domain
LS	Lea Schultz
LTP	lipid transfer protein
M1R	muscarinic receptor 1
MCS	membrane contact sites
MDCK	Madin-Darby Canine Kidney
MEM	Minimum Essential Media
mRNA	messenger ribonucleic acid
MSP	major sperm protein
nFor	nested forward primer
Nir	PYK2 N-terminal domain-interacting receptor
nRev	nested reverse primer

OK	Opossum Kidney
Orai	Ca^{2+} release-activated Ca^{2+} modulator
ORP	OSBP-related protein
OSBP	oxysterol-binding protein
Oxo-M	oxotremorine-M
PA	phosphatidic acid
PAGE	Polyacrylamide Gel Electrophoresis
PAO	phenylarsine oxide
PBS	Phosphate-buffered saline
PBST	phosphate-buffered saline with Tween®
PCR	Polymerase chain reaction
PH	Pleckstrin Homology
PI	phosphatidylinositol
$PI(3,4,5)P_3$	phosphatidylinositol-(3,4,5)-trisphosphate
$PI(3,4)P_2$	phosphatidylinositol-(3,4)-bisphosphate
$PI(4,5)P_2$	phosphatidylinositol-(4,5)-bisphosphate
PI3K	phosphatidylinositol 3-kinase
PI3P	phosphatidylinositol-3-phosphate
PI4K	phosphatiylinositol 4-kinase
PI4P	phosphatdylinositol-4-phosphate
PIP5K	phosphatdylinositol-4-phosphate 5-kinase
PIS	phosphatidylinositol synthase
PITD	phosphatidylinositol transfer domain
PITP	phosphatidylinositol transfer protein
PKC	protein kinase C
PLCβ	phospholipase C-β
PM	plasma membrane
POMC	pro-opiomelanocortin
PS	phosphatidylserine
rdgB	retinal degradation B gene
Rev	reverse primer
RFP	red fluorescent protein

RNA	Ribonucleic acid
ROI	region of interest
RT-PCR	Reverse transcription polymerase chain reaction
SDS	Sodium dodecyl sulfate
SEM	standard error of the mean
SHIP	Src homology 2 (SH2) domain containing inositol polyphosphate 5-phosphatase
SMP	synaptotagmin-like mitochondrial lipid-binding protein
SNARE	SNAP receptor
SOC	Super Optimal broth with Catabolite repression
SOCE	store-operated Ca^{2+} entry
StART	StAR-related lipid transfer
STIM	stromal interaction molecule 1
TIRF	Total Internal Reflection Fluorescence
T_M	melting temperature
TMEM	transmembrane protein
Tris	tris(hydroxymethyl)aminomethane
TTC7	tetratricopeptide repeat protein 7
tubbyCT	C-terminal domain of tubby
TULIP	tubular lipid-binding
TULP	tubby-like protein
VAMP	Vesicle associated membrane protein
VAP	VAMP-associated protein
VSP	voltage-sensitive phosphatase
VT	Veronika Thallmair
YFP	yellow fluorescent protein

ABSTRACT

Phosphatidylinositol-4,5-bisphosphate ($PI(4,5)P_2$) plays a prominent role in plasma membrane (PM) physiology. It is implicated in the regulation of a variety of cellular functions including exo- and endocytosis, cytoskeleton anchorage, and ion channel activity. Activation of Gq-coupled receptors induces rapid break-down of $PI(4,5)P_2$ by PLCβ. The thereby generated second messengers $I(1,4,5)P_3$ and diacylglycerol (DAG), in turn also stimulate the resynthesis of $PI(4,5)P_2$. Because its precursor phosphytidylinositol (PI) is synthesized in the endoplasmic reticulum (ER), PI transport to the PM is an essential step in replenishment of $PI(4,5)P_2$. This transport has recently been shown to occur by a non-vesicular mechanism at highly specialized contact sites between both membranes, the ER-PM junctions. These membrane contact sites are mediated by membrane tethering proteins, including the Extended Synaptotagmins (E-Syts) and tightened upon intracellular Ca^{2+} rise, allowing PI transfer to occur.

In my work, I discovered the preferential localization of tubbyCT, a known $PI(4,5)P_2$ recognition domain, to E-Syt3-rich ER-PM junctions. Junctional recruitment is mediated by coincidence detection of E-Syt3 and $PI(4,5)P_2$, as shown by co-localization experiments, co-immunoprecipitations and manipulations of PM $PI(4,5)P_2$ content. These dual binding properties allowed, for the first time, the selective investigation of local $PI(4,5)P_2$ dynamics at ER-PM junctions. Using Total Internal Reflection Fluorescence (TIRF) microscopy, TubbyCT revealed the unexpected increase of a local $PI(4,5)P_2$ pool at ER-PM junctions, that was dependent on local synthesis, despite concurrent global $PI(4,5)P_2$ consumption by PLCβ. Pharmacological inhibition of $PI(4,5)P_2$ resynthesis revealed that these local $PI(4,5)P_2$ pool dynamics are required for maintenance and tightening of ER-PM contact sites during PLCβ signaling. Together, my data suggest a model of local metabolic turnover of locally supplied PI, i.e. ‘metabolic channeling’ of $PI(4,5)P_2$ production in the PM.

Enrichment at ER-PM contact sites was not restricted to the isolated tubby domain, but was likewise observed with the full-length tubby protein and its close relative TULP3. So far, tubby-like proteins (TULPs) have been implicated in delivery of G protein-coupled receptors to primary cilia. My findings suggest an additional role of TULP proteins at ER-PM junctions not previously recognized.

ZUSAMMENFASSUNG

Phosphatidylinositol-4,5-bisphosphat ($PI(4,5)P_2$) ist ein essentielles Signallipid der Plasmamembran (PM) und in viele biologische Prozesse involviert. So spielt es beispielsweise eine wichtige Rolle bei Endo- und Exozytose, bei der Verankerung des Zytoskeletts an der Membran, sowie bei der Regulierung von Ionenkanälen. Die Aktivierung von Gq-gekoppelten Rezeptoren führt zum schnellen Abbau von $PI(4,5)P_2$ durch die Phospholipase C-β (PLCβ), jedoch bedingen die dabei anfallenden sekundären Botenstoffe $I(1,4,5)P_3$ und Diacylglycerin (DAG) auch eine zeitnahe $PI(4,5)P_2$ Resynthese. $PI(4,5)P_2$ wird durch Phosphorylierung aus Phosphatidylinositol (PI) gebildet, welches aus dem ER stammt und die PM durch nicht-vesikulären Lipidtransport erreicht. Dieser PI Transfer stellt einen essentiellen Schritt der $PI(4,5)P_2$ Resynthese dar. Er findet an sogenannten ER-PM Junctions statt, hochspezialisierten Domänen, an denen die ER Membran über Proteine wie beispielsweise die Extended Synaptotagmins (E-Syts) mit der PM verbunden ist. Ein Anstieg an intrazellulärem Ca^{2+}, hervorgerufen zum Beispiel durch Aktivierung der PLCβ, führt zu einem verminderten Abstand der beiden Membranen, was letztendlich den PI Transfer ermöglicht.

In der vorliegenden Arbeit habe ich die bevorzugte Assoziation des bekannten $PI(4,5)P_2$ Sensors TubbyCT mit E-Syt3-enthaltenden ER-PM Junctions herausgefunden. Die Rekrutierung von TubbyCT an die ER-PM Junctions erfolgt durch Koinzidenz-Bindung an E-Syt3 und $PI(4,5)P_2$, was ich unter anderem durch Kolokalisationsexperimente, Ko-Immunpräzipitationen und Manipulationen des $PI(4,5)P_2$ Gehalts der PM gezeigt habe. Aufgrund der Koinzidenz-Bindungseigenschaften von TubbyCT eignet sich der Sensor zur Messung lokaler $PI(4,5)P_2$ Dynamiken an ER-PM Junctions. So konnte zum ersten Mal, mittels Interner Totalreflexionsfluoreszenz (TIRF) Mikroskopie des fluoreszenzmarkierten TubbyCT, eine lokale Produktion von $PI(4,5)P_2$ an ER-PM Junctions, während gleichzeitig stattfindender globaler Hydrolyse des Lipids durch die PLCβ, gezeigt werden. Pharmakologische Inhibierung der $PI(4,5)P_2$ Resynthese machte des Weiteren deutlich, dass diese lokale $PI(4,5)P_2$ Population für den Erhalt der ER-PM Junctions, sowie für die Reduktion des Abstands der beiden Membranen während der Aktivierung der PLCβ nötig ist. Zusammenfassend deuten meine Ergebnisse darauf hin, dass PI für die Produktion von $PI(4,5)P_2$ durch einen, an ER-PM Junctions assoziierten,

Multienzymkomplex geschleust wird, also eine Metabolit-Kanalisierung während der $PI(4,5)P_2$ Synthese stattfindet.

Neben TubbyCT reichert sich auch das Volllängenprotein Tubby, sowie sein naher Verwandter TULP3 an ER-PM Junctions an. Bisher beschränkte sich die Funktion der Tubby-ähnlichen Proteine (TULPs) auf die Rekrutierung G-Protein gekoppelter Rezeptoren in Primärzilien, meine Daten jedoch deuten auf eine weitere, konservierte Funktion der TULPs an ER-PM Junctions hin.

1 Introduction

1.1 Cellular Membranes

Cellular membranes are fluid lipid bilayers embedding integral and peripheral membrane proteins. The lipid bilayer constitutes a selectively permeable barrier segregating an interior from an exterior aqueous milieu. Integral channels and transporters confer selective permeabilities for individual ions and biological molecules. During evolution of early life, the development of a membranous lipid structure enclosing the cellular components was a key step to achieve a free-living organism. In eukaryotes endomembranes additionally compartmentalize cells, thereby generating highly specialized organelles enclosing environments which favor certain biochemical processes. However, apart from serving as a barrier, membranes constitute important signaling compartments which pass information from one side to the other. The assembly of protein complexes at and within membranes improves signaling efficiencies and membrane lipids directly participate in signal transduction as they serve as first and second messengers (reviewed in Casares, Escribá and Rosselló, 2019).

Cellular membranes are highly specialized compartments with lipid and protein compositions adjusted to their respective functions. Endomembranes of different organelles as well as the plasma membrane (PM) show unique lipid and protein mixtures which vary additionally between species and cell types. Furthermore, membranes are often asymmetric showing different compositions at the inner and outer leaflets. And finally, lipids of one leaflet are not homogeneously distributed. The best studied example of inter-leaflet lipid inhomogeneity are so-called 'lipid rafts', structures which derive from the self-assemble of sterols and sphingolipids and which further recruit phospholipids with saturated acyl chains as well as specific proteins. 'Lipid rafts' are small in size (10-200 nm), highly dynamic and constitute important cell signaling and membrane trafficking platforms (reviewed in Pike, 2006; reviewed in Lingwood and Simons, 2010; reviewed in Simons and Sampaio, 2011; reviewed in Owen *et al*., 2012). Sterol-sphingolipid self-assembly is an example of how lipids shape the sub-compartmentalization of membranes, however also proteins can generate their own lipid microenvironment and thereby considerably change membrane composition (reviewed in Epand, 2008; Corradi *et al.*, 2018).

The PM of a typical animal cell comprises approximately 50% lipids and 50% proteins by weight, this corresponds to approximately 1 protein molecule every 50-100 lipids (reviewed in Cooper, 2000). The main structural lipids of the outer leaflet of the PM are phosphatidylcholine, sphingomyelin and glycolipids, whereas the inner leaflet is enriched in phosphatidylethanolamine and phosphatidylserine (PS). Moreover, the quantitatively minor, but functionally very important structural and signaling lipid family of phosphoinositides and their precursor phosphatidylinositol (PI) are exclusively present at the inner leaflet of the PM. The negatively charged headgroups of PS, PI and phosphoinositides confer the characteristic negative surface charge to the cytosolic leaflet. Besides the above-mentioned structural lipids, cholesterol, a small sterol which inserts into the bilayer is a major component of the PM. It accounts for up to 35% of the PM lipids and plays an important role in the 'lipid raft' formation and thus in the lateral sub-compartmentalization of the PM (reviewed in Cooper, 2000; reviewed in Casares, Escribá and Rosselló, 2019).

1.2 Phosphoinositides

Phosphoinositides are a family of structural phospholipids with regulatory functions in signal transduction, membrane trafficking and cellular metabolism. They derive from phosphatidylinositol (PI), a glycerophospholipid whose phosphate moiety is esterified with *myo*-inositol. The inositol ring structure can be reversibly phosphorylated at its 3, 4 and 5 positions, thereby generating seven distinct phosphoinositide species. Numerous kinases and phosphatases are implicated in phosphoinositide interconversion (Figure 1.1). Their differential abundance and activity at distinct cellular membranes generate membrane-specific phosphoinositide compositions which contribute substantially to membrane identities. Phosphoinositides are involved in many cellular processes as they recruit cytosolic proteins to membranes and modulate the activity of various membrane proteins (reviewed in Di Paolo and De Camilli, 2006; reviewed in Balla, 2013; reviewed in Schink, Tan and Stenmark, 2016).

At the PM phosphoinositides constitute approximately 4% of all glycerophospholipids (Traynor-Kaplan *et al.*, 2017). Phosphatidylinositol-(4,5)-bisphosphate ($PI(4,5)P_2$) is the most prevalent phosphoinositide at the PM and only scarcely present at endomembranes. It is mainly generated from PI via sequential phosphorylation by PI4 kinases (PI4K) and PI4P5 kinases (PIP5K) (reviewed in Balla, 2013; reviewed in

Pemberton, Kim and Balla, 2020). Phosphatdylinositol-4-phosphate (PI4P) is only marginally less prevalent than $PI(4,5)P_2$, in contrast to their common precursor PI whose abundance is very low at the PM (Pemberton *et al.*, 2020; reviewed in Pemberton, Kim and Balla, 2020; Zewe *et al.*, 2020). In addition to $PI(4,5)P_2$, $PI(3,4,5)P_3$ constitutes a signature phosphoinositide of the PM. Its abundance is very low under resting conditions, but growth factor stimulation activates type I PI3-kinases (PI3Ks) which generate $PI(3,4,5)P_3$ from $PI(4,5)P_2$. $PI(3,4,5)P_3$ promotes cell growth and cell proliferation and in turn can be step-wise dephosphorylated by SHIP and INPP4B to form $PI(3,4)P_2$ and PI3P, two further scarcely present phosphoinositides at the PM (reviewed in Schink, Tan and Stenmark, 2016).

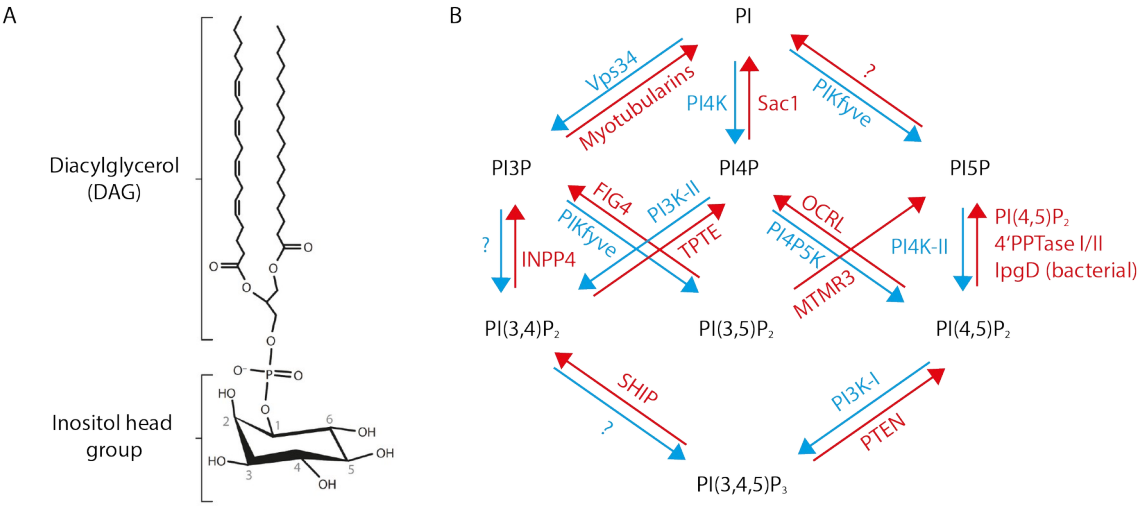

Figure 1.1: Phosphoinositide structure and interconversion
(**A**) Phosphatidylinositol (PI) structure. PI is composed of a membrane-anchored diacylglycerol (DAG) backbone esterified with an inositol head group. Phosphorylations of its 3, 4 and 5 positions generate the seven distinct phosphoinositides. (**B**) Kinases (blue) and phosphatases (red) involved in phosphoinositide interconversion. Modified from Schink, Tan and Stenmark, 2016.

1.2.1 Phosphatidylinositol-4-phosphate

In mammalian cells PM PI4P pool is mainly generated by PI4KIIIα (Balla *et al.*, 2005, Balla *et al.*, 2008; Nakatsu *et al.*, 2012; Bojjireddy *et al.*, 2014) which is embedded in a complex with TTC7 (tetratricopeptide repeat protein 7), FAM126A (hyccin) and EFR3 (Nakatsu *et al.*, 2012; Baskin *et al.*, 2016). The palmitoylated and thus membrane-anchored EFR3 determines PM localization and catalytic activity of the complex (Nakatsu *et al.*, 2012; reviewed in Pemberton, Kim and Balla, 2020). An alternative complex comprising PI4KIIIα, EFR3 and TMEM150 has also been described and might confer plasticity to PI4P production at the PM (Chung *et al.*, 2015b).

For a long time PM PI4P was considered as a $PI(4,5)P_2$ precursor, only. However, independent PI4P effectors have been characterized and the role of PI4P for non-vesicular lipid transport cycles and thus membrane lipid homeostasis has become evident (reviewed in D'Angelo *et al*., 2008; Hammond, Schiavo and Irvine, 2009; reviewed in Balla, 2013; Chung *et al*., 2015a; reviewed in Choy, Han and Botelho, 2017; reviewed in Pemberton, Kim and Balla, 2020). Nevertheless, PI4P serves as substrate for PIP5Ks which phosphorylate its 5' position to generate $PI(4,5)P_2$. Human cells express three PIP5K isoforms (PIP5Kα, β and γ) and all of them have been associated with PM $PI(4,5)P_2$ production (Ishihara *et al*., 1996; Loijens and Anderson, 1996; Ishihara *et al*., 1998; reviewed in van den Bout and Divecha, 2009; reviewed in Pemberton, Kim and Balla, 2020). However, it has remained puzzling that the bulk pool of PI4P of the PM appears to be distinct from the pool that constitutes the $PI(4,5)P_2$ precursor, as depletion of PI4P had remarkably little effect on the $PI(4,5)P_2$ concentration under most conditions (Hammond *et al.*, 2012).

1.2.2 Phosphatidylinositol-4,5-bisphosphate

$PI(4,5)P_2$ is a signature lipid of the PM and implicated in a huge variety of cellular processes ranging from exo- and endocytosis to cell motility and attachment of the cytoskeleton. $PI(4,5)P_2$ is also an important co-factor of many ion channels and transporters. Moreover, it serves as precursor of the second messengers phosphatidylinositol-(3,4,5)-trisphosphate ($PI(3,4,5)P_3$) as well as diacylglycerol (DAG) and inositol-(1,4,5)-trisphosphate ($I(1,4,5)P_3$) (reviewed in Di Paolo and De Camilli, 2006; reviewed in Schink, Tan and Stenmark, 2016; reviewed in Dickson and Hille, 2019). It has been postulated that $PI(4,5)P_2$, in order to guarantee its multifunctionality, laterally segregates into functionally distinct and spatially separated $PI(4,5)P_2$ pools (Hope and Pike, 1996; reviewed in Martin, 2001; Johnson and Rodgers, 2008; reviewed in Kwiatkowska, 2010; van den Bogaart *et al.*, 2012; Wang and Richards, 2012). According to this hypothesis, individual $PI(4,5)P_2$ pools assemble with different proteins and signaling complexes and thereby achieve discrete functions. Importantly, differential accessibility of $PI(4,5)P_2$ producing and consuming enzymes allows independent regulation of such pools.

PM $PI(4,5)P_2$ levels can be rapidly decreased by activation of Gq-coupled receptors (GqPCRs). GTP-loaded Gα subunits but also Gβγ stimulate phospholipase C-β (PLCβ)

which hydrolyses $PI(4,5)P_2$ into DAG and $I(1,4,5)P_3$. DAG, an activator of the PKC, stays membrane-bound, whereas the cytosolic $I(1,4,5)P_3$ translocates to $I(1,4,5)P_3$ receptors at the endoplasmic reticulum (ER) membrane where it triggers Ca^{2+} release from the ER into the cytosol (reviewed in Kadamur and Ross, 2013). PLCβ activation regulates cellular functions ranging from cell growth, differentiation and migration to neuronal circuit control (reviewed in Suh *et al.*, 2008; reviewed in Yang *et al.*, 2013). However, to maintain basic PM functions and also to enable response to ongoing receptor activation $PI(4,5)P_2$ is rapidly resynthesized following GqPCR stimulation.

1.2.3 The PI cycle

As mentioned above, PM $PI(4,5)P_2$ is predominantly generated via sequential phosphorylation from PI. PI, however, is not synthesized at the PM, but at the ER membrane by two enzymatic steps: CDP-DAG synthase (CDS) catalyzes the generation of CDP-DAG from CTP and phosphatidic acid (PA) and subsequently PI synthase (PIS) generates PI from *myo*-inositol and CDP-DAG. Importantly, PLC-derived products DAG and $I(1,4,5)P_3$ that arise in the PM are recycled for PI synthesis: DAG is phosphorylated at the PM to form PA and reused for CDP-DAG synthesis. $I(1,4,5)P_3$ in turn is recycled to *myo*-inositol, but the latter can also be synthesized *de novo* or taken up from the cell's surroundings (reviewed in Balla, 2013; reviewed in Pemberton, Kim and Balla, 2020). In order to recycle PA to PI, it needs to be transported from the PM to the ER. Moreover, to restore PM $PI(4,5)P_2$ content, PI must be transferred in the opposite direction. In this way, a metabolic cycle (PI cycle) emerges that comprises PI generation in the ER and PI consumption at the PM (Figure 1.2). The lipid transfer within this cycle is mainly achieved by PI transfer proteins (PITPs) of the Nir family (Chang *et al.*, 2013; Kim *et al.*, 2013; Chang and Liou, 2015; Kim *et al.*, 2015). Besides Nir proteins, TMEM24 contributes to PI transfer mainly in neuroendocrine cells (Lees *et al.*, 2017; Sun *et al.*, 2019) and also the soluble, single-domain class I PITPs have been implicated in transfer of PI between membranes (reviewed in Pemberton, Kim and Balla, 2020).

Landmark studies from the last years found that PI transfer predominantly occurs at membrane contact sites (MCSs) between the ER and the PM which are specifically formed and tightened upon PLC activation (Chang *et al.*, 2013; Idevall-Hagren *et al.*, 2015).

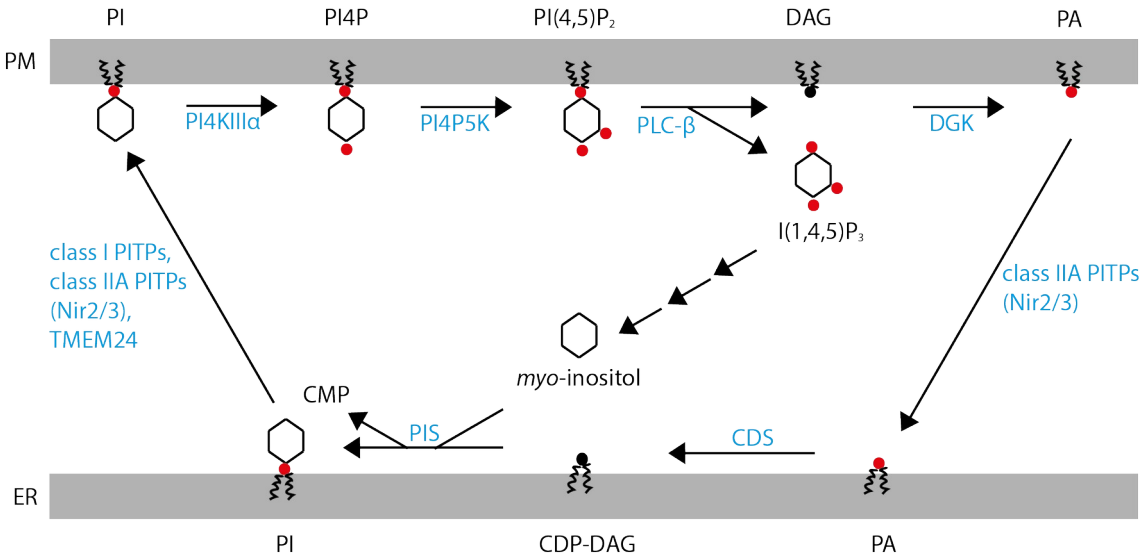

Figure 1.2: The PI cycle
Activation of PLCβ results in $PI(4,5)P_2$ hydrolysis and DAG and $I(1,4,5)P_3$ production. Both products are reused for PI synthesis at the ER membrane. In order to replenish PM $PI(4,5)P_2$ pool, PI is transferred from the ER to the PM by PI transfer proteins (PITPs). At the PM PI is sequentially phosphorylated mainly by PI4KIIIα and PIP5Ks. Modified from Pemberton, Kim and Balla, 2020.

1.3 Membrane contact sites

Membrane contact sites (MCSs) are close membrane appositions formed between different organelles among each other as well as with the PM. They allow inter-organelle communication and lipid and ion exchange without membrane fusion. Tethering proteins tightly link the two opposing membranes, thereby facilitating distances of approximately 3-30nm (reviewed in Phillips and Voeltz, 2016). This enables lipid transfer proteins to either bridge the cytosol directly or to shuttle between the two membranes (Chang *et al.*, 2013; Schauder *et al.*, 2014). Another pivotal function of MCSs is the generation of locally highly increased Ca^{2+} concentrations via Ca^{2+} fluxes across its membranes. This allows a high spacial resolution of cellular signaling events (Wang *et al.*, 2001; Wang *et al.*, 2004). Moreover, MCSs are the site of action of various trans-acting enzymes (Anderie, Schulz and Schmid, 2007; Dickson *et al.*, 2016; reviewed in Phillips and Voeltz, 2016).

MCSs constitute specific membrane compartments which are enriched in structural and functional proteins, but which are also devoid of certain components present in the rest of the respective organelle. Ribosomes for example are specifically excluded from MCSs formed by the ER (West *et al.*, 2011; reviewed in Okeke *et al.*, 2016; reviewed in Phillips and Voeltz, 2016). Also the lipid composition is likely to be specific at MCSs as

membrane binding of various MCS proteins is dependent on individual lipids (Giordano *et al.*, 2013; Kim *et al.*, 2013; Chung *et al.*, 2015a; Lees *et al.*, 2017; Besprozvannaya *et al.*, 2018). Moreover, lipid transfer activity of certain MCS-resident proteins may generate a local lipid microenvironment. MCSs can be formed and dissolved dynamically in response to cell signaling events as in case of MCSs between the ER and the PM (Zhang *et al.*, 2005; Chang *et al.*, 2013; Giordano *et al.*, 2013). However, they can also be very stable: MCSs formed by the ER and mitochondria even persist if mitochondria travel across the cell, thereby dragging the ER behind them (reviewed in Phillips and Voeltz, 2016).

In summary, it has become evident that MCSs play pivotal and general roles in a variety of cellular processes including lipid biosynthesis and transport, calcium signaling and homeostasis as well as organelle biogenesis and trafficking (reviewed in Phillips and Voeltz, 2016; reviewed in Wu, Carvalho and Voeltz, 2018).

1.4 ER-PM junctions

MCSs formed by the ER and the PM (ER-PM junctions) are crucial for lipid transfer and PM lipid homeostasis, as well as for Ca^{2+} regulation (reviewed in Okeke *et al.*, 2016; reviewed in Saheki and De Camilli, 2017; reviewed in Pemberton, Kim and Balla, 2020). Formation and dissolution of ER-PM junctions strongly depend on Ca^{2+} signaling: [I] Depletion of intracellular Ca^{2+} stores initiates the interaction of the ER-localized Ca^{2+} sensor STIM with the PM Ca^{2+} channel Orai, a key step during store-operated Ca^{2+} entry (SOCE). This ER-PM junction formation ensures fast coupling of intracellular Ca^{2+} store depletion with the Ca^{2+}-release activated Ca^{2+} (CRAC) current for refilling internal stores (Zhang *et al.*, 2005; Luik *et al.*, 2006; Orci *et al.*, 2009). [II] Cytoplasmic Ca^{2+} rise results in the formation and tightening of Extended Synaptotagmin (E-Syt)-mediated ER-PM junctions (Chang *et al.*, 2013; Giordano *et al.*, 2013). They are implicated in $PI(4,5)P_2$ homeostasis as the phosphatidylinositol transfer proteins (PITPs) Nir2 and Nir3 are recruited into these junction where they deliver the $PI(4,5)P_2$ precursor PI from the ER to the PM (Chang *et al.*, 2013; Kim *et al.*, 2013; Chang and Liou, 2015; Kim *et al.*, 2015).

It has been discussed controversially whether these functional differences are reflected in structurally and functionally distinct populations of ER-PM junctions. Although E-Syt- and STIM1-Orai1-rich ER-PM junctions can form independently of each other

(Giordano *et al.*, 2013; Idevall-Hagren *et al.*, 2015), their formation often occurs at the same PM regions (Chang *et al.*, 2013; Idevall-Hagren *et al.*, 2015). However, recent cryo-electron tomography data show clear ultrastructural differences between ER-PM junctions mediated by E-Syts and by STIM1-Orai1, respectively. In COS-7 cells, over-expression of E-Syts evokes junctions with an ER-PM distance of 21.8 ± 1.8 nm (E-Syt1) and 18.8 ± 0.4 nm (E-Syt3) with an electron-dense layer between the two membranes. Conversely, STIM1-Orai1-mediated junctions displayed larger clefts (27.1 ± 2.8 nm membrane distance) and the gap between ER and PM was spanned by filamentous structures. In untransfected neurons both types of ER-PM junctions, but also junctions with both, electron-dense layer and filamentous structures were observed, as well as junctions of unknown nature. This clearly argues for the existence of different types of ER-PM junctions (Fernández-Busnadiego, reviewed in Saheki and De Camilli, 2015).

Indeed, besides the two above-mentioned, best-characterized ER-PM contact sites other subtypes have been described involving tethers of the GRAM (Rab-like GTPase activators and myotubularins) domain-containing protein family (Besprozvannaya *et al.*, 2018), the ORP (OSBP-related protein) family (Chung *et al.*, 2015a) as well as SNARE proteins (Petkovic *et al.*, 2014) and TMEM24 (Lees *et al.*, 2017). Additionally, ER-resident VAMP-associated proteins (VAPs) recruit cytosolic or PM-bound proteins to ER-PM junctions, like for example Nir proteins and some ORP family members (Loewen, Roy and Levine, 2003; Amarilio *et al.*, 2005).

Although often clearly linked to a certain junction subtype, individual tethering proteins can have pleiotropic functions at diverse MCSs. GRAMD2A for example, a constitutive tether which pre-marks ER-PM junctions for STIM1 recruitment and thus for SOCE, also co-localizes with E-Syt2/3 (Besprozvannaya *et al.*, 2018). Redundant functions of some tethering proteins may also explain the lack of a major systemic phenotype of E-Syt triple knock-out mice (Sclip *et al.*, 2016). However, the close homolog of GRAMD2A, GRAMD1A clearly localizes to distinct ER-PM junctions, additionally indicating a highly specialized role of individual tethers (Besprozvannaya *et al.*, 2018).

1.4.1 The role of ER-PM junctions in lipid homeostasis

The ER is site of synthesis of the majority of lipids present at cellular membranes. Vesicular transport accounts for a large fraction of the lipid transport to organelles connected to the secretory and endocytic pathways and thus also for the ER-to-PM trafficking. However, as it is a rather slow process it cannot explain rapid recoveries following the break-down of certain lipids. Indeed, blocking of vesicular transport does not inhibit lipid delivery from the ER to the PM. Hence, non-vesicular transport complements vesicular trafficking especially to ensure cellular characteristics like the fast adjustment of lipid homeostasis but also the heterogeneity of different cellular membranes. At ER-PM contact sites, the minimal membrane gap facilitates effective lipid transport by lipid transfer proteins (LTPs) and their contribution to PM lipid composition has been brought to light in recent years (reviewed in Saheki and De Camilli, 2017; reviewed in Pemberton, Kim and Balla, 2020).

The PM enrichment in PS for example is at least in parts established by the ER-PM tethering proteins ORP5 and ORP8 (Chung *et al.*, 2015a). They integrate into the ER membrane with their hydrophobic tail sequence and bind PM PI4P via their N-terminal pleckstrin homology (PH) domains. ORP5 and ORP8 are PS/PI4P counter-transporters, which use the PI4P gradient between the PM and the ER to deliver PS from the ER to the PM. Thereby they also directly impact on PI4P levels of the PM. This PS/PI4P countertransport depends on the subsequent PI4P consumption by the ER-resident 4-phosphatase Sac1, because PI4P-depleted ER-microenvironment is needed to maintain the PI4P gradient but it probably also favors PS binding at the ER-membrane interface (Figure 1.3A) (Chung *et al*., 2015a; reviewed in Pemberton, Kim and Balla, 2020).

Sterols are another lipid family enriched at the PM compared to their site of synthesis, the ER. The sterol gradient is proposed to be established by proteins of the LAM/GRAMD family. They consist of a C-terminal ER-anchoring sequence, a StAR-related lipid transfer (StART) domain and a potential PM-binding domain. StART domains bind and transfer cholesterol, sphingolipids and glycerophospholipids. In yeast it could be shown that the LAM/GRAMD family proteins Ysp2 and Lam4 specifically bind sterols and that Ysp2 knock-out cells show defects in PM sterol content (Gatta *et al.*, 2015; reviewed in Saheki and De Camilli, 2017). In humans 5 orthologs have been identified (GRAMD1a-c and GRAMD2a/b) with GRAMD2a/b lacking the StART-like

domain. It has been shown that GRAMD1a localizes to ER-PM junctions (Besprozvannaya *et al.*, 2018), but its function there remains to be investigated (Figure 1.3B).

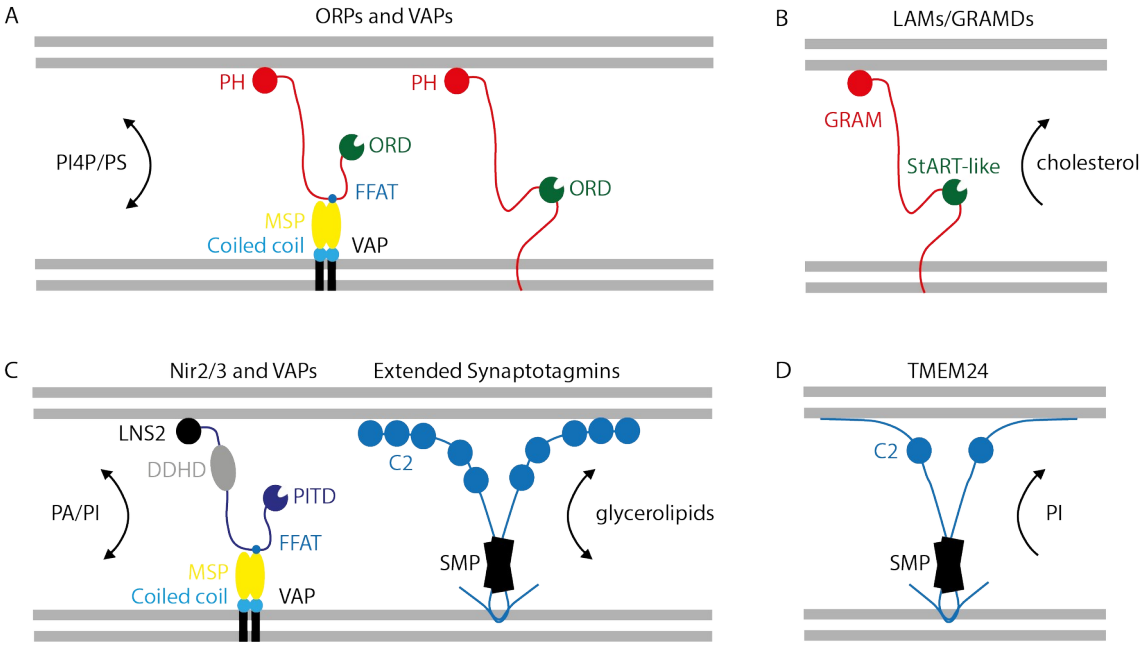

Figure 1.3: ER-PM contact sites involved in lipid homeostasis
(**A**) ORPs account considerably for the PS enrichment at the PM. They use the PI4P gradient between PM and ER to transport PS from the ER to the PM. ORPs are either directly ER-anchored or bind the ER via VAPs. (**B**) Proteins of the LAM/GRAMD family contain a StAR-related lipid transfer (StART) domain domain and are putative cholesterol transporting proteins. (**C**) ER-PM junctions formed by Extended Synaptotagmins (E-Syts) recruit VAP-anchored Nir proteins and contribute considerably to the recycling of the PLC-derived metabolites DAG and PA and to phosphoinositide resynthesis. E-Syts can directly transport glycerolipids via their SMP domains, Nir proteins are phosphatidylinositol (PI)/PA exchanger and thereby refill PM PI pool. (**D**) TMEM24 additionally contributes to PI transfer from the ER to the PM mainly in neuroendocrine cells. Modified from Saheki and De Camilli, 2017.

Another family of LTPs are defined by the presence of a so-called tubular lipid-binding (TULIP) domain. TULIP domains have been described to harbor and transport lipids. Specifically, the ER-PM tethering proteins E-Syt1-3 and the transmembrane protein 24 (TMEM24) contain synaptotagmin-like mitochondrial lipid-binding protein (SMP) domains that belong to the TULIP superfamily (Giordano *et al.*, 2013; Lees *et al.*, 2017). E-Syts and TMEM24 are ER-anchored and bind the PM in trans: E-Syts via specific binding of $PI(4,5)P_2$ (Giordano *et al.*, 2013) and TMEM24 through binding to acidic lipids like PS or phosphoinositides (Lees *et al.*, 2017). TMEM24, through its SMP domain, has been shown to specifically transfer PI from the ER to the PM and to thereby contribute to $PI(4,5)P_2$ recovery following PLC-induced $PI(4,5)P_2$ depletion

(Lees *et al*., 2017; Sun *et al.*, 2019). In contrast, the SMP domains of E-Syts harbor phospholipids without preference for a specific lipid (Schauder *et al.*, 2014). However, it has been shown that E-Syts are involved in DAG clearance following PLCβ activation, most likely via their direct lipid transport capability (Figure 1.3C, D) (Saheki *et al.*, 2016).

E-Syts additionally contribute to phosphoinositide homeostasis following Gq-coupled receptor activation as they shape the ER-PM junctions involved in Nir-mediated PI transfer from the ER to the PM (Chang *et al*., 2013). The function, regulation, and the molecular components of these particular ER-PM contact sites are described in detail in the next section.

1.4.2 Extended Synaptotagmin-mediated and Nir-containing ER-PM junctions

$PI(4,5)P_2$ is a signature lipid of the PM whose precursor PI is synthesized at the ER. Following $PI(4,5)P_2$ break-down by activation of Gq-coupled receptors, $PI(4,5)P_2$ is rapidly resynthesized (reviewed in Pemberton, Kim and Balla, 2020) via the PI cycle (see also section 1.2.3), thereby enabling cells to respond to ongoing receptor activation (Chang *et al*., 2013). The pivotal PI transfer from the ER to the PM mainly takes place at E-Syt-mediated and Nir-containing ER-PM junctions (Kim *et al*., 2015).

PLCβ activation elevates cytosolic Ca^{2+} levels which are sensed by E-Syt1 (see section 1.4.2.1 below). The ensuing PM binding results in the tightening of preformed E-Syt-containing ER-PM contact sites, but also in formation of new junctions (Chang *et al*., 2013). Simultaneously, PA is generated at the PM by DAG kinases (reviewed in Carrasco and Mérida, 2007). PA and DAG accumulation at the PM together with the increased ER-PM connectivity recruit Nir proteins into the ER-PM junctions. Nir proteins are PI/PA exchanger which deliver PI from its site of synthesis, the ER to the PM (see section 1.4.2.2 below). Vice versa, PA is transported from the PM to the ER, where it is subsequently recycled to form new PI (Figure 1.4) (Chang *et al*., 2013; Kim *et al*., 2013; Chang and Liou, 2015; Kim *et al*., 2015).

Thus, E-Syts and Nir proteins have a synergistic role in disposing of the PLCβ-derived metabolites, but Nir proteins additionally provide PI, the $PI(4,5)P_2$ precursor, to the PM. Together, they ensure effective $PI(4,5)P_2$ resynthesis after PLCβ activation and consequently are key players in $PI(4,5)P_2$ homeostasis.

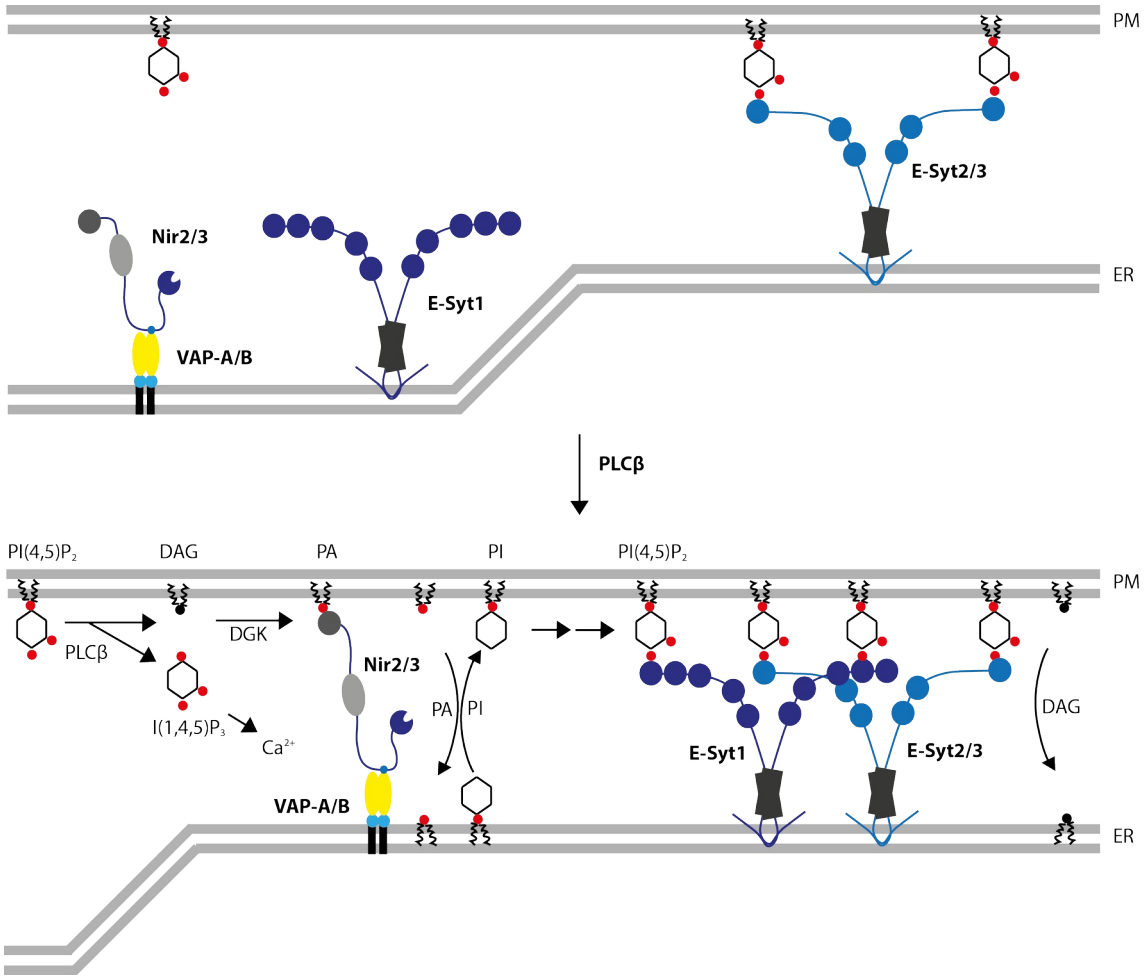

Figure 1.4: Activation of PLCβ activates Nir-mediated PI transfer at ER-PM contact sites
ER-PM junctions involved in PI transfer are preformed under resting conditions due to Ca^{2+}-independent PM binding of E-Syt2/3 (upper scheme). Activation of PLCβ results in rise in intracellular Ca^{2+} and accumulation of DAG and PA at the PM (lower scheme). E-Syt1 is recruited Ca^{2+}-dependently to PM, thereby increasing number and connectivity of ER-PM contact sites. This initiates DAG- and PA-dependent recruitment of the PI transfer proteins Nir2/3. PLC-derived metabolites are transported to the ER by E-Syts (DAG) and Nirs (PA). Nir additionally transports PI from the ER to the PM. Modified from Chang *et al*., 2013 and Chang and Liou, 2015.

1.4.2.1 Extended Synaptotagmins

Extended Synaptotagmins (E-Syts) are a conserved eukaryotic ER-binding protein family of three members (E-Syt1-3), which can bind the PM in trans (Morris *et al.*, 1999; Min, Chang and Südhof, 2007; Giordano *et al*., 2013). ER association occurs via an N-terminal, 30 amino acid long hydrophobic region which inserts into the ER membrane as a hairpin (Giordano *et al*., 2013). Furthermore, E-Syts consist of a cytoplasmic SMP domain as well as multiple C2 domains (three in E-Syt2 and E-Syt3 and five in E-Syt1). C2A and C2B are arranged in tandem and are most likely evolutionarily duplicated in E-Syt1 (Figure 1.5) (Min, Chang and Südhof, 2007).

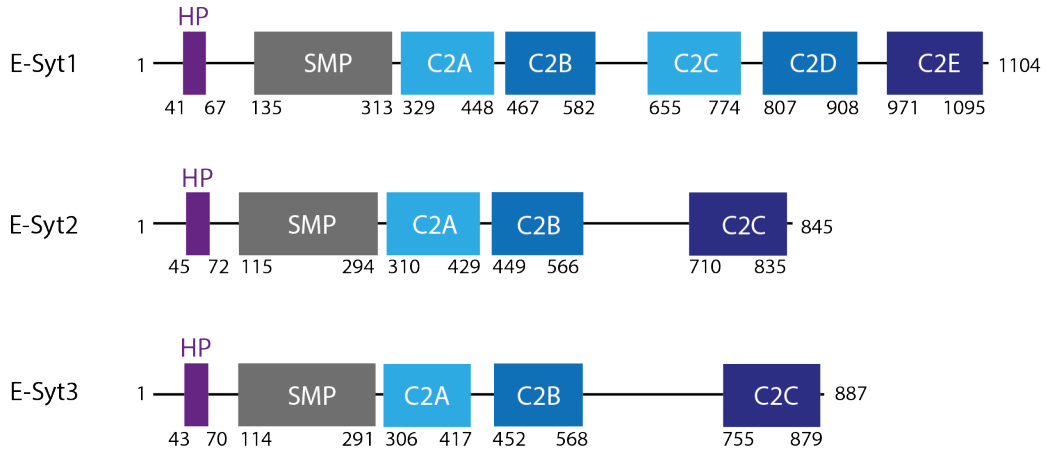

Figure 1.5: Structure of E-Syt1-3
E-Syts consist of an ER-binding hairpin (HP), a cytoplasmic SMP domain and three to five C2 domains. In E-Syt1 C2C and C2D are evolutionarily duplicated from C2A and C2B. Numbers indicate amino acid position in the human E-Syts. Modified from Herdman and Moss, 2016.

PM targeting is mediated by specific $PI(4,5)P_2$ binding of the terminal C2 domain (C2C in E-Syt2/3 and C2E in E-Syt1) and – in case of E-Syt1 – by additional $PI(4,5)P_2$ binding of the central C2C domain. In E-Syt2 and E-Syt3, $PI(4,5)P_2$ binding is Ca^{2+}-independent, leading to ER-PM tethering under resting conditions (Chang *et al.*, 2013; Giordano *et al.*, 2013; Idevall-Hagren *et al.*, 2015). In contrast, E-Syt1 $PI(4,5)P_2$ binding is impaired in absence of Ca^{2+}, resulting in exclusive and ubiquitous localization to the ER but lack of PM association. However, Ca^{2+} binding to the E-Syt1 C2C domain facilitates the direct $PI(4,5)P_2$ binding of C2C. Moreover, under resting conditions the C2C domain auto-inhibits $PI(4,5)P_2$ binding of the C2E domain which is abrogated in presence of Ca^{2+} (Chang *et al.*, 2013; Giordano *et al.*, 2013; Bian, Saheki and De Camilli, 2018). In summary, intracellular Ca^{2+} rise stimulates E-Syt1 $PI(4,5)P_2$ affinity and leads to tight PM binding and enhanced ER-PM connectivity with a reduced gap distance of ~10 nm.

The SMP domain belongs to the TULIP superfamily of protein domains which is described to harbor and transport lipids. Indeed, the crystal structure of dimerized E-Syt2 SMP domains revealed a 90 Å-long cylinder harboring a hydrophobic channel. Using mass spectrometry, glycerophospholipids were detected inside this hydrophobic groove (Schauder *et al.*, 2014). On a liposome-based assay, E-Syt1 SMP domain showed Ca^{2+}-dependent glycerophospholipid transport activity along a concentration gradient and in E-Syt1/2 double- and E-Syt1/2/3 triple-knock-out cells DAG clearance

from the PM after PLCβ activation was delayed (Saheki *et al*., 2016). However, basal glycerophospholipid composition of the PM was not altered in these knock-out cells (Saheki *et al*., 2016). Ca^{2+}-dependency of E-Syt1 lipid transport activity can be explained by an auto-inhibitory interaction of the SMP domain with the C2A domain which is removed upon Ca^{2+} binding to C2A (Bian, Saheki and De Camilli, 2018). The C2A domains of E-Syt2 and E-Syt3 also hold Ca^{2+} binding sites. As membrane-binding of E-Syt2 and E-Syt3 is Ca^{2+}-independent it has been suggested that Ca^{2+} binding regulates lipid transport activity also in these proteins.

Due to their simultaneous ER and PM binding capacity, E-Syts represent prototypical ER-PM tether proteins. The Ca^{2+}-dependency of E-Syt1 additionally allows dynamic formation of ER-PM junctions. E-Syt1 PM tethering occurs at micromolar Ca^{2+} concentrations (EC50 = 1.7 ± 0.4 μM), which are reached during SOCE, depolarisation of excitable cells, and PLCβ activation (Idevall-Hagren *et al*., 2015). E-Syts homo- and heterodimerize and heterodimers show intermediate properties of both proteins: Co-expression of E-Syt1 with E-Syt2 (or E-Syt3) shifts E-Syt1 to the PM under resting conditions and vice versa it confers a Ca^{2+}-dependency to E-Syt2 similar to that of E-Syt1 (EC50 = 1.4 ± 0.2 μM) (Schauder *et al*., 2014; Giordano *et al*., 2015; Idevall-Hagren *et al*., 2015; Tremblay *et al.*, 2015). Because PM localization of E-Syts depends on $PI(4,5)P_2$, Ca^{2+} levels above 10-50 μM result in loss of E-Syt1 and E-Syt2 from the PM, most likely due to Ca^{2+}-activated PLCβ activity (Idevall-Hagren *et al*., 2015).

1.4.2.2 Nir proteins

The Nir (PYK2 N-terminal domain-interacting receptor) family of proteins consists of three members in mammals (Nir1-3) (Figure 1.6) (Lev *et al.*, 1999). Nir2, also named PITPnm1 (phosphatidylinositol transfer protein membrane-associated 1) was identified as a mammalian homolog of the *Drosophila* retinal degradation B gene (rdgB) (Aikawa, Hara and Watanabe, 1997). In rdgB null-mutant flies retinal degradation occurs presumably because $PI(4,5)P_2$ levels cannot be restored after light-induced PLC activation (Trivedi and Padinjat, 2007). Recent studies showed that also in mammals Nir2 and Nir3 are key players in maintaining PM $PI(4,5)P_2$ and also $PI(3,4,5)P_3$ levels following receptor stimulated $PI(4,5)P_2$ depletion (Kim *et al*., 2013; Chang and Liou, 2015). Nir2 and Nir3 (but not Nir1) comprise an N-terminal PI transfer domain (PITD) which provides the PM with ER-derived PI. The PITD seems to function as a

monomeric shuttle which extracts PI from the ER membrane and transports it to the PM where it is released. At the PM the PITD is loaded with PA (accumulating as a result of PLC activity), which is in turn delivered to the ER where it is subsequently recycled to PI (Kim *et al.*, 2015; reviewed in Pemberton, Kim and Balla, 2020).

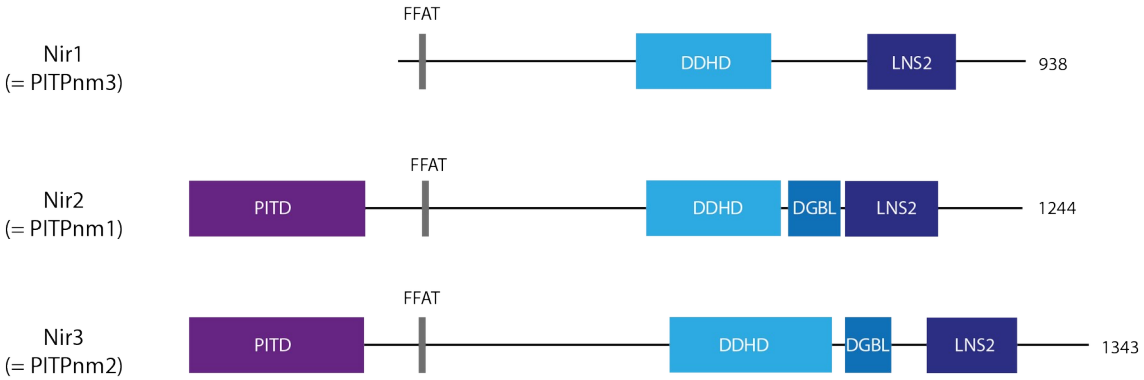

Figure 1.6: Structure of Nir proteins 1-3
Nir1-3 (also called PITPnm3, PITPnm1, PITPnm2) belong to the family of classIIA PITPs. However, only Nir2 and Nir3 consist of a PITD and are functional transfer proteins. Furthermore, Nir1-3 consist of an FFAT motif, a DDHD and LNS2 domain. The FFAT motif mediates the interaction with the ER-resident VAP proteins and PM PA is bound by their DDHD and LNS2 domains. Nir2 and Nir3 additionally hold a DAG-binding DGBL domain. Numbers indicate amino acid lengths in the human proteins. Modified from Amarilio *et al.*, 2005 and Kim *et al.*, 2015.

In resting cells Nir proteins localize to the golgi (Kim *et al.*, 2013), the ER (Aikawa *et al.*, 1999; Kim *et al.*, 2015) and the cytosol (Kim *et al.*, 2015). They translocate to E-Syt-mediated ER-PM junctions following PLCβ activation. Targeting of Nir proteins to the ER is mediated by binding of the FFAT motif to the ER-resident VAP-A and VAP-B proteins (Amarilio *et al.*, 2005, Chang *et al.*, 2013). PM association is achieved by direct binding of the LNS2 and DDHD domains to PA (Kim *et al.*, 2013; Chang and Liou, 2015; Kim *et al.*, 2015; reviewed in Pemberton, Kim and Balla, 2020) and of the DDHD domain to DAG (Kim *et al.*, 2015). Hence, the translocation of Nir2/3 into ER-PM junctions is triggered by the accumulation of DAG and PA at the PM, but also by the decreased ER-PM junction gap distance due to E-Syt1 recruitment (Chang *et al.*, 2013).

In general, Nir2 and Nir3 both mediate a similar $PI(4,5)P_2$ replenishment function. Yet, Nir3 can sense more subtle $PI(4,5)P_2$ depletion because of a higher PA-binding capability compared to Nir2: e.g., Nir3 undergoes robust PM translocation following 10 µM histamine stimulation of Hela cells, whereas Nir2 translocation required 100 µM

histamine treatment. Similarly, addition of 100 µM PA was sensed by Nir3 but not by Nir2 (Chang and Liou, 2015). Moreover, Nir2 showed a higher PI transfer activity in comparison to Nir3. Analyzing $PI(4,5)P_2$ sensor dynamics and Ca^{2+} spiking, Chang and Liou (2015) could show that Nir3 is involved in maintaining basal $PI(4,5)P_2$ levels and important for $PI(4,5)P_2$ homeostasis following low level PLCβ activation. In contrast Nir2 predominantly contributes to $PI(4,5)P_2$ homeostasis during vigorous PLCβ activation.

1.4.2.3 VAMP-associated proteins

Besides E-Syts and Nir proteins VAMP-associated protein A and B (VAP-A/-B) are enriched at ER-PM junctions implicated in $PI(4,5)P_2$ resynthesis (Chang *et al*., 2013, Kim *et al*., 2015).

VAPs are a conserved eukaryotic protein family with two members in mammals (VAP-A and -B). They consist of an N-terminal major sperm protein (MSP) domain, a coiled-coil domain and a transmembrane domain. VAPs are integral ER membrane proteins with their MSP and coiled-coil domain reaching into the cytoplasm. They interact with many different proteins like SNAREs, viral proteins and FFAT motif-containing proteins (reviewed in Lev *et al.*, 2008). FFAT motifs (two phenylalanines in an acidic tract) are recognized by a conserved 16 aa-long region of the VAP MSP domain (Loewen, Roy and Levine, 2003; Kaiser *et al.*, 2005). Consistent with their interaction partners, VAPs are involved in functions like membrane trafficking, lipid transport and microtubule organization (reviewed in Lev *et al*., 2008). At ER-PM junctions VAP-A and VAP-B interact with the FFAT motif of Nir2 and Nir3. This interaction is essential for PLCβ induced recruitment of Nir proteins into ER-PM contact sites and vice versa, also triggers the accumulation of VAP-A/B at these contact sites following PLCβ stimulation (Amarilio *et al*., 2005; Chang *et al*., 2013; Kim *et al*., 2015).

1.5 Phosphoinositide binding domains

Phosphoinositide distribution and dynamics in living cells are typically studied by use of fluorescent genetically-encoded phosphoinositide probes. The lipid binding moiety of these biosensors constitute phosphoinositide binding protein domains such as for example Pleckstrin Homology (PH), FERM, FYVE or epsin N-terminal homology (ENTH) domains, which is routinely fused to GFP or any of its spectrally distinct analogs (reviewed in Hammond and Balla, 2015).

Biosensors should show high specificities towards a certain phosphoinositide species so that their localization is driven by distribution and dynamics of an individual phosphoinositide species only. Affinities should fit the biological range in such a way that lipid changes impact sensor localization. However, many commonly used biosensors bind more than one phosphoinositide species and additional binding to proteins often influences their behavior. Notably, such coincidence binding can also drive localization of the sensor to certain membrane compartments, thereby facilitating the study of specific lipid pools (Levine and Munro, 2002; reviewed in Hammond and Balla, 2015; He *et al.*, 2017).

Commonly used PI(4,5)P_2 sensors are the PH domain of PLCδ1 (PLCδ1-PH; (Stauffer, Ahn and Meyer, 1998; Várnai and Balla, 1998), the C-terminal domain of tubby (tubbyCT; Santagata *et al.*, 2001; Quinn, Behe and Tinker, 2008) as well as the recently described Epsin1 ENTH domain (Leitner *et al*., 2019). Each of these sensors decorates the PM under resting conditions and translocates into the cytoplasm upon PI(4,5)P_2 depletion via the activation of voltage-sensitive phosphatases (VSPs) (Halaszovich, Schreiber and Oliver, 2009; Leitner *et al*., 2019). However, each of the sensors also holds its individual advantages and disadvantages. The two most commonly used PI(4,5)P_2 sensors PLCδ1-PH and tubbyCT are introduced and compared below.

1.5.1 The PI(4,5)P_2 sensor PLCδ1-PH

Fluorescently tagged PLCδ1-PH (aa 1-175 of PLCδ1) is the most widely used PI(4,5)P_2 sensor (Stauffer, Ahn and Meyer, 1998; Várnai and Balla, 1998). PH domains are found in many signaling proteins and often direct them to the PM (or other membranes) due to their phosphoinositide and sometimes also protein binding capability. Phosphoinositides can be bound solely electrostatically and thus rather with low specificity (like in case of

PH domains from pleckstrin or spectrin) or in a high-affinity and stereo-specific manner (like for PLCδ1-PH). PH domains are ~120 aa in size and share a common structure of a β-sandwich which is enclosed at one side by an α-helix. They are electrostatically polarized with phosphoinositide binding occurring at the positively charged face (reviewed in Lemmon, 2003; reviewed in Lemmon, 2007).

The PH domain of PLCδ1 binds $PI(4,5)P_2$ but also $I(1,4,5)P_3$ with high specificity and affinity (Cifuentes, Honkanen and Rebecchi, 1993; Cifuentes, Delaney and Rebecchi, 1994; Yagisawa *et al.*, 1994; Garcia *et al.*, 1995; Lemmon *et al.*, 1995). Its crystal structure conforms to the general PH domain organization but it reveals two additional α-helices, one at the N-terminus and one in the β5/β6 loop. $I(1,4,5)P_3$ co-crystallization revealed its binding to the β1/β2 as well as to the β3/β4 loop (Ferguson *et al.*, 1995). $I(1,4,5)P_3$ binding competes $PI(4,5)P_2$ binding suggesting that they occupy the same binding pocket (Yagisawa *et al*., 1994). In the native protein this competition represents product inhibition and thus negatively regulates catalytic activity (Cifuentes, Delaney and Rebecchi, 1994).

PLCδ1-PH was first used as a sensor in 1998 by Stauffer and colleagues and by Várnai and Balla who showed its translocation into the cytoplasm upon PLC activation. Since then fluorescently-tagged PLCδ1-PH has been used in countless studies to examine PM $PI(4,5)P_2$ levels and localization. However, its high $I(1,4,5)P_3$ affinity (K_D = 0.21 ± 0.12μM) which even exceeds $PI(4,5)P_2$ binding affinity (K_D = 1.66 ± 0.80μM) has to be kept in mind when the sensor is used in experiments involving activation of PLC. In fact, it has been argued that this sensor reports $I(1,4,5)P_3$ production rather than $PI(4,5)P_2$ depletion in the context of Gq/PLC signaling (Garcia *et al*., 1995, Lemmon *et al*., 1995; Hirose *et al.*, 1999).

1.5.2 The $PI(4,5)P_2$ sensor tubbyCT

TubbyCT is the C-terminal tubby domain (aa 243-505) of the tubby protein. Tubby is the founder member of the tubby-like proteins (TULPs) comprising five members in mammals (tubby, TULP1-4) with TULP4 being very distantly related. TULPs consist of an unstructured N-terminal domain which comprises a nuclear-localization signal and the C-terminal tubby domain (tubbyCT) (reviewed in Mukhopadhyay and Jackson, 2011). TubbyCT drives PM localization of tubby by virtue of its binding to $PI(4,5)P_2$ (Santagata *et al*., 2001). Initially, it was suggested that PLC-induced $PI(4,5)P_2$ break-

down releases tubby from the PM to allow translocation into the nucleus where it acts as transcriptional regulator (Santagata *et al*., 2001). However, tubby-regulated genes have never been identified. This raised doubts on the function of tubby as a transcription factor. Recent investigations rather suggest a role of TULPs in primary cilia: $PI(4,5)P_2$-dependent binding of tubbyCT to G protein-coupled receptors (GPCRs) and binding of the tubby N-terminus to the intraflagellar transport complex A (IFT-A) delivers GPCRs to primary cilia. Subsequently, GPCR cargo is released into the cilium as the ciliary membrane domain is very low in $PI(4,5)P_2$ (Mukhopadhyay *et al.*, 2010; Sun *et al.*, 2012; Loktev and Jackson, 2013; Badgandi *et al.*, 2017). Ciliary defects are linked to obesity disorders (Chen *et al.*, 2002; Davenport *et al.*, 2007; Wang *et al.*, 2009; Loktev and Jackson, 2013) and thus might explain the maturity-onset obesity syndrome of *tubby* mice (Coleman and Eicher, 1990; Stubdal *et al.*, 2000).

Aside from its as yet poorly understood function, $PI(4,5)P_2$ binding of its C-terminal domain is undisputed. TubbyCT forms a helix-filled barrel structure, a $PI(4,5)P_2$ binding pocket is formed by the β-strands 4, 5 and 6 as well as the α-helix 6A. N310, K330, R332 and R363 coordinate the inositol ring and the 4- and 5-phosphates (Santagata *et al*., 2001). In lipid blot experiments tubbyCT showed high specificity towards phosphoinositides phosphorylated at adjacent ring positions, i.e. $PI(4,5)P_2$, $PI(3,4)P_2$ and $PI(3,4,5)P_3$. However, in living cells PM localization was not affected by inhibition of PI3K suggesting that the highly abundant $PI(4,5)P_2$ defines tubbyCT PM localization *in vivo* (Santagata *et al*., 2001).

Fluorescently tagged tubbyCT was introduced as a $PI(4,5)P_2$ sensor in 2008 (Quinn, Behe and Tinker, 2008). But although it bound the PM under resting conditions, no translocation was observed following $PI(4,5)P_2$ depletion by activation of PLCβ. This was understood to reflect a high $PI(4,5)P_2$ affinity (Quinn, Behe and Tinker, 2008; Szentpetery *et al.*, 2009), but later experiments involving the step-wise depletion of $PI(4,5)P_2$ by VSPs disproved this explanation. Thus, tubbyCT displayed a lower $PI(4,5)P_2$ affinity than PLCδ1-PH (Halaszovich, Schreiber and Oliver, 2009). However, this is obviously at odds with the reluctance to dissociate from the PM following PLCβ activation. Nevertheless, lowering the $PI(4,5)P_2$ affinity of tubbyCT by mutating the binding pocket resulted in PLCβ-induced translocation of the sensor into the cytoplasm (Quinn, Behe and Tinker, 2008). Although an important advantage of the tubbyCT

sensor compared to PLCδ1-PH is the total lack of $I(1,4,5)P_3$ binding affinity (Quinn, Behe and Tinker, 2008; Szentpetery *et al*., 2009), the enigmatic behavior of tubbyCT wildtype upon PLCβ activation limited the usage of tubbyCT as a default $PI(4,5)P_2$ sensor.

1.6 Aim of the study

$PI(4,5)P_2$ is an important signaling lipid at the PM which is implicated in a huge variety of independent cellular processes (reviewed in Schink, Tan and Stenmark, 2016). In order to achieve its multifunctionality, its dynamics must be temporarily but also spatially tightly controlled. It has been postulated that functionally distinct PM $PI(4,5)P_2$ pools exist which differ in their lipid and protein composition and also in their accessibility to $PI(4,5)P_2$ modifying enzymes (reviewed in Kwiatkowska, 2010).

$PI(4,5)P_2$ dynamics are typically imaged by use of lipid biosensors. $PI(4,5)P_2$ sensors which target individual $PI(4,5)P_2$ pools and thus allow imaging of a specific lipid subpopulation are important tools to investigate $PI(4,5)P_2$ multifunctionality (reviewed in Hammond and Balla, 2015). Such pool-specific $PI(4,5)P_2$ sensors have been artificially constructed e.g. by fusion of PLCδ1-PH and auxilin to study $PI(4,5)P_2$ dynamics during endocytosis (He *et al*., 2017). However, also the pure lipid binding domains PLCδ1-PH and tubbyCT might be recruited to distinct $PI(4,5)P_2$ pools as they behave differently following PLCβ activation (Quinn, Behe and Tinker, 2008; Szentpetery *et al*., 2009). Hence, in a first set of experiments, I tested the hypothesis that PLCδ1-PH and tubbyCT target different $PI(4,5)P_2$ pools. I also investigated whether segregation into distinct pools can explain their diverging behavior following PLCβ activation.

I concluded from these first experiments, that indeed, tubbyCT preferentially bound a $PI(4,5)P_2$ pool which was only barely detected by PLCδ1-PH. Interestingly, this $PI(4,5)P_2$ pool was refilled during PLCβ activation whereas $PI(4,5)P_2$ in the bulk membrane was depleted simultaneously. In fact, PLCβ activation not only leads to $PI(4,5)P_2$ hydrolysis, rising Ca^{2+} levels also initiate a fast $PI(4,5)P_2$ resynthesis which critically depends on PI transfer from the ER to the PM (reviewed in Pemberton, Kim and Balla, 2020). This PI transfer takes place at E-Syt-rich ER-PM junctions (Chang *et al*., 2013; Kim *et al*., 2015; Chang and Liou, 2015). Hence, I next examined whether tubbyCT associates with ER-PM junctions and which lipid and protein determinants

target it to these contact sites. Thereby, I also examined to what extent tubbyCT can be used as reliable sensor to detect PI(4,5)P_2 resynthesis at ER-PM junctions.
Next, I was interested whether the identified association of tubbyCT to E-Syt3 rich ER-PM junctions is also valid for the full-length tubby protein and its close relative TULP3. I further studied the function of tubby at E-Syt3 rich ER-PM contact sites.

2 Methods

2.1 Cell culture

Chinese Hamster Ovary (CHO) dhFr$^-$ cells were cultured in MEM Alpha medium (gibco, ThermoFisher Scientific, Waltham, US), COS-7, Madin-Darby Canine Kidney (MDCK) and Opossum Kidney (OK) cells in DMEM GlutaMAX^{TM}-I medium (gibco). All media were supplemented with 10% fetal calf serum, 1% penicillin and 1% streptomycin. Cells were kept at 37°C and 5% CO_2. For TIRF experiments cells were plated on glass bottom dishes (WillCo Wells B.V., Amsterdam, The Netherlands) or in glass bottom µ-slide VI $^{0.5}$ flow chambers (ibidi, Martinsried, Germany). For protein and RNA extraction cells were grown on polystyrene dishes (Cellstar®, Greiner Bio-One, Kremsmünster, Austria). 48 h post seeding cells were transfected using JetPEI® DNA Transfection Reagent (CHO dhFr$^-$ cells, Polyplus Transfection, Illkirch-Graffenstaden, France) or lipofectamin®2000 Reagent (COS-7, MDCK and OK cells, Invitrogen, by Thermo Fischer Scientific, Waltham, US) and following manufacturer's instructions. Typically, transfected DNA amount (340 µg/cm^2 culture dish area) was equally distributed among transfected plasmids. But for experiments which involved the activation of PLCβ, cells were transfected with equal total amounts of human muscarinic receptor 1 (M1R, 114 µg/cm^2) independent of additionally transfected plasmids. This procedure should ensure comparable M1R expression and thus comparable PLCβ activation between different experimental settings. Experiments were performed 24 h (TIRF measurements) and 48 h (protein extraction) after transfection.

2.2 Molecular biology

Expression vectors used in this study are listed in Table 1.

pEGFP-C1-tubbyCT R332H and Y343F point mutations were inserted by Gisela Fischer and Eva Naudascher, respectively using QuikChange II XL Site-Directed mutagenesis kit (Stratagene, Agilent Technologies, Santa Clara, US). pEGFP-C1-tubbyCT KR330/332AA and Nir2-mcherry S164A point mutations were inserted by me and Lea Schultz, respectively using PfuUltra II Hotstart PCR Master Mix (Agilent Technologies).

Table 1: Used expression vectors

Species	Gene	Gene ID Number	Vector	Citation/Source
human	M1R	NM_000738.2	pSGHV0	
human	PLCδ1-PH (aa 1-170)	NM_006225.3	pEGFP-N1	Várnai and Balla, 1998; obtained from T. Balla
			pcDNA3-YFP(mono)	generated in Oliver lab
			pCFP(mono)	generated in Oliver lab
rat	epsin1-ENTH (aa 1-158)	NM_057136.1	pEGFP-N1	Leitner *et al*., 2019
mouse	tubbyCT (aa 243-505)	NM_021885.4	pEGFP-C1	Santagata *et al*., 2001; obtained from L. Shapiro
			pRFP-C1	generated in Oliver lab
			pEYFP-C1	generated in Oliver lab
			pECFP-C1	generated in Oliver lab
mouse	tubbyFL	NM_021885.4	pEGFP-C1	Santagata *et al*., 2001; obtained from L. Shapiro
human	TULP3	NM_003324.4	pGLAP1	Mukhopadhyay *et al*., 2010; obtained from S. Mukhopadhyay
rat	PKCγ-C1 (aa 26-89)	NM_012628.1	pEGFP-N1	Oancea *et al*., 1998; obtained from T. Meyer
Legionella pneumophila	P4M-SidMx1	DQ845395	pEGFP-C1	Hammond, Machner and Balla, 2014; obtained from G. Hammond
	lyn11		pECFP (mono)-N2	Inoue *et al*., 2005; generated in Oliver lab
	lyn11-FRB		pRFP-N1	generated in Oliver lab
human	E-Syt1	NM_015292	pEGFP-C1	Giordano *et al*., 2013
			pRFP-C3	generated in Oliver lab
human	E-Syt2	NM_020728.1	pEGFP-C1	Giordano *et al*., 2013
			pRFP-C3	generated in Oliver lab

Continuation Table 1:

Species	Gene	Gene ID Number	Vector	Citation/Source
human	E-Syt3	NM_031913	pEGFP-C1	Giordano *et al*., 2013
			pRFP-C3	generated in Oliver lab
human	Nir2-mcherry	AF334584.1		Chang *et al*., 2013; obtained from J. Liou
human	Nir3-mcherry	AB385472		Chang and Liou, 2015; obtained from J. Liou
Ciona intestinalis	VSP	AB183035.1	pRFP-C1	Murata *et al.*, 2005; obtained from Y. Okamura
	empty vector		pRFP-C1	
	empty vector		pEGFP-C1	
	empty vector		pEYFP (mono)-C1	generated in Oliver lab

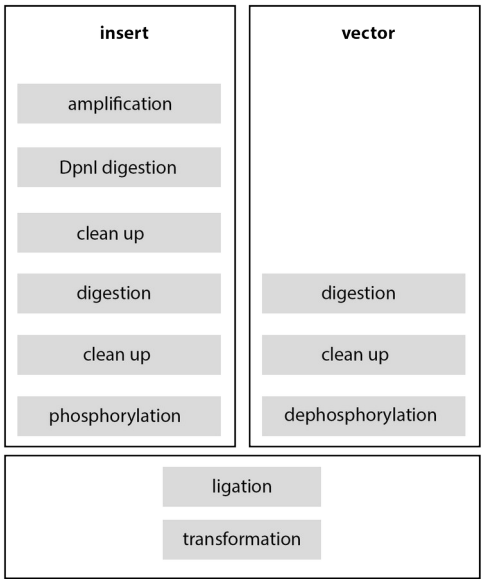

Figure 2.1: Scheme of subcloning procedure

Subcloning was performed following the scheme in Figure 2.1. In brief, the insert was amplified from template vector using primers with integrated restriction sites. If any short additional sequence (coding for e.g. a linker or myc tag) was desired in the final construct it was also included in the primer sequence. Following insert amplification template DNA was digested by DpnI and PCR product was cleaned up. Amplified insert and desired vector were digested independently but with the same restriction enzymes to

generate matching DNA overhangs. Digestions were performed with two different restriction enzymes to avoid vector religation and to ensure unidirectional insert integration. Digestions were cleaned up. If necessary, vector backbone was cleaned up from ethidiumbromid-containing agarose gel. Following insert phosphorylation and vector backbone dephosphorylation, DNA amount was estimated from an ethidiumbromid-containing agarose gel. Ligation was performed with an approximately 6-fold excess of insert to increase chance of integration into the vector backbone. Subsequently, ligated DNA was transformed into chemo-competent *Escherichia coli* DH5α or XL10 Gold cells. Used protocols for the individual subcloning steps are listed in Table 2.

Table 2: Protocols of individual subcloning steps
* = Thermo Fisher Scientific, Waltham, US; ** = Agilent Technologies, Santa Clara, US; *** GeneAll Biotechnology, Seoul, South Korea.

<table>
<tr><th>method</th><th>reaction mix</th><th>protocol</th></tr>
<tr><td rowspan="2">PCR</td><td>1 µl template (100µM)
5 µl Pfu buffer (*)
1 µl forward primer (10 µM)
1 µl reverse primer (10 µM)
1 µl dNTPs, (10 mM each, *)
39 µl water
1 µl Pfu DNA Polymerase (*)</td><td>
<table>
<tr><th>Step</th><th>Temp.</th><th>time</th><th>cycle</th></tr>
<tr><td>1</td><td>95°C</td><td>3 min</td><td></td></tr>
<tr><td>2</td><td>95°C</td><td>30 s</td><td rowspan="3">25x</td></tr>
<tr><td>3</td><td>A_T</td><td>30 s</td></tr>
<tr><td>4</td><td>68°C</td><td>E_{time}</td></tr>
<tr><td>5</td><td>68°C</td><td>2x E_{time}</td><td></td></tr>
</table>
</td></tr>
<tr><td>1 µl template (100µM)
1 µl forward primer (10 µM)
1 µl reverse primer (10 µM)
22 µl water
25 µl PfuUltra II Hotstart PCR 2x Master Mix (**)</td><td>
<table>
<tr><th>Step</th><th>Temp.</th><th>time</th><th>cycle</th></tr>
<tr><td>1</td><td>95°C</td><td>3 min</td><td></td></tr>
<tr><td>2</td><td>95°C</td><td>30 s</td><td rowspan="3">25x</td></tr>
<tr><td>3</td><td>A_T</td><td>30 s</td></tr>
<tr><td>4</td><td>72°C</td><td>E_{time}</td></tr>
<tr><td>5</td><td>72°C</td><td>2x E_{time}</td><td></td></tr>
</table>
</td></tr>
<tr><td>DpnI digestion</td><td>1 µl DpnI, 10 U/µl (*)
added to PCR mix</td><td>1 h at 37°C</td></tr>
<tr><td>PCR product digestion</td><td>5 µl 10x FD Green buffer (*)
1 µl FD restriction enzyme 1 (*)
1 µl FD restriction enzyme 2 (*)
44 µl cleaned up PCR product</td><td>20 min at 37°C</td></tr>
</table>

Continuation Table 2:

method	reaction mix	protocol
Vector digestion	5 µl 10x FD Green buffer (*) 1 µl FD restriction enzyme 1 (*) 1 µl FD restriction enzyme 2 (*) 3 µl vector (1 µg/µl) 40 µl water	20 min at 37°C
DNA clean up	Expin™ Gel Kit (***)	Following manufacturer's instructions
phosphorylation	14.5 µl cleaned up insert DNA 2 µl 10x buffer A (PNK) (*) 1 µl ATP (10 mM) (*) 2.5 µl T4 PNK, 10 U/µl (*)	1 h at 37°C, 10 min at 75°C
dephosphorylation	7 µl cleaned up vector DNA 1 µl 10x buffer (FastAP) (*) 2 µl FastAP, 1 U/µl (*)	1 h at 37°C, 10 min at 75°C
ligation	1 µl vector x µl insert 1 µl T4 DNA Ligase, 5 U/µl (*) 2 µl T4 DNA Ligase buffer (*) 16-x µl water	Mix vector and insert, incubate 2 min at 70°C, put on ice, add water, buffer and ligase, incubate at 4°C overnight or at 22°C, 2 h
transformation		defreeze bacteria on ice, add 20 µl ligation mix, incubate 30 min on ice, heat-shock: 42°C, 40 s, incubate 2 min on ice, add 1 ml SOC medium, incubate 1 h at 37°C, plate on LB plates with antibiotics

Subcloning strategies for individual constructs are subsequently described:

CFP-E-Syt3 was generated by exchanging the EGFP portion of the pEGFP-C1-E-Syt3 construct with CFP using AgeI and BsrG1 restriction sites.

N-terminal myc tag was added to tubbyCT via PCR amplification and PCR product was subcloned into pcDNA3.1 using BamH1 and Not1 restriction sites. N-terminally myc-tagged PLCδ1-PH construct was generated by exchanging the tubbyCT portion of pcDNA3.1-myc-tubbyCT with PLCδ1-PH using EcoRI and Not1 restriction sites. N-terminally myc-tagged E-Syt1 construct was generated by exchanging EGFP-E-Syt1 of the pEGFP-N1-E-Syt1 plasmid with PCR amplified myc-E-Syt1 by use of AgeI and EcoRV restriction sites. In all generated myc-tagged constructs the original start codon was removed.

pRFP-C1-E-Syt deletion constructs (E-Syt1ΔHP (AA 125-1105), E-Syt2ΔHP (AA 106-846), E-Syt3ΔHP (AA 104-887), E-Syt3C2ABC (AA 296-887), E-Syt3C2BC (AA 439-887), E-Syt3C2C-L (AA 568-877) and E-Syt3C2C (AA 745-887)) were generated by PCR amplification of E-Syt portions and subcloning into pRFP-C1 using BsrG1 and Sal1 (E-Syt1ΔHP), BglII and BamH1 (E-Syt2ΔHP) and HindIII and KpnI (E-Syt3 deletion constructs) restriction sites, respectively. Subcloning of E-Syt3C2BC and E-Syt3C2C-L was conceived by me and performed by the student assistant Lea Schultz under my supervision.

2.3 Detection of gene expression at mRNA level

Gene expression was assessed at mRNA level by end-point reverse transcription polymerase chain reaction (RT-PCR). Therefore, RNA was isolated from non-transfected cells and reverse transcribed into cDNA. Gene-specific cDNA was subsequently amplified by PCR. PCR efficiency was semi-quantitatively evaluated at an ethidiumbromid-containing agarose gel and compared to the expression level of the house-keeping gene glyceraldehyde 3-phosphate dehydrogenase (GAPDH).

2.3.1 RNA extraction

For RNA extraction cells were grown on 6 cm polystyrene dishes (Cellstar®, Greiner Bio-One). 48 h after seeding culture medium was removed from non-transfected cells, 2.1 ml peqGOLD RNAPure™ reagent (VWR International, Radnor, US) was added and incubated for 5 min at room temperature. Cells were detached using a cell scraper and equally distributed to two 1.5 ml reaction tubes. 0.21 ml phenol:chloroform:isoamyl alcohol (25:24:1) was added to each tube, mixture was properly vortexed (15 s) and incubated for 6 min on ice. The aqueous RNA-containing phase was separated from the organic phase by centrifugation (12000 g, 5 min, 4°C) and transferred into a new reaction tube. For RNA precipitation equal amount of isopropanol was added, mixed and incubated for 15 min on ice. After 10 min centrifugation (12000 g, 4°C), supernatant was removed, pellet was washed twice with 75% ethanol and subsequently dried. Isolated RNA was dissolved in 25 µl RNAse-free water.

As an alternative to the described phenol-chloroform extraction, RNA was isolated using the Quick-RNA Miniprep Kit (ZymoResearch, Irvine, US) following manufacturer's instructions. In brief, cells were disrupted by incubation in provided lysis

buffer, cell debris was removed by centrifugation. Genomic DNA was removed from cell lysate by binding to the Spin-Away™ Filter, RNA-containing flow through was diluted with ethanol and loaded on a Zymo-Spin™ IIICG column. Remaining DNA was in-column digested by DnaseI. Column-bound RNA was further washed and finally diluted in RNAse-free water.

Content and quality of isolated RNA was accessed by a microvolume spectrophotometer (Thermo Scientific™ NanoDrop 2000).

2.3.2 Reverse transcription polymerase chain reaction

First-strand cDNA was generated from isolated RNA using SuperScript™ II Reverse Transcriptase (RT) (Invitrogen, by Thermo Fischer Scientific, Waltham, US) following manufacturer's instructions. In brief, 1 µg RNA was diluted to 10 µl in RNA-free water and incubated with 0.5 µl random hexamer primers (10 µM) for 10 min at 70°C. 5µl 5x RT buffer, 1.2 µl dNTPs (10 mM each), 2.5 µl 0.1 M DTT, 4.8 µl RNA-free water and 1 µl RT enzyme was added and incubated for 50 min at 42°C, followed by 10 min at 70°C.

For gene-specific cDNA amplification, 2 µl first-strand cDNA was mixed with 1 µl gene-specific forward (10 µM) and 1 µl gene-specific reverse primer (10 µM), 5 µl 10x DreamTaq buffer (Thermo Fisher Scientific), 1 µl dNTPs (10 mM each, Thermo Fisher Scientific), 39 µl water and 1 µl DreamTaq DNA Polymerase (5 U/µl, Thermo Fisher Scientific). Used PCR protocol is shown in Table 3, gene-specific primers are listed in Table 4. If necessary, nested PCRs were performed, using 2 µl of obtained PCR product as template and gene-specific nested forward and nested reverse primers (10 µM each). PCR protocol shown in Table 3 was also used for nested PCRs.

Table 3: PCR protocol used for gene-specific cDNA amplification

	Temperature	Time	Cycle
Denaturation	95°C	3 min	
Denaturation	95°C	30 s	40x
Annealing	60°C	30 s	
Elongation	72°C	30 s	
Final Elongation	72°C	3 min	

Table 4: Gene-specific primer and nested primer pairs used for cDNA amplification
For: forward primer; Rev: reverse primer; nFor: nested forward primer; nRev: nested reverse primer. All melting temperatures (T_M) are salt adjusted and were calculated from oligo sequences using OligoCalc (http://biotools.nubic.northwestern.edu/OligoCalc.html).

	CHO cells			COS-7 cells		
Gene	Primer sequence		T_M [°C]	Primer sequence		T_M [°C]
GAPDH	For	aactttggcattgtggaagg	56.4	For	aactttggtatcgtggaagg	56.4
	Rev	ctctgttgctgtagccaaat	56.4	Rev	ccctgttgctgtagccaaat	58.4
E-Syt1	For	catggtgacagcccctc	57.3	For	acacatgttgacagtccctt	56.4
	Rev	ctgcccttatctttgtcatc	56.4	Rev	ctgcccttgtccttgtcgtc	56.3
E-Syt2	For	gaaatgggaccaccctgg	58.4	For	gacaaagaccaagccaacg	57.5
	Rev	ccacgtgtgttttccttctc	58.4	Rev	gccttggagacccagac	57.3
E-Syt3	For	aacccttttgactacctgaatg	58.4	For	aacccttttgactacctgaatg	58.4
	Rev	aaggcacacatagcgcact	57.5	Rev	caaggcaaatctgtagggc	57.5
	nFor	aaaactctccaggtttgcccaa	57.5			
	nRev	cttgtcacatctgcaggg	56.3			
VAP-A	For	gtctgtctgtctcttttaacc	57.5	For	aagatggacctatgccaaaac	57.5
	Rev	aagcaatccctggtggag	56.3	Rev	gaatccaatgaaaatggctgc	57.5
VAP-B	For	gcctctctcaacgtgtcg	58.4	For	gtctaagtctctgagttcttc	57.5
	Rev	ctacatcgtgtggtttagcg	58.4	Rev	ggccttcttccttcccag	58.4
Nir2	For	ggaactagcagcactgcc	58.4	For	ccacttctactagcggtg	56.3
	Rev	gggaggcaaaggcatcg	57.3	Rev	actaccgtgtcgctcgc	57.3
Nir3	For	gagcccagcagcagcaa	57.3	For	ggccttccaagagcatgc	58.4
	Rev	atgaatcgtggagggtgga	57.5	Rev	ctgatgtccagctcaggg	58.4
				nFor	gaagtcgctgcaaagtggt	57.5
				nRev	ccaagatgctggagttgtc	57.5
Septin4	For	ggcagatacactgacacct	57.5	For	caagcgtttcctggagga	56.3
	Rev	cgttcctttactactagacg	56.4	Rev	ctggttgtcagcggactg	58.4
	nFor	tgaagtggaccgaaagaaatg	57.5			
	nRev	ctcataatgtgtctctcggg	58.4			
Septin5	For	ccatcaccgactatgtgga	57.5	For	caaagctgactgtcttgtcc	58.4
	Rev	cactgggaaccaggcag	57.3	Rev	tctccatgcggctgtcct	58.4

Table 5: Gene-specific CHO cell E-Syt3 primer and nested primer pairs
For: forward primer; Rev: reverse primer; nFor: nested forward primer; nRev: nested reverse primer. All melting temperatures (T_M) are salt adjusted and were calculated from oligo sequences using OligoCalc (http://biotools.nubic.northwestern.edu/OligoCalc.html).

	Primer sequence		T_M [°C]	Nested primer sequence		T_M [°C]
RT-PCR 1	For	ttcttgctcactgggcaca	57.5			
	Rev	ttggcaaacctggagagtttt	57.5			
RT-PCR 2	For	aaaactctccaggtttgccaa	57.5			
	Rev	tgctcagctgtcacactg	56.3			
RT-PCR 3	For	ccaaaaataaagccagcagag	57.5	nFor1	cagtgtgacagctgagca	56.3
	Rev	aaggcacacatagcgcact	57.5	nRev1	cttgtcacatctgcaggg	56.3
				nRev2	ctgggatggggttttgtgatc	61.2
RT-PCR 4	For	aacccttttgactacctgaatg	58.4	nFor	ccaaaaataaagccagcagag	57.5
	Rev	aaggcacacatagcgcact	57.5	nRev	cttgtcacatctgcaggg	56.3
RT-PCR 5	For	aacccttttgactacctgaatg	58.4	nFor	ccaaaaataaagccagcagag	57.5
	Rev	cttgtcacatctgcaggg	56.3	nRev	tgctcagctgtcacactg	56.3

PCR products were loaded on an ethidiumbromid-containing 2% agarose gel and verified by Sanger sequencing (Microsynth Seqlab GmbH, Göttingen, Germany).

Amplification of E-Syt3 from CHO cell cDNA was not successful using the primer pairs annotated in Table 4. Amplification was further attempted using more primer and nested primer pair combinations (Table 5).

2.4 Co-immunoprecipitation

Co-immunoprecipitation (Co-IP) serves to identify and study direct and indirect protein-protein interactions. For this purpose, protein complexes are precipitated by binding of one complex component to bead-coupled antibodies. Isolated complexes can be subsequently analyzed by SDS-PAGE, Western Blot or mass spectrometry (Figure 2.2).

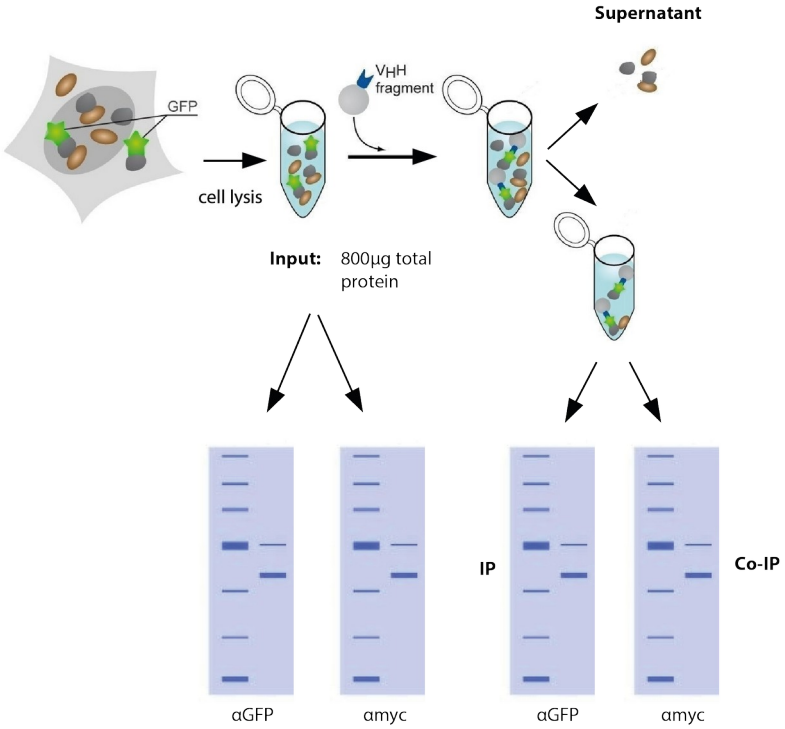

Figure 2.2: Principle of performed co-immunoprecipitation
GFP- and myc-tagged proteins were harvested from CHO dhFr$^-$ cells, complexes were immunoprecipitated by αGFP nanobodies and subsequently analyzed by SDS-PAGE and Western Blot. Figure was modified from
https://www.antikoerper-online.de/resources/17/874/gfp-trap/ (09/27/2020).

2.4.1 Protein extraction and complex precipitation

CHO cells were co-transfected with myc- and GFP-fused constructs. Proteins were harvested 48 h post transfection. Therefore cells were washed in Phosphate Buffered Saline (PBS, recepy Table 6) and thereupon lysed in 50 mM Tris, 150 mM NaCl, 10 mM EDTA, 1% Triton X-100, pH = 7.2, 1% protease inhibitor cocktail (Roche) for 30 min. For better disruption, cells were 3x squeezed through a hypodermic needle (Ø 0.40 x 20 mm, 27 G x ¾, Gr. 20, Sterican®, B.Braun, Melsungen, Germany) during lysis. Cell debris was removed from cell lysate by centrifugation (21000 g, 4°C, 20 min). Protein content of supernatant was assessed by a microvolume

spectrophotometer (Thermo Scientific™ NanoDrop 2000) and 800 ng total protein was diluted with 600 µl dilution buffer (10 mM Tris, 150 mM NaCl, 0.5 mM EDTA, pH = 7.5). For immunoprecipitation (IP) αGFP nanobodies covalently bound to agarose beads (GFP-Trap®_A, Chromotech, Planegg-Martinsried, Germany) were used. 25 µl beads were 3x equilibrated in dilution buffer and thereupon incubated with diluted protein for 1 h at 4°C. For better binding mixture was rotated constantly. Beads were isolated by centrifugation (2500 g, 4°C, 2 min), 3x washed in dilution buffer followed by 3 washing steps in 10 mM Tris, 500 mM NaCl, 0.5 mM EDTA, pH = 7.5. All washing steps took place under rotation. Immunocomplexes were dissociated from beads by incubation in 2x SDS buffer (20% v/v glycerol, 100 mM Tris, 115 mM DTT, 6.5% w/v SDS, 0.013% (w/v) bromphenol blue) (95°C, 10 min). Beads were removed by centrifugation (2500 g, 2 min), supernatant was used for Western Blot analysis.

2.4.2 SDS-PAGE and Western Blot

Denaturated protein lysates (30 µg total protein in SDS buffer) and immunoprecipitated protein complexes were run on a 10% SDS-polyacrylamide gel and subsequently plotted onto a nitrocellulose membrane (PROTRAN BA 85, 045 µm, Whatman plc, Maidstone, UK) (188 mA, 2.5 h). Recipes of stacking and running gels as well as of running and transfer buffers and PBS are listed in Table 6.

Nitrocellulose membrane was blocked overnight in 5% milk powder in PBST (1x PBS, pH = 7.4 + 0.05% Tween). After 3 washing steps (10 min each) in PBST, membrane was incubated with primary antibody (1:200 in PBST) under rotation for 1.5 h at room temperature. Blot was washed in PBST (2x 5 min) and subsequently incubated under rotation for 2 h at 4°C in secondary antibody (1:5000 in PBST). For detection of GFP-tagged proteins rabbit polyclonal IgG anti-GFP (FL) (1:200; sc-8334 Santa Cruz Biotechnology, Dallas, US) primary antibody and goat αrabbit (IRDye® 800CW) (1:5000, 926-32211, Li-cor Biosciences, Bad Homburg, Germany) secondary antibody was used. Co-immunoprecipitated myc-tagged protein were detected by mouse monoclonal IgG anti-c-Myc (1:200; sc-40 Santa Cruz Biotechnology) primary antibody and donkey αmouse (IRDye® 800CW) (1:5000, 926-32212, Li-cor Biosciences) secondary antibody. After final washing steps (2x 10 min in PBST, 1x 10 min in PBS) secondary antibodies were detected by an infrared scanner (Li-cor Biosciences).

Table 6: Gel and buffer recipes for SDS-PAGE and Western Blotting

stacking gel	15.6 ml water 3.9 ml acrylamide / N,N-methylenbisacrylamid 2.9 ml 1.5 M Tris pH 6.8 230 µl 10% SDS 23 µl TEMED 230 µl 10% APS
10% running gel	12.3 ml water 10.3 ml acrylamide / N,N-methylenbisacrylamid 7.7 ml 1.5 M Tris pH 8.8 310 µl 10% SDS 23 µl TEMED 310 µl 10% APS
10x SDS running buffer	30 g Tris 150 g Glycin 10 g SDS ad 1 l water
10x transfer buffer	3.03 g Tris 14.4 g Glycin 100 ml methanol ad 1 l water
20x PBS	120.2 g NaCl 4g KCl 35.6 g Na_2HPO_4 x 2 H_2O 5.4 g KH_2PO_4 ad 1 l water

2.4.3 Quantification of co-immunoprecipitation

In all Co-IPs a negative control lysate of cells expressing myc-tubbyCT only was included. In this sample, myc-tubbyCT should not be found in the immunoprecipitated fraction as it should not bind to the αGFP nanobodies. However, a very faint band was observed in some experiments, probably resulting from insufficient bead washing. The intensity of this negative control band was subtracted from the intensities of all other co-immunoprecipitated αmyc bands and resulting values were normalized to immunoprecipitated αGFP band intensities. Thus the relative Co-IP values were calculated with the following formula:

relative Co-IP (sample) = αmyc band intensity Co-IP (sample) - αmyc band intensity Co-IP (neg. control)
/ αGFP band intensity IP (sample)

Band intensities were determined using ImageJ software.

2.5 Fluorescence Resonance Energy Transfer

Fluorescence Resonance Energy Transfer (FRET) is the nonradiative energy transfer from a donor to an acceptor fluorophore through dipole-dipole coupling. The fundamental prerequisite for FRET is an overlap of donor emission spectrum with the acceptor excitation spectrum. Consequently, donor excitation results in acceptor emission (Figure 2.3). FRET efficiency (E_{FRET}) declines with the sixth power of the donor-to-acceptor distance (R) as follows:

$$E_{FRET} = R_0^6/(R_0^6 + R^6)$$

with R_0 being the Förster distance with a FRET efficiency of 50%. Additionally, dipole-dipole interaction, thus donor-to-acceptor orientation, and donor-to-acceptor ratio affect FRET efficiency (reviewed in Sahoo, 2011).

As FRET typically occurs within a distance range of 1-10 nm it is a powerful tool to study protein-protein interactions as well as conformational changes within molecules. Moreover, due to its non-invasiveness, FRET imaging allows the dynamic investigation of such processes.

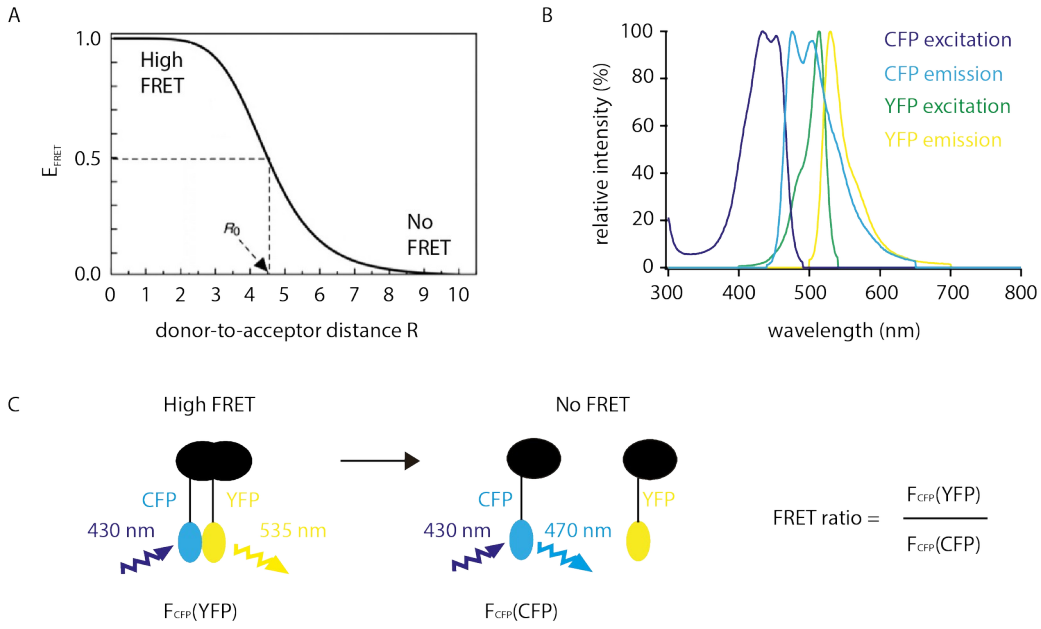

Figure 2.3: Principle of Fluorescence Resonance Energy Transfer
(**A**) FRET efficiency (E_{FRET}) in dependence of the donor-to-acceptor distance. R_0 = Förster distance. Modified from Sahoo, 2011. (**B**) CFP and YFP excitation and emission spectra. Due to overlapping CFP emission and YFP excitation spectra, CFP and YFP represent a typical FRET donor and acceptor pair. (**C**) Experimental setting for probing protein-protein interactions. High FRET is observed during interaction of CFP- with YFP-fused proteins: CFP excitation results in YFP emission. Increasing distance between the proteins of interest reduces FRET and thus results in in reduced YFP and increased CFP emission during CFP excitation.

2.5.1 Experimental Set-up

CFP and YFP constitute a typical FRET pair and were used as donor and acceptor in this study (Figure 2.3). CHO cells were imaged 24 h post transfection with an Eclipse TE2000-U inverted microscope (Nikon, Minato, Japan) equipped with a 40x0.55 LWD objective and an Oligochrome light source (TILL Photonics, Gräfelfing, Germany). For CFP and YFP excitation a 430/24 nm (F49-430, AHF Analysentechnik, Tubingen, Germany) and a 500/20 nm (F49-500, AHF) filter were used, respectively. CFP was excited with 20% and YFP with 27% illumination power. Emmision light passed a tripleband beamsplitter CFP/YFP/mCherry (F68-017, AHF) as well as a 470/23nm (F49, AHF) and a 535/30nm filter for CFP and YFP emission, respectively. Emission light was restricted to a detection area by a uEye camera (TILL Photonics) and detected with photodiodes (TILL Photonics). CFP emission under CFP excitation (F_{CFP}(CFP)), YFP emission under YFP excitation (F_{YFP}(YFP)) as well as YFP emission under CFP excitation (F_{CFP}(YFP)) was recorded. During imaging cells were perfused with extracellular solution (5.8 mM KCl, 144 mM NaCl, 0.9 mM MgCl, 1.3 mM CaCl, 0.7 mM NaH_2PO_4, 5.6 mM D-glucose, 10 mM HEPES, pH = 7.4). Time series with an interval of 3 s were acquired.

2.5.2 Background, bleed through and false excitation correction

During FRET CFP excitation induces YFP emission and thus F_{CFP}(CFP) decreases and F_{CFP}(YFP) increases with rising FRET. FRET ratios can be calculated with the following formula:

$$\text{FRET ratio} = F_{CFP}(\text{YFP}) / F_{CFP}(\text{CFP}).$$

However, by use of above described excitation and emission filters, the CFP/YFP spectral overlap also causes substantial bleed through of CFP into the YFP emission channel especially during CFP excitation, but also during YFP excitation. Moreover, CFP excitation at 430 nm causes direct false YFP excitation (Figure 2.5). Consequently, CFP and YFP directly influence F_{CFP}(YFP) even without occurring FRET. Additionally, background signals distort measured fluorescences. Thus, original data needs to be appropriately corrected before used for FRET ratio calculations. To this end, the ratios of background fluorescence, bleed through and false excitation were experimentally determined and F_{CFP}(YFP), F_{CFP}(CFP) and F_{YFP}(YFP) were corrected accordingly. As correction values depend on experimental parameters such as illumination power, all

recording settings were kept constant throughout all measurements.

Background correction:

Recorded background signals predominantly depend on the size of the detection area. Thus, to determine the background signals, F_{YFP}(YFP), F_{CFP}(CFP) and F_{CFP}(YFP) of non-transfected cells were recorded and correlated to the size of the detection area. The following correlations were determined by linear fitting of measured data points (Figure 2.4):

$$\text{background } F_{YFP}(YFP) = 3.48\text{x}10^{-7} (\pm 1.29\text{x}10^{-8}) \text{ x detection area (pixel)}$$

$$\text{background } F_{CFP}(CFP) = 8.45\text{x}10^{-7} (\pm 2.03\text{x}10^{-8}) \text{ x detection area (pixel)}$$

$$\text{background } F_{CFP}(YFP) = 1.64\text{x}10^{-6} (\pm 5.19\text{x}10^{-8}) \text{ x detection area (pixel)}$$

Respective background signals were subtracted from fluorescences recorded in all other measurements.

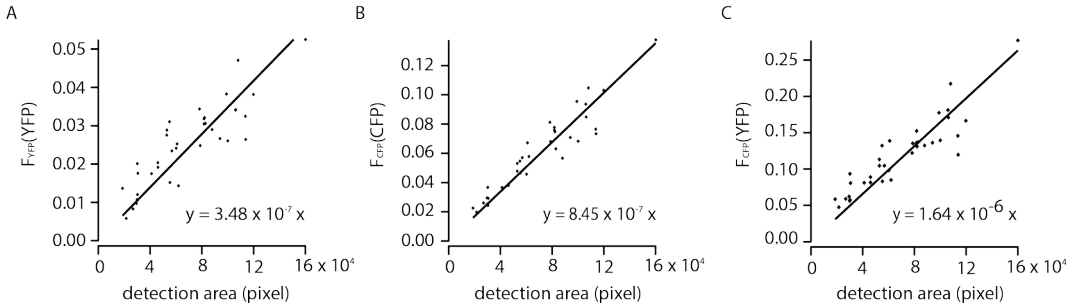

Figure 2.4: Background fluorescences
Fluorescence of non-transfected CHO cells in dependence of the detection area. (**A**) F_{YFP}(YFP) (**B**) F_{CFP}(CFP) (**C**) F_{CFP}(YFP). n = 36 cells.

Determination of CFP bleed through into YFP emission:

CFP fluorescence is typically detected at ~470 nm. However, it is also emitted quite substantially at 535 ±15 nm, the wavelengths transmitted by the YFP emission filter (Figure 2.5A). To detect the fractions of direct CFP bleed through into the YFP emission channel, cells were transfected with the donor lyn-CFP only and F_{CFP}(CFP), F_{YFP}(YFP) and F_{CFP}(YFP) was recorded.

For determination of CFP bleed through during CFP excitation, F_{CFP}(YFP) was plotted against F_{CFP}(CFP). Data was fitted linearly and the so-called Donor Excitation Ratio (DER) was determined from the linear slope (Figure 2.5B):

$$DER = F_{CFP}(YFP) / F_{CFP}(CFP) = 0.790 \pm 0.00776$$

CFP is also slightly excited during YFP excitation settings and hence, also shows a certain bleed through into the YFP emission signal during YFP excitation (F_{YFP}(YFP)).

In order to determine this so called RD2 ratio, F_{YFP}(YFP) was plotted against F_{CFP}(CFP). Data points were fitted linearly and RD2 was determined from the linear slope (Figure 2.5C):

$$RD2 = F_{YFP}(YFP) / F_{CFP}(CFP) = 0.00978 \pm 0.000207$$

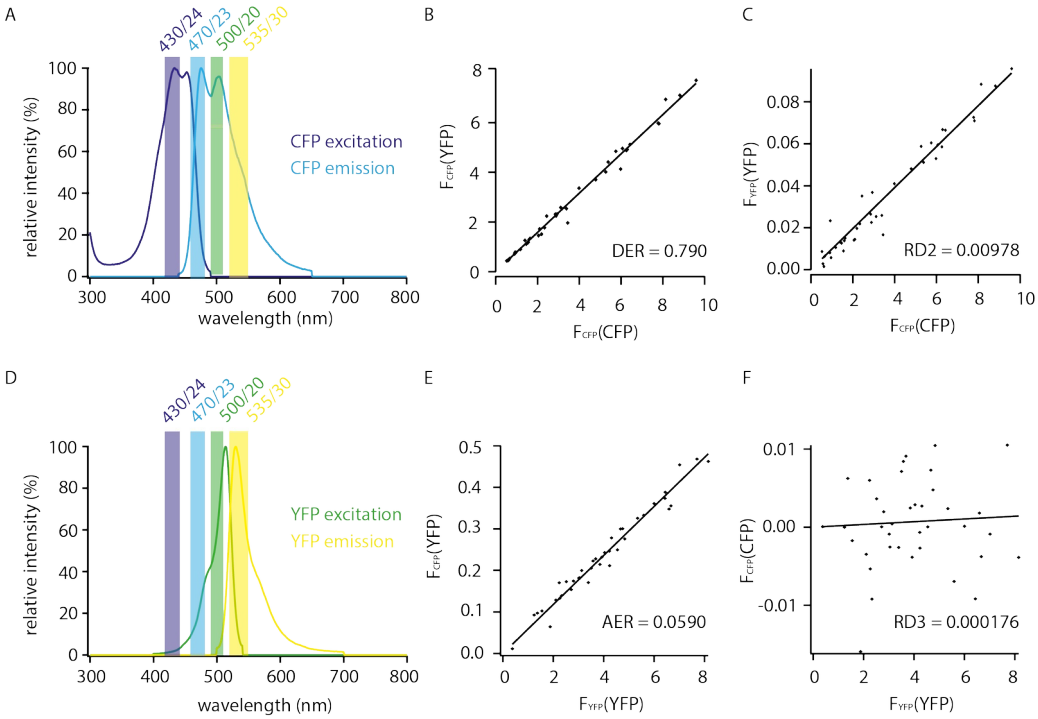

Figure 2.5: CFP bleed through and YFP false excitation
(**A-C**) For determination of CFP bleed through into YFP emission channels, CHO cells were transfected with donor (lyn-CFP) only and F_{YFP}(YFP), F_{CFP}(CFP) and F_{CFP}(YFP) were recorded. (**A**) CFP excitation and emission spectra. Filter sets are highlighted: dark blue = CFP excitation filter; light blue = CFP emission filter; green = YFP excitation filter; yellow = YFP emission filter. (**B**) Correlation of F_{CFP}(YFP) to F_{CFP}(CFP). Donor excitation ratio (DER) was determined from the slope of the linear fit of measured data points. n = 39 cells. (**C**) Correlation of F_{YFP}(YFP) to F_{CFP}(CFP). RD2 was determined from the slope of the linear fit of measured data points. n = 39 cells. (**D-E**) For determination of false YFP excitation, CHO cells were transfected with acceptor (YFP-PLCδ1-PH) only and F_{YFP}(YFP), F_{CFP}(CFP) and F_{CFP}(YFP) were recorded. (**D**) YFP excitation and emission spectra. Filter sets are highlighted in the same colours as in (A) (**E**) Correlation of F_{CFP}(YFP) to F_{YFP}(YFP). Acceptor excitation ratio (AER) was determined from the slope of the linear fit of measured data points. n = 30 cells. (**F**) Correlation of F_{CFP}(CFP) to F_{YFP}(YFP). RD3 was determined from the slope of the linear fit of measured data points. n = 30 cells.

<u>Determination of false YFP excitation at 430 nm:</u>

CFP excitation at 430 nm also directly excites YFP (Figure 2.5D). In order to determine this false YFP excitation, cells were transiently transfected with acceptor (PLCδ1-PH-YFP) only and F_{CFP}(CFP), F_{YFP}(YFP) and F_{CFP}(YFP) were measured.

For determination of the direct YFP emission into the F_{CFP}(YFP) channel, the so-called

Acceptor Excitation Ratio (AER) was determined. F_{CFP}(YFP) was plotted against F_{YFP}(YFP) and data points were fitted linearly. AER was determined from the linear slope (Figure 2.5E):

$$AER = F_{CFP}(YFP) / F_{YFP}(YFP) = 0.0590 \pm 0.0015$$

YFP also slightly emits at 470 ± 12.5 nm, the wavelength transmitted by the CFP emission filter. Hence, I additionally identified the YFP fraction in F_{CFP}(CFP). Therefore F_{CFP}(CFP) was plotted against F_{YFP}(YFP) and the so-called RD3 ratio was determined from the slope of the linear fit of the respective data points (Figure 2.5F):

$$RD3 = F_{CFP}(CFP) / F_{YFP}(YFP) = 0.000176 \pm 0.000418$$

As detected YFP signal was very low and the error relatively high, RD3 was no further taken into account.

Bleed through and false excitation correction:

F_{CFP}(YFP) and F_{YFP}(YFP) were subsequently bleed through and false excitation corrected. The following formula were used:

$$\text{corrected } F_{CFP}(YFP) = F_{CFP}(YFP) - [F_{YFP}(YFP) - RD2 \times F_{CFP}(CFP)] \times AER - F_{CFP}(CFP) \times DER$$

$$\text{corrected } F_{YFP}(YFP) = F_{YFP}(YFP) - RD2 \times F_{CFP}(CFP)$$

Because RD3 ~ 0 correction of F_{CFP}(CFP) was not necessary. The corrected fluorescence intensities were subsequently used for FRET ratio and acceptor-to-donor ratio calculations.

2.6 Total Internal Reflection Fluorescence Microscopy

Total Internal Reflection Fluorescence (TIRF) microscopy was first described in 1981 by Daniel Axelrod and represents an imaging method which allows selective visualization of cellular structures in close proximity to the glass-specimen interface (Figure 2.6).

In contrast to other fluorescence microscopy methods, fluorophores are excited by the so-called evanescent field. It is generated if light is totally reflected at the interface of two transparent media with different refractive indices. The energy of the evanescent wave declines exponentially with the perpendicular distance to the interface as follows:

$$I(z) = I(o)e^{-z/d}$$

with I describing the evanescent field intensity at the interface (I(o)) and at a distance z

from the interface (I(z)). d represents the characteristic evanescent wave penetration depth which depends on the refractive indices n of the two transparent media, the light wavelength λ and the incidence angle α_1:

$$d = \lambda/4\pi(n_1^2\sin^2\alpha_1 - n_2^2)^{-1/2}$$

TIRF images show a high z-axis resolution and a good signal-to-noise ratio. Penetration depths below 100 nm facilitate imaging of the plasma membrane and underlying structures (reviewed in Sezgin and Schwille, 2011).

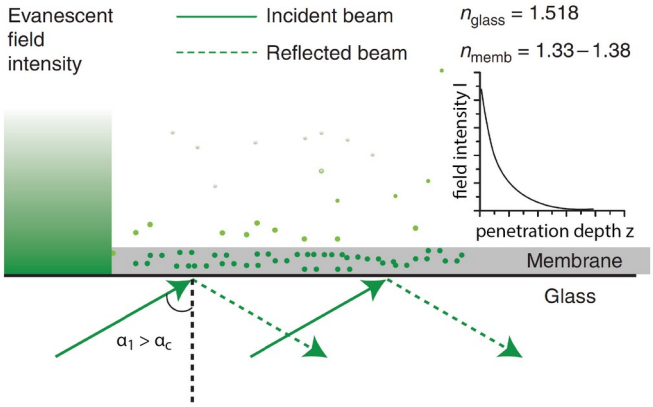

Figure 2.6: Principle of TIRF imaging
During TIRF imaging incidence beam is totally reflected at the glass-specimen interface if the incidence angle α_1 exceeds the critical angle α_c. The intensity I of the thereby generated evanescent wave declines exponentially with the penetration depth z. The thereby high z-axis resolution allows imaging of membrane-associated processes. Image from Sezgin and Schwille, 2011.

For TIRF experiments cells were imaged 24 h after transfection. During imaging, cells were perfused with extracellular solution (5.8 mM KCl, 144 mM NaCl, 0.9 mM MgCl, 1.3 mM CaCl, 0.7 mM NaH2PO4, 5.6 mM D-glucose, 10 mM HEPES, pH = 7.4).

Imaging for experiments shown in Figures 3.2A, B, E-G; 3.4G-I; 3.5A-C; 3.10A, B; 3.12A-D; 3.12H; 3.17A, C-E; 3.18; was performed on a BX51WI upright microscope (Olympus, Hamburg, Germany). GFP and CFP fluorescence was excited using 488 nm (Picarro, Sunnyvale, CA and Qioptiq, Göttingen, Germany) and 405 nm laser (Qioptiq, Göttingen, Germany), respectively. Laser light was directed through a TIRF condensor (Numerical Aperture: 1.45; Olympus) to the glass-specimen interface. Incidence angle was set manually, thus exact penetration depth could not be determined. Emission light passed a LUMPlanFI/IR 40×/0.8-numerical aperture water immersion objective (Olympus) and a CFP/YFP ET Dualband Filter (Chroma® Technology, Bellows Falls, US). Images were acquired with a TILL-Imago QE cooled CCD camera (TILL

Photonics GmbH, Gräfelfing, Germany) which was controlled by TILLvisION software (TILL Photonics GmbH).

For experiments shown in Figure 3.2A, C, D; 3.3; 3.4A-G; 3.5B, D; 3.6-3.9; 3.11; 3.12E-H, 3.13-3.16; 3.17B; 3.19-3.21 a Dmi8 upright microscope (Leica, Wetzlar, Germany) provided with an Infinity TIRF module (Leica) and diode lasers (Leica) were used. Excitation occurred at 488 nm (GFP), 561 nm (RFP) and 405 nm (CFP), respectively. Laser light was directed through a HC PL APO 100x/1.47 OIL objective (Leica) to the glas-specimen interface. For each specimen the critical reflection angle was determined by laser auto-alignment and nominal penetration depth was set to 90 nm. emission light passed GFP-T (505-555 nm), DS-Red-T (590-650 nm) or CFP-T (460-500 nm) emission filters (Leica) and was detected by a ORCA-Flash4.0 C13440-20C camera (Hamamatsu photonics, Hamamatsu, Japan). Image acquisition was controlled by LAS X software (Leica).

2.7 Plasma membrane protein cluster detection

Clustering of fluorescence-tagged proteins at the plasma membrane as recorded by TIRF microscopy was analyzed with ImageJ software. To determine regions of protein clustering (local fluorescence accumulation), individual images of TIRF time series (40 images) were background-subtracted followed by a procedure to also remove inhomogeneous local background usually encountered across each cell (Figure 2.7). To this end, images were median-filtered ($r = 0.9$ µm) and resulting blurry images were subsequently subtracted from the original (background-subtracted) images. Resulting images were thresholded using RenyiEntropy threshold, yielding regions above threshold as provisional pre-cluster area. Pixels assigned at least twice (out of 40 frames of a time series) to a pre-cluster were included to the final cluster ROI. Pixel detected only once as a pre-cluster were considered as background. Pixel with a distance of 1.8 µm (useful distance determined empirically) to the final cluster ROI were assigned to the non-cluster ROI (Figure 2.7). This algorithm was implemented as an ImageJ macro. In detected cluster and non-cluster ROIs fluorescence intensities were analyzed over time. For analysis of cluster size, number and area only baseline pre-clusters (10 images) were added to a baseline cluster ROI. Background cluster pixels were also deleted from this baseline cluster ROI.

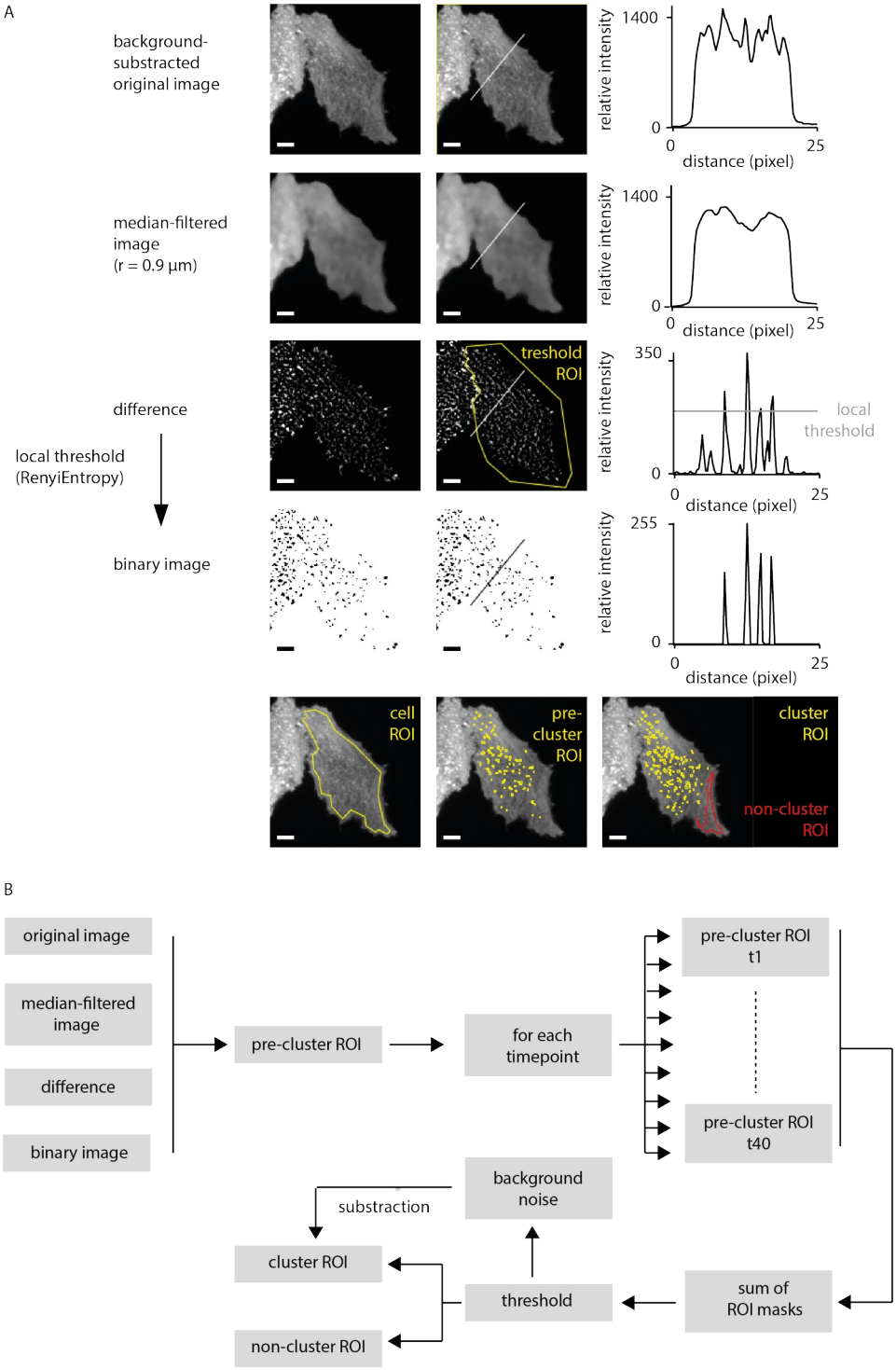

Figure 2.7: Principle of cluster detection algorithm
(**A**) Cluster detection exemplary shown for a GFP-tubbyCT-expressing CHO cell. Individual image processing steps are depicted from top to bottom. On the right line profiles along a distance of 25 pixel are depicted for each processing step. Original image (here timepoint 1) was background-subtracted and median-filtered. Resulting image was subsequently subtracted from original image and locally thresholded (RenyiEntropy). Pre-clusters were generated from resulting binary image. Final cluster and non-cluster ROIs were generated from pre-cluster ROIs of 40 timepoints of a time series. Scale bar = 5 µm. (**B**) Schematic representation of image processing.

This above described ImageJ macro was applied exactly in this way for TIRF images taken with the Leica setup (Dmi8 upright microscope, HC PL APO 100x/1.47 OIL objective). As images acquired with the BX51WI upright microscope (Olympus) and the LUMPlanFI/IR 40×/0.8-numerical aperture water immersion objective (Olympus) showed a lower imaging quality and thus a higher noise, a slight adjustment of the ImageJ macro was necessary: In these images, the cluster ROI was set more stringently and only pixels detected in at least 6 timepoints as pre-clusters were taken into account. Remaining pre-cluster pixels were considered as background noise. In all other respects, images from the Olympus and Leica setup were analyzed identically.

2.8 Chemicals

The M1R agonist oxotremorine-M (Oxo-M, Tocris Bioscience, Bristol, UK) was dissolved as a 10 mM stock solution in water and further diluted to 10 µM in extracellular solution (5.8 mM KCl, 144 mM NaCl, 0.9 mM MgCl, 1.3 mM CaCl, 0.7 mM NaH2PO4, 5.6 mM D-glucose, 10 mM HEPES, pH = 7.4).

100 mM stock solutions of PI4K inhibitor phenylarsine oxide (PAO, Sigma Aldrich, St Louis, US) were prepared in DMSO and diluted to a final working solution of 30 µM. The PI4K inhibitor GSK-A1 (Bojjireddy *et al.*, 2014) was dissolved as a 1 mM stock solution in DMSO and used for experiments in concentrations of 10 nM and 100 nM. PAO and GSK-A1 dilutions were made in extracellular solution.

The short-chain DAG analog DiC8 (Avanti Polar Lipids, Alabaster, USA) was prepared as a 20 mM stock in DMSO and diluted to a 20 µM working solution in extracellular solution.

2.9 Data analysis

TIRF data from the Olympus set-up were analyzed with TILLvisION software (TILL Photonics GmbH) and IGOR Pro (WaveMetrics, Lake Oswego, OR, USA). Analysis of TIRF data from the Leica set-up was done with ImageJ and IGOR Pro (WaveMetrics, Lake Oswego, OR, USA). Pearson's coefficients were calculated using ImageJ Coloc2 plug-in.

Fitting of FRET data and statistical analysis was done with IGOR Pro. For comparison of two groups, student's t tests were performed. Values derived from the same cells were analyzed using paired student's t tests. For comparisons of multiple groups to one

control group, Dunnett's tests were performed. Single sample t testing (H0 = 0) was done for co-localization analysis of Pearsons's coefficients. Asterisks indicate significance levels: *: $p < 0.05$, ***: $p < 0.01$. Respective p values are also stated in the figure legends.

3 Results

3.1 TubbyCT and PLCδ1-PH do not target mutually exclusive $PI(4,5)P_2$ pools

The $PI(4,5)P_2$ sensor tubbyCT has been described to be insensitive to $PI(4,5)P_2$ depletion via activation of PLCβ (Quinn, Behe and Tinker, 2008; Szentpetery *et al*., 2009). This had been ascribed to a high $PI(4,5)P_2$ affinity first (Quinn, Behe and Tinker, 2008; Szentpetery *et al*., 2009), but $PI(4,5)P_2$ titrations by use of a voltage-sensitive phosphatidylinositol 5-phosphatase (VSP) revealed a lower $PI(4,5)P_2$ affinity of tubbyCT than of PLCδ1-PH (Halaszovich, Schreiber and Oliver, 2009). PLCδ1-PH is a well-established $PI(4,5)P_2$ sensor which in contrast to tubbyCT shows a robust translocation into the cytosol following PLCβ activation (Stauffer, Ahn and Meyer, 1998; Szentpetery *et al*., 2009). Another possible explanation for the missing tubbyCT response is its localization to a PLCβ insensitive $PI(4,5)P_2$ pool. Therefore, I analyzed by Fluorescence Resonance Energy Transfer (FRET) experiments whether tubbyCT and PLCδ1-PH target different, mutually exclusive $PI(4,5)P_2$ pools and whether these pools are accessible by PLCβ.

CHO cells were transfected with CFP- and YFP-tagged $PI(4,5)P_2$ sensors as well as with the untagged muscarinic acetylcholine receptor M1 (M1R). CFP- and YFP-tagged sensors constituted the FRET donor and acceptor, respectively. In case of energy transfer, CFP excitation induces YFP emission, resulting in high FRET ratios. FRET ratios were calculated as YFP emission at CFP excitation normalized to CFP emission at CFP excitation. FRET ratio dynamics were determined during PLCβ signaling stimulated by application of the M1R agonist oxotremorine-M (Oxo-M; 10 µM). Because FRET ratios strongly depend on the distance between donor and acceptor fluorophores, $PI(4,5)P_2$ sensor translocations into the cytoplasm should decrease FRET ratios (Figure 3.1A). Additionally, FRET ratios rise with increasing acceptor-to-donor ratios. Thus, basal FRET ratios as well as FRET ratios following PLCβ activation were correlated to respective acceptor-to-donor ratios (Figure 3.1C, F, I). In my experiments, FRET ratios were saturated with acceptor-to-donor ratios above 15, thus those measurements were used for FRET ratio comparisons before and after PLCβ activation (Figure 3.1D, G, J).

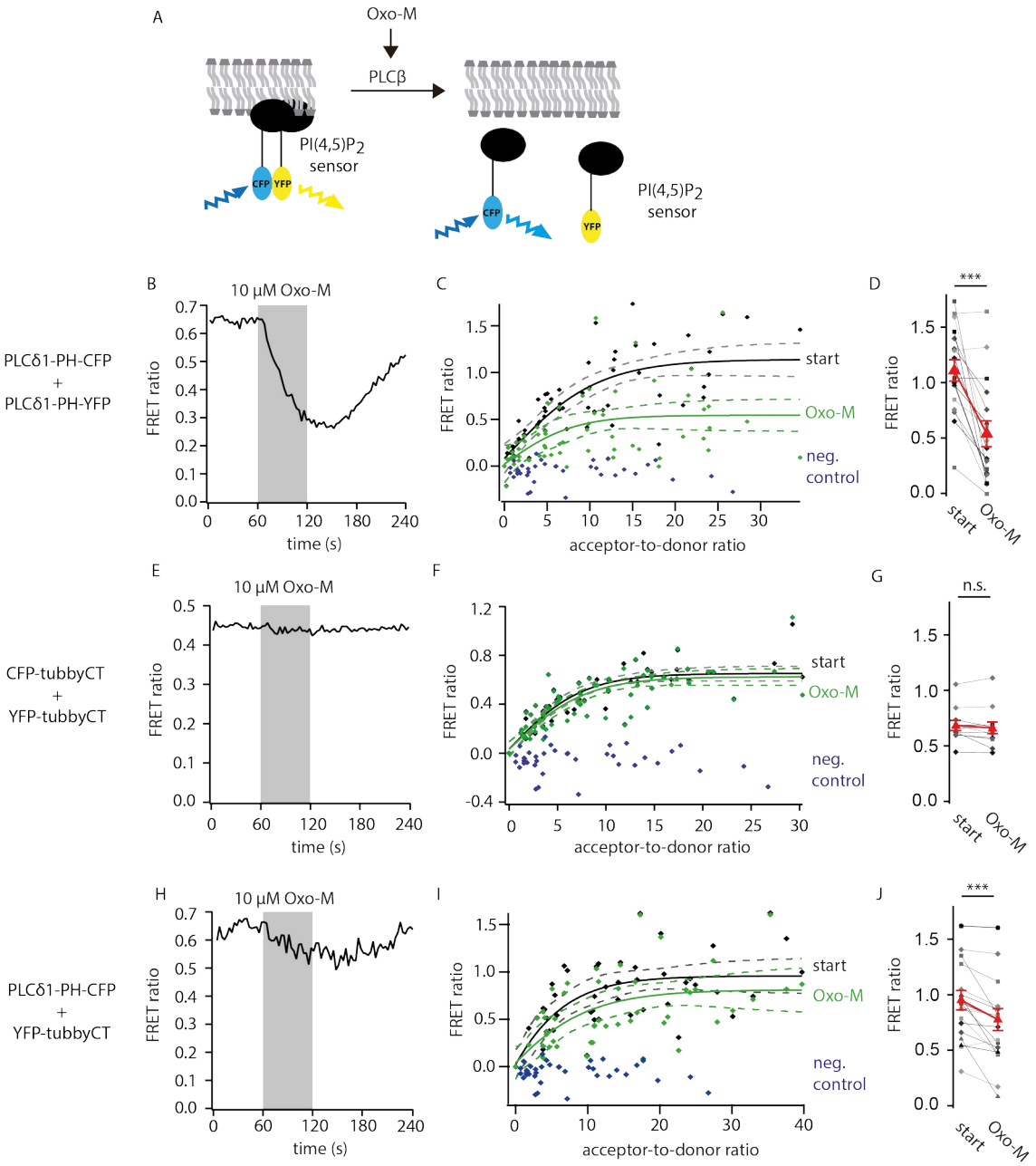

Figure 3.1: FRET between PI(4,5)P_2 sensors

(**A**) Experimental set-up. CFP- and YFP-tagged PI(4,5)P_2 sensors show high energy transfer if they localize to the same PM PI(4,5)P_2 pool. PLCβ-induced sensor translocation into the cytoplasm reduces FRET efficiencies. Dynamic FRET ratios between PLCδ1-PH-CFP and PLCδ1-PH-YFP (B-D), CFP-tubbyCT and YFP-tubbyCT (E-G) and PLCδ1-PH-CFP and YFP-tubbyCT (H-J) were determined. (**B, E, H**) FRET ratio dynamics of example cells upon PLCβ activation by 10 µM Oxo-M. (**C, F, I**) FRET ratios before (black) and during (t = 120 sec, green) Oxo-M application of individual cells blotted against their acceptor-to-donor ratios. FRET ratios between lyn11-CFP and free YFP under resting conditions represent the negative control (blue). Negative controls in C, F, I show the same n = 37 cells. (C) n = 60 cells. (F) n = 67 cells. (I) n = 56 cells. (**D, G, J**) FRET ratios before and during Oxo-M application of cells with an acceptor-to-donor ratio > 15. Mean and SEM is shown in red. (D) n = 17 cells; Paired students t test: p = 0.000110 (G) n = 12 cells; Paired students t test: p = 0.153 (J) n = 19 cells; Paired students t test: p = 0.000576.

First, FRET between CFP- and YFP-tagged PLCδ1-PH was measured. Under resting conditions FRET increased as a function of acceptor-to-donor ratio. Stimulation of PLCβ significantly reduced the FRET ratio, indicating translocation of the sensors into the cytoplasm (Figure 3.1B-D). FRET between membrane-localized lyn11-CFP (Inoue *et al.*, 2005) and cytosolic free YFP was used as negative control. These control FRET ratios ranged around zero and were independent of acceptor-to-donor ratio (Figure 3.1C, F, I).

Next, FRET between CFP- and YFP-tagged tubbyCT was determined. Similar to PLCδ1-PH experiments, cells displayed FRET under resting conditions with FRET ratios dependent on acceptor-to-donor ratio. However, FRET was independent of PLCβ activation (Figure 3.1E-G). These findings are in line with previously described PLCβ insensitivity of tubbyCT.

Interestingly, co-expression of PLCδ1-PH-CFP and YFP-tubbyCT also induced a robust, acceptor-to-donor ratio-dependent FRET signal (Figure 3.1H-J). Oxo-M application slightly, but significantly reduced FRET ratio as best seen in cells with a acceptor-to-donor ratio > 15 (Figure 3.1J).

Because FRET is only observed in case of close proximity of the donor and acceptor fluorophores, observed FRET under resting conditions clarifies that PLCδ1-PH and tubbyCT do not localize to mutually exclusive $PI(4,5)P_2$ pools. Hence, pools recognized by both domains are at least partially overlapping. However, these experiments do not exclude partial, or even preferential, association of each sensor domain to different $PI(4,5)P_2$ pools.

3.2 TubbyCT clusters at the PM and shows PLCβ-induced PM recruitment

Next, I reevaluated tubbyCT and PLCδ1-PH translocation dynamics following PLCβ-induced $PI(4,5)P_2$ depletion. CHO cells were transiently transfected with GFP-tagged tubbyCT and PLCδ1-PH, respectively and $PI(4,5)P_2$ sensor dynamics were imaged by Total Internal Reflection Fluorescence (TIRF) microscopy. In these experiments an increase of fluorescence intensity indicates association of the fluorescence-tagged protein domains to the membrane, whereas a decrease of fluorescence reports dissociation from the membrane into the cytoplasm. In this and in all subsequent experiments involving the activation of PLCβ, cells were additionally transfected with

untagged (non-fluorescent) M1R.

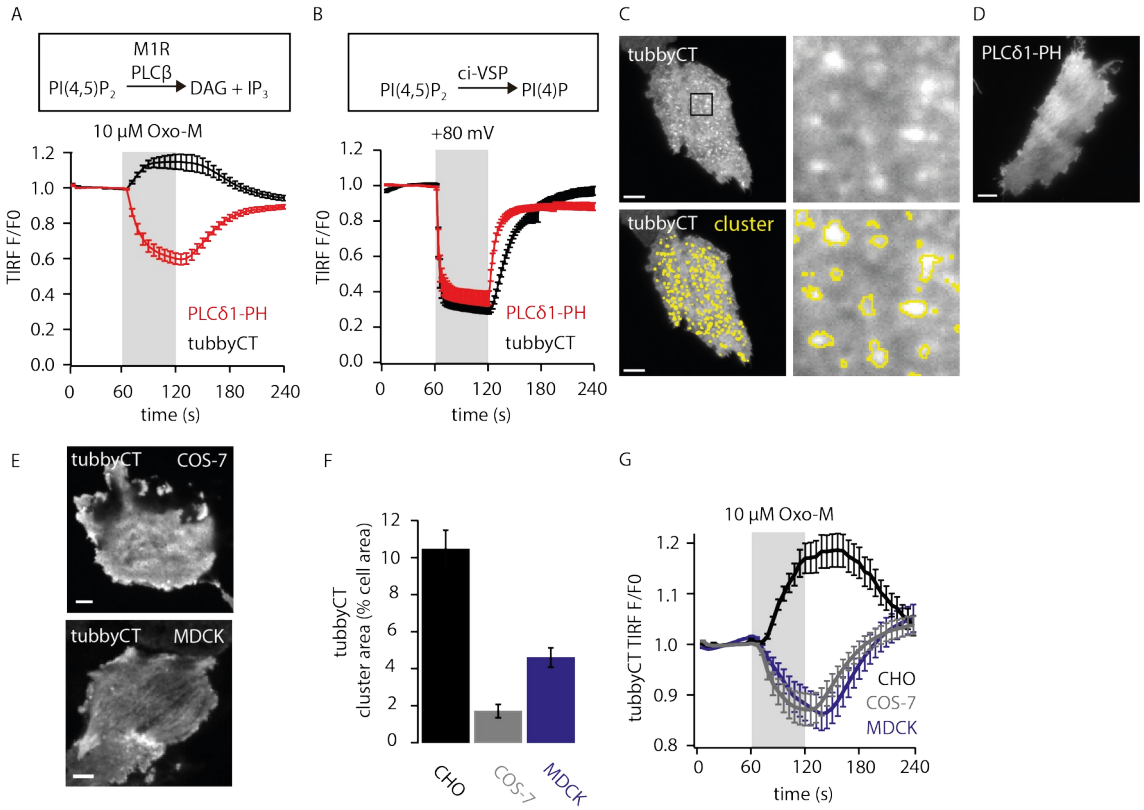

Figure 3.2: PI(4,5)P_2 sensor dynamics upon PI(4,5)P_2 depletion
(**A, B**) TIRF imaging of PLCδ1-PH-GFP (red) and GFP-tubbyCT (black) in CHO cells upon PI(4,5)P_2 depletion via activation of PLCβ (A) and ci-VSP (B). Mean ± SEM of normalized traces are plotted. (**A**) PLCδ1-PH: n = 34 cells; tubbyCT: n = 32 cells. (**B**) Measurements performed by Michael G. Leitner. PLCδ1-PH: n = 9 cells; tubbyCT: n = 7 cells. (**C, D**) Example TIRF images of CHO cells expressing GFP-tubbyCT (C) and PLCδ1-PH-GFP (D). Detected tubbyCT baseline clusters are framed in yellow. Scale bar = 5 µm, enlarged frame = 5µm. (**E**) Example TIRF images of GFP-tubbyCT-expressing COS-7 and MDCK cells. Scale bar = 5 µm. (**F**) TubbyCT cluster area in CHO, COS-7 and MDCK cells, quantified from images as in (C, E). Mean ± SEM are shown. n = 43 CHO cells; n = 28 COS-7 cells; n = 31 MDCK cells. (**G**) TubbyCT PM association upon PLCβ activation assessed by TIRF microscopy. Mean ± SEM of normalized traces are plotted. n = 67 CHO cells; n = 35 COS-7 cells; n = 97 MDCK cells.

Surprisingly, following PLCβ activation tubbyCT showed robust recruitment to the PM whereas in the same experimental setting PLCδ1-PH dissociated from the PM into the cytoplasm (Figure 3.2A). The results were compared to previous measurements by Michael G. Leitner, in which PI(4,5)P_2 depletion was achieved by activation of *Ciona intestinalis* VSP (ci-VSP). In these experiments CHO cells were transfected with the GFP-tagged sensors tubbyCT and PLCδ1-PH, respectively as well as with RFP-tagged ci-VSP. Depolarization of the PM to +80 mV known to induce strong activation of ci-VSP resulted in essentially full translocation of both sensors into the cytoplasm (Figure

3.2B). These control experiments confirm that also under our experimental conditions tubbyCT PM binding strongly depended on $PI(4,5)P_2$.

Interestingly, in CHO cells tubbyCT exhibited strong clustering within the PM which was not observed with PLCδ1-PH (Figure 3.2C, D). I analyzed tubbyCT clustering under resting conditions in terms of cluster number, size and area. For cluster detection I developed an ImageJ algorithm (see methods section). On average 0.66 ± 0.03 tubbyCT clusters were detected per μm^2 PM and clusters were 0.147 ± 0.010 μm^2 in size. Hence, tubbyCT cluster covered on average 10.5 ± 0.9% of the PM.

Next, I assessed tubbyCT clustering and PLCβ-induced dynamics in other cell types, COS-7 and MDCK cells.

In these cell types tubbyCT clustering was absent or at least much less pronounced (Figure 3.2E, F) and strikingly, also PM recruitment during PLCβ activation was not observed. In contrast, tubbyCT translocated into the cytoplasm following PLCβ-induced $PI(4,5)P_2$ depletion (Figure 3.2G). This finding prompted me to further investigate tubbyCT clustering and its relation to tubbyCT PM recruitment in CHO cells.

TubbyCT clusters might arise from local concentration of tubbyCT sensors within a plane PM, but their high fluorescence might also derive from PM invaginations. In the latter case, tubbyCT clusters would represent PM enrichment rather than protein accumulations within the PM. To elucidate the origin of tubbyCT clusters, I co-expressed GFP-tubbyCT and the PM marker lyn11-FRB-RFP in CHO cells. TIRF images and an example line profile depict that lyn11 was not enriched at tubbyCT clusters (Figure 3.3A), indicating that they do not derive from PM invaginations. Local $PI(4,5)P_2$ enrichment could drive tubbyCT clustering within the PM, hence I investigated whether the clusters are also detectable by other $PI(4,5)P_2$ sensors. I co-expressed RFP-tubbyCT with the GFP-tagged $PI(4,5)P_2$ sensors PLCδ1-PH and the Epsin1 ENTH domain, respectively. PLCδ1-PH labeled the PM largely homogeneously as expected. However, careful analysis of line profiles unveiled slight accumulation of PLCδ1-PH at tubbyCT clusters (Figure 3.3B). The Epsin1 ENTH domain exhibited strong accumulations at rod-like structures within the PM, as observed before (Leitner *et al*., 2019). Outside these clusters the PM was homogeneously labeled and no accumulation at tubbyCT clusters was detected (Figure 3.3C). Hence, the strong clustering is tubbyCT specific. However, the slight enrichment of PLCδ1-PH at

tubbyCT clusters additionally carefully hints at local PI(4,5)P_2 enrichment.

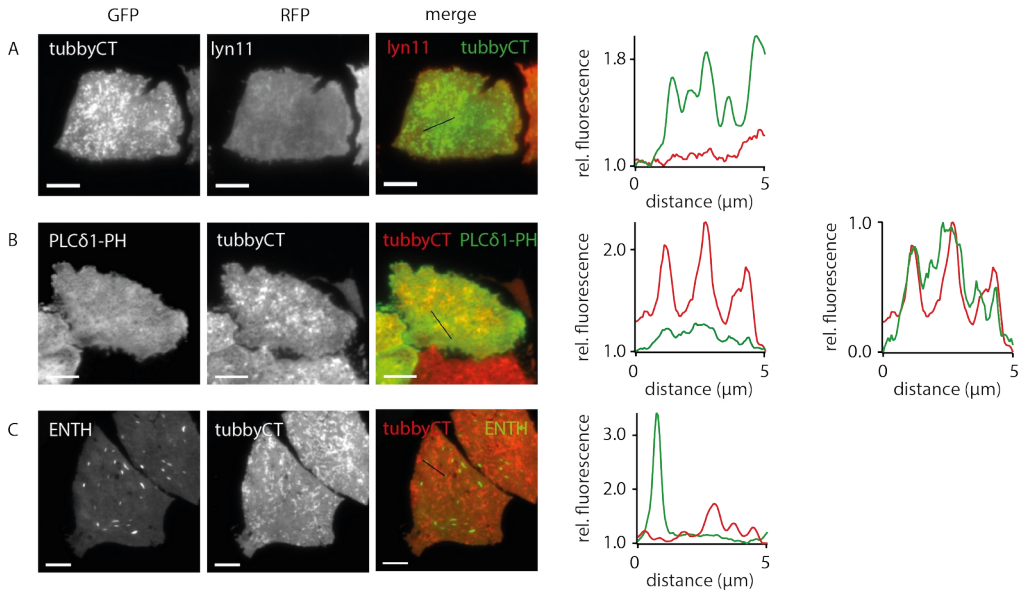

Figure 3.3: Co-localization of tubbyCT with the PM marker lyn11 and the PI(4,5)P_2 sensors PLCδ1-PH and Epsin1 ENTH
Example TIRF images of CHO cells co-expressing GFP-tubbyCT and RFP-lyn11 (**A**), PLCδ1-PH-GFP and RFP-tubbyCT (**B**) and ENTH-GFP and RFP-tubbyCT (**C**), respectively. Line profiles along a distance of 5 µm (highlighted in merged images) are shown on the right. Fluorescence intensities are normalized to the respective minimal value. The second representation of the line profile in (B) is normalized to minimal and maximal values and thereby emphasizes overlying peaks. In merged images and line profiles GFP-tagged proteins are displayed in green and RFP-tagged proteins in red. Scale bar = 5 µm.

3.3 TubbyCT recruitment occurs at regions with strong clustering

TubbyCT shows a strong clustering in CHO cells. However, the clusters were surrounded by regions of lower and largely homogeneous tubbyCT abundance (non-clustered regions). Hence, I studied tubbyCT dynamics following PLCβ activation in clustered and non-clustered regions independently. TIRF time series of tubbyCT-transfected CHO cells were analyzed by an ImageJ algorithm which automatically detected clustered and non-clustered regions and assigned respective ROIs for separate analysis of fluorescence time courses (see methods section; Figure 3.4A, B). Absolute tubbyCT fluorescence intensity changes at maximal PLCβ activation compared to baseline levels are depicted in Figure 3.4C. Strikingly, tubbyCT recruitment occurred at highly clustered regions but, in contrast, its dissociation from the membrane was only observed in non-clustered regions. Maximal increase was predominantly observed at detected clusters (Figure 3.4C). In contrast, in CHO cells transfected with PLCδ1-PH almost no clusters were detected and intensity decrease took place throughout the cell

(Figure 3.4D-F).

Next, I analyzed the time course of relative tubbyCT intensity at detected clusters and at non-clustered regions following PLCβ activation. This analysis clearly revealed that PM recruitment occurred at clusters whereas sensor translocation into the cytoplasm took place at the non-clustered PM regions (Figure 3.4G). This finding suggests that tubbyCT indeed senses PLCβ-induced $PI(4,5)P_2$ depletion that occurs in the non-clustered region. As this region only accounts for a minor portion of the PM in CHO cells and contains less tubbyCT, the tubbyCT dissociation dynamics was probably masked in analyses of overall PM (e.g. Figure 3.2A) by the dynamics of the clustered region.

Next, I studied cluster-dependent tubbyCT dynamics also in COS-7 and MDCK cells. In these cell types, tubbyCT cluster abundance was low compared to CHO cells (Figure 3.2E, F). Due to low intensity contrast in such uniformly labeled cells, the ImageJ algorithm detected a small amount of false positive clusters (see also PLCδ1-PH clusters in Figure 3.4E) which complicated the detection of cluster dynamics. Indeed, in COS-7 cells $1.7 \pm 0.4\%$ of the PM was covered with tubbyCT clusters and no differences between the tubbyCT dynamics in the clustered and non-clustered region could be resolved (Figure 3.4H). In MDCK cells tubbyCT clusters made up $4.6 \pm 0.5\%$ of the PM area. In the detected clusters tubbyCT translocated into the cytoplasm following PLCβ activation. However, this translocation was significantly less than in the non-clustered region (Figure 3.4I).

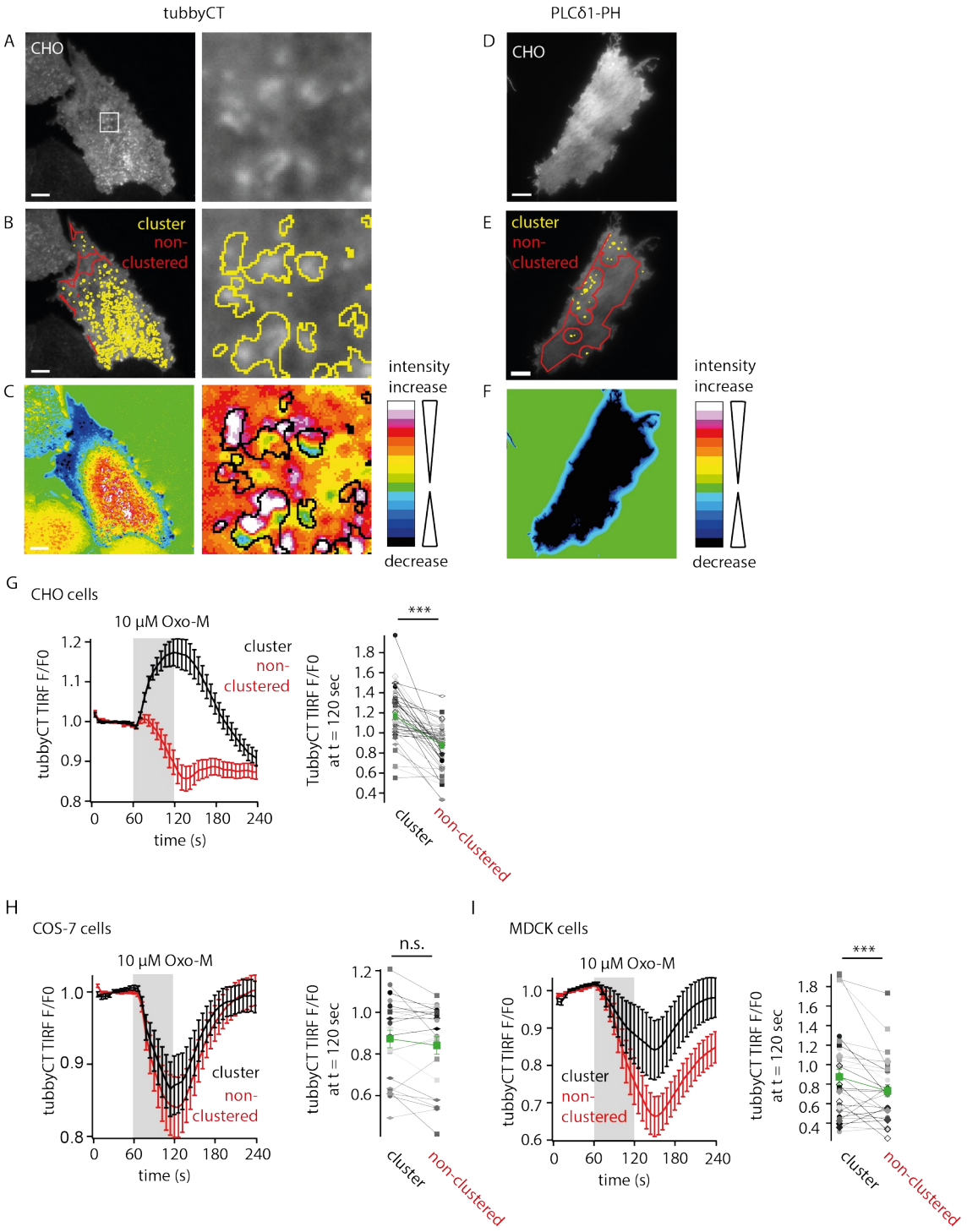

Figure 3.4: PLCβ-induced tubbyCT dynamics in clustered and non-clustered PM regions
(**A-C**) TIRF images of an example GFP-tubbyCT expressing CHO cell. Scale bar = 5 µm. Enlarged frame (right, side length = 5 µm) is shown in (A). Cluster (yellow) and non-clustered regions (red) are highlighted in (B). (C) Absolute fluorescence change upon 1 min 10 µM Oxo-M application. Clusters are framed in black. (**D-F**) TIRF images of an example PLCδ1-PH-GFP-expressing CHO cell. Scale bar = 5 µm. Clustered (yellow) and non-clustered (red) regions as well as absolute PLCβ-induced fluorescence change is shown in (B) and (C), respectively. (**G-I**) TIRF imaging of GFP-tubbyCT expressing CHO (G), COS-7 (H) and MDCK (I) cells. Relative time courses (mean ± SEM) of tubbyCT PM association in the clustered (black) and

non-clustered (red) region are shown on the left. Relative TIRF fluorescence at maximal Oxo-M application (t = 120 sec) in clustered and non-clustered regions of individual cells is depicted on the right. Mean ± SEM are shown in green. (G) n = 49 CHO cells. Paired students t test: p = 0.00000000044 (H) n = 24 COS-7 cells. Paired students t test: p = 0.094 (I) n = 30 MDCK cells. Paired students t test: p = 0.0054.

3.4 TubbyCT membrane recruitment is DAG-independent and PI(4,5)P_2-dependent

Contrary to expectations, PLCβ activation caused tubbyCT recruitment to its PM clusters. Since activation of PLCβ leads to DAG and I(1,4,5)P_3 production with DAG remaining membrane-bound (reviewed in Kadamur and Ross, 2013) a possible reason for the recruitment could be DAG binding. I investigated this hypothesis in the following experiment.

CHO cells were transiently transfected with GFP-tubbyCT and the DAG sensor PKCγ-C1-GFP, respectively. 20μM 1,2-Dioctanoyl-*sn*-glycerol (DiC8), a short-chain DAG analog was applied while cells were imaged by TIRF microscopy. After an initial fluorescence decrease PKCγ-C1 was robustly recruited to the PM, indicating DiC8 incorporation into the inner leaflet of the PM (Figure 3.5A). An initial transient drop in PKCγ-C1 fluorescence in this type of experiment was observed before (Wilke *et al.*, 2014) and may be explained by incorporation of DiC8 into the upper, non-imaged region of the PM preceding accumulation in the membrane imaged by TIRF. Importantly, tubbyCT showed no PM recruitment following DiC8 application, indicating that it does not bind to DAG (Figure 3.5A).

In contrast, PI(4,5)P_2 binding of tubbyCT is undisputed and a binding pocket has been identified in its crystal structure (Santagata *et al*., 2001). Several tubbyCT binding pocket mutants with reduced PI(4,5)P_2 affinity were previously described. TubbyCT R332H mutation for example decreases PI(4,5)P_2 affinity, but this mutant still holds intermediate membrane binding capability (Santagata *et al*., 2001; Halaszovich, Schreiber and Oliver, 2009). Furthermore, in the tubbyCT KR330/332AA mutant PI(4,5)P_2 binding is severely disrupted and PM binding has been reported to be lost completely (Santagata *et al*., 2001). In order to examine the role of PI(4,5)P_2 binding in the newly discovered PLC-dependent recruitment of tubbyCT to the PM, I studied the dynamics of PI(4,5)P_2 binding mutants upon PLCβ activation. CHO cells were transiently transfected with GFP-tagged tubbyCT wildtype (WT), R332H mutant and KR330/332AA mutant, respectively. PLCβ was activated by application of 10 μM

Oxo-M and membrane association of the sensors was imaged by TIRF microscopy. As a further control, tubbyCT Y343F mutant was imaged. Y343 is located within the PI(4,5)P_2 binding pocket, but its mutation to phenylalanine should not affect PI(4,5)P_2 binding (Santagata *et al.*, 2001). TubbyCT WT as well as the Y343F mutant showed robust membrane recruitment, which was not observed in the R332H and KR330/332AA mutants. In contrast, reduced PI(4,5)P_2 affinity lead to the dissociation of the sensors into the cytoplasm (Figure 3.5B). Translocation of tubbyCT KR330/332AA was weak, but detectable. This is in line with its very weak resting PM binding and suggests that minimal but detectable PI(4,5)P_2 binding capability remains also in this mutant.

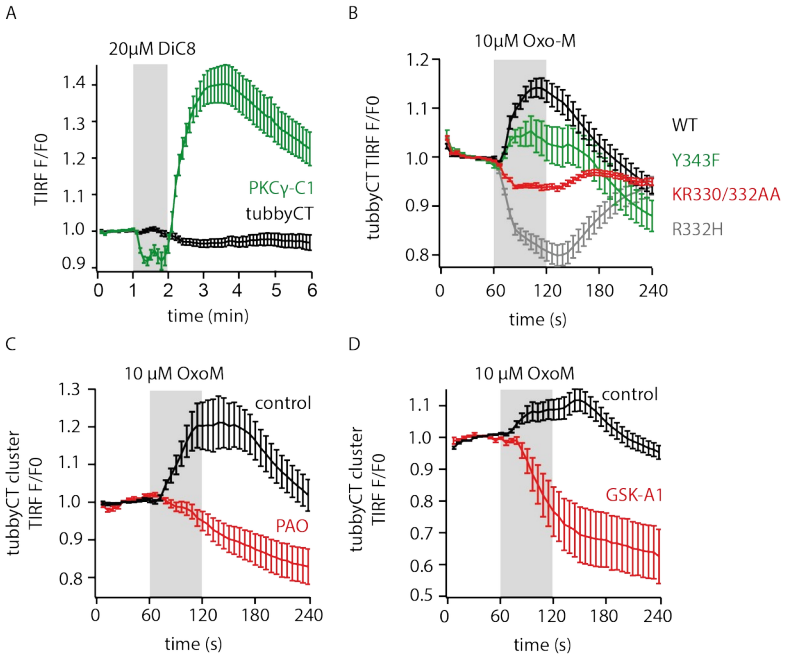

Figure 3.5: Probing DAG and PI(4,5)P_2 dependence of tubbyCT PM recruitment
(**A**) TIRF imaging of CHO cells expressing PKCγ-C1-GFP (green) and GFP-tubbyCT (black), respectively. Normalized PM flourescence (mean ± SEM) upon DiC8 application is shown. PKCγ-C1: n = 29 cells. tubbyCT: n = 17 cells. (**B**) TIRF imaging of CHO cells expressing GFP-tubbyCT wild-type (WT, black), Y343F (green), KR330/332AA (red) and R332H (grey) mutants, respectively. Mean ± SEM of normalized PM fluorescence upon PLCβ activation is plotted. WT: n = 61 cells. Y343F: n = 27 cells. KR330/332AA: n = 58 cells. R332H: n = 40 cells. (**C, D**) TIRF imaging of GFP-tubbyCT expressing CHO cells. PLCβ was activated following incubation of cells in PI4K inhibitors PAO (30 µM) (C) and GSK-A1 (100 nM) (D), respectively. Respective control cells were incubated in extracellular solution. Relative cluster fluorescence (mean ± SEM) is plotted. (**C**) control: n = 40 cells; PAO: n = 24 cells. (**D**) control: n = 39 cells; 100 nM GSK-A1: n = 25 cells.

These findings indicated that PLCβ-induced tubbyCT membrane recruitment is indeed dependent on PI(4,5)P_2 binding. Although it is generally thought that activation of PLCβ leads to net PI(4,5)P_2 consumption, recruitment therefore can only be explained by net PI(4,5)P_2 increase due to its prompt (stimulated) resynthesis. PI(4,5)P_2 is generated from its precursor PI in a two-step phosphorylation process by PI4Ks and PIP5Ks. To elucidate the influence of PI(4,5)P_2 resynthesis on tubbyCT cluster recruitment during PLCβ activation, I inhibited PI4Ks with 30 µM phenylarsine oxide (PAO; Figure 3.5C) and 100 nM GSK-A1 (Bojjireddi *et al*., 2014) (Figure 3.5D), respectively. CHO cells were transfected with GFP-tubbyCT and incubated with PI4K inhibitors prior to TIRF imaging. Control cells were incubated in extracellular solution. During imaging PLCβ was activated and cluster dynamics were measured. Figure 3.5C, D depict that inhibition of PI4Ks abolished recruitment of tubbyCT into the clusters. In contrast, PLCβ activation induced tubbyCT translocation into the cytoplasm, whereas control cells showed cluster recruitment as expected. Moreover, with PI4K inhibitors, tubbyCT membrane association did not recover confirming successful PI4K inhibition.

3.5 TubbyCT localizes to E-Syt3-rich ER-PM junctions

3.5.1 TubbyCT co-localizes with the ER-PM junction protein E-Syt3

The dependence of PLCβ-induced tubbyCT recruitment on PI(4,5)P_2 synthesis together with its occurrence at confined puncta brought me to the hypothesis that tubbyCT clusters may correspond to the subtype of ER-PM junctions which is involved in PI transfer and hence in PI(4,5)P_2 resynthesis. These ER-PM contact sites are tethered by E-Syts, preformed under resting condition and tightened upon intracellular Ca^{2+} rise, i.e. during PLCβ activation. Tightened junctions as well as accumulation of DAG and PA at the PM then trigger the transfer of PI, the precursor of PI(4,5)P_2, from the ER to the PM. It is mainly mediated by the PI transfer proteins Nir2 and Nir3. Once in the PM, PI is step-wise phosphorylated to form PI(4,5)P_2 (reviewed in Pemberton, Kim and Balla, 2020).

I tested the hypothesis by examining co-localization of GFP-tubbyCT with the RFP-tagged ER-PM junction proteins E-Syt1-3 and Nir2/3, respectively. These co-localization experiments (Figure 3.6) as well as co-localization experiments building on them (Figure 3.7-3.9) were performed by myself and by Lea Schultz, a student assistant

who performed experiments conceived and supervised by myself. The exact origin of the data shown in Figure 3.6-3.9 is annotated in the respective figure legends.

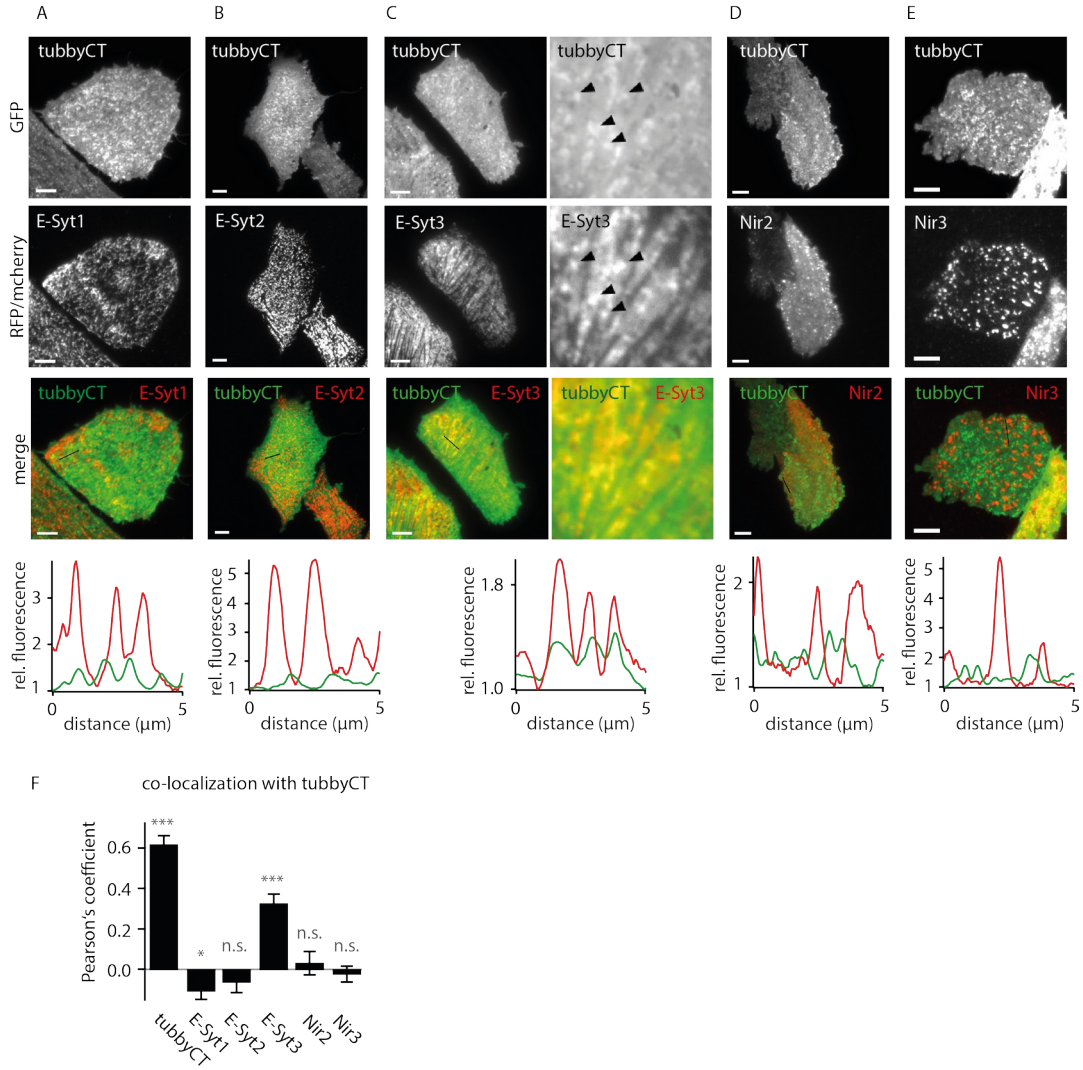

Figure 3.6: Co-localization of tubbyCT with ER-PM junction proteins
(**A-E**) Example TIRF images of CHO cells co-expressing GFP-tubbyCT and RFP-E-Syt1 (A), RFP-E-Syt2 (B), RFP-E-Syt3 (C) Nir2-mcherry (D) and Nir3-mcherry (E), respectively. Scale bar = 5 µm. Size length of enlarged frame in (C) = 5 µm. Black arrows point at overlying clusters. In the first line GFP images are shown, followed by RFP/mcherry and merged images. Line profiles along a distance of 5 µm are depicted below. RFP/mcherry and GFP fluorescences are normalized to the respective minimal values. In merged images and line profiles tubbyCT is plotted in green and RFP/mcherry-tagged proteins in red. Example images (A, C) were taken by Veronika Thallmair (VT), example images (B, D, E) by Lea Schultz (LS). (**F**) Pearson's coefficients (mean ± SEM) from cells as in (A-E) and from cells co-expressing GFP-tubbyCT and RFP-tubbyCT. tubbyCT + tubbyCT: n = 13 cells (VT) + n = 10 cells (LS); E-Syt1 + tubbyCT: n = 2 cells (VT) + n = 14 cells (LS); E-Syt2 + tubbyCT: n = 5 cells (VT) + n = 13 cells (LS); E-Syt3 + tubbyCT: n = 17 cells (VT) + n = 9 cells (LS); Nir2 + tubbyCT: n = 6 cells (VT) + n = 18 cells (LS); Nir3 + tubbyCT: n = 7 cells (VT) + n = 17 cells (LS). Results of two-tailed single sample students t tests (H0 = 0) are annotated in grey (n.s. = not significant; *: $p < 0.05$; ***: $p < 0.01$).

CHO cells were co-transfected with GFP- and RFP/mcherry-tagged constructs and imaged by TIRF microscopy. Co-localization under resting conditions was subsequently examined by line profile analysis and calculation of Pearson's coefficients r. The Pearson's coefficient correlates pixel intensities of two corresponding images and ranges between r = -1 (perfect exclusion) to r = +1 (perfect co-localization). A Pearson's coefficient of r = 0 indicates lack of correlation.

E-Syt1 and Nir2 showed a weak ER-PM junction localization under resting conditions (Figure 3.6A, D) which is in line with its predominant localization to activated ER-PM contact sites (Chang *et al*., 2013; Giordano *et al*., 2013; Fernández-Busnadiego *et al*., 2015). Importantly, also in my experiments activation of PLCβ induced recruitment of both proteins into the prelabeled regions, confirming the detection of the right structures. E-Syt2, E-Syt3 and Nir3 localized robustly to ER-PM junctions (Figure 3.6B, C, E) also under resting conditions. TubbyCT clusters did not co-localize with E-Syt1-, E-Syt2-, Nir2- and Nir3-labeled ER-PM junctions which can be best seen in missing peak overlays in respective example line profiles and Pearson's coefficients around zero (Figure 3.6A, B, D-F). In contrast, E-Syt3 clearly co-localized with tubbyCT clusters as can be seen from overlying clusters in enlarged frames. Also the depicted line profile displays overlying peaks of GFP and RFP traces (Figure 3.6C) and the respective Pearson's coefficient reached a value of $r = 0.325 \pm 0.046$ which was significantly different from zero. However, it was also significantly lower than the positive control GFP-tubbyCT with RFP-tubbyCT ($r = 0.616 \pm 0.045$; Figure 3.6F).

For comparison, I also examined co-localization between PLCδ1-PH-GFP and the ER-PM junction proteins RFP-E-Syt1-3 and Nir2/3-mcherry. PLCδ1-PH labeled the PM homogeneously (see above, Figure 3.2D, 3.3B) and did not substantially co-localize with the tested ER-PM junction proteins (Figure 3.7A-F). Pearson's coefficients obtained from co-localization of PLCδ1-PH with E-Syt1 and E-Syt3 were not significantly different from zero. However, PLCδ1-PH slightly co-localized with E-Syt2, Nir2 and Nir3, but respective Pearsons's coefficients were smaller than the value obtained from co-localization of tubbyCT with E-Syt3 (Figure 3.7F).

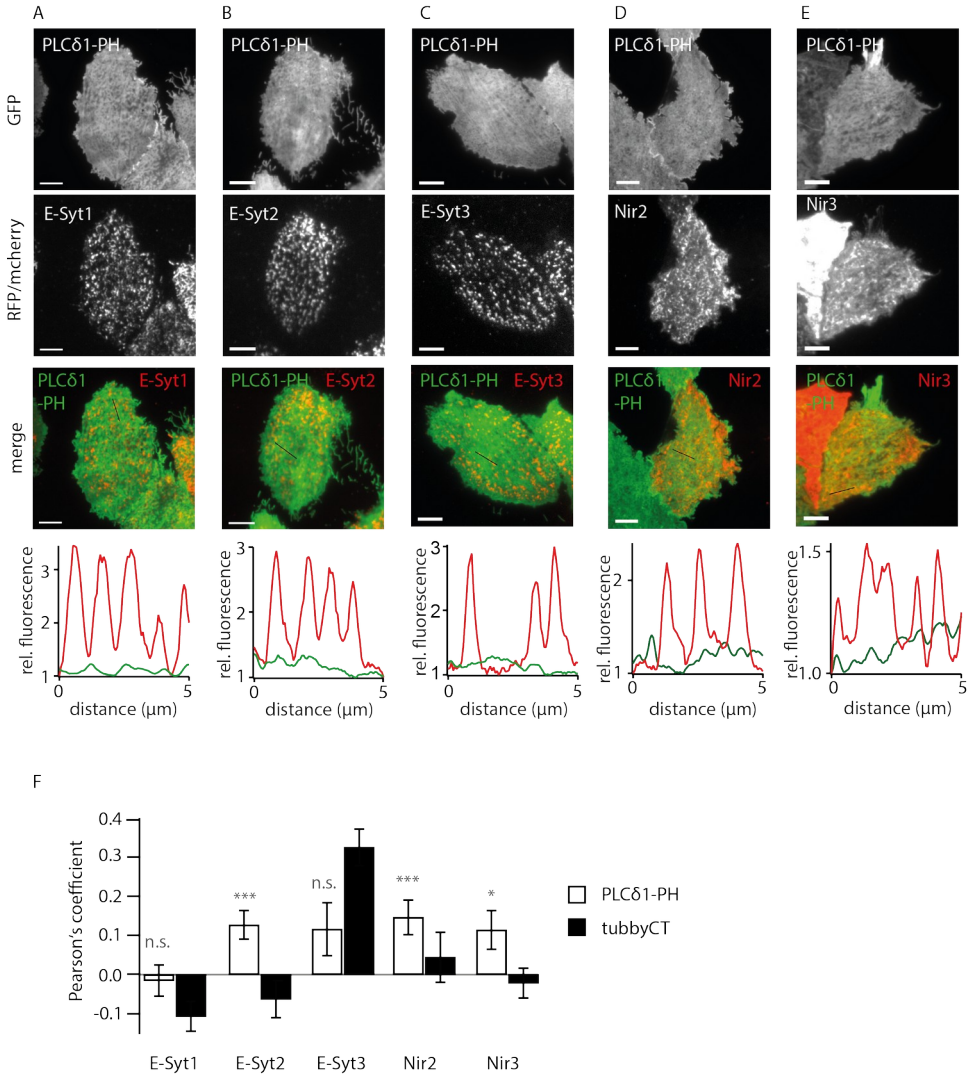

Figure 3.7: Co-localization of PLCδ1-PH with ER-PM junction proteins
(**A-E**) Example TIRF images of CHO cells co-expressing PLCδ1-PH-GFP and RFP-E-Syt1 (A), RFP-E-Syt2 (B), RFP-E-Syt3 (C) Nir2-mcherry (D) and Nir3-mcherry (E), respectively. Scale bar = 5 µm. In the first line GFP images are shown, followed by RFP/mcherry and merged images. Line profiles along a distance of 5 µm are depicted below. RFP/mcherry and GFP fluorescences are normalized to respective minimal values. In merged images and line profiles PLCδ1-PH is plotted in green and RFP/mcherry-tagged proteins in red. Example images (B-E) were taken by Veronika Thallmair (VT), example images (A) by Lea Schultz (LS). (**F**) Pearson's coefficients r (mean ± SEM) from cells as in (A-E) (white) and from cells co-expressing GFP-tubbyCT and respective ER-PM junction proteins (black). Black bars are replotted from Figure 3.6F. E-Syt1 + PLCδ1-PH: n = 4 cells (VT) + n = 16 cells (LS); E-Syt2 + PLCδ1-PH: n = 9 cells (VT) + n = 10 cells (LS); E-Syt3 + PLCδ1-PH: n = 12 cells (VT) + n = 8 cells (LS); Nir2 + PLCδ1-PH: n = 2 cells (VT) + n = 14 cells (LS); Nir3 + PLCδ1-PH: n = 5 cells (VT) + n = 13 cells (LS). Results of two-tailed single sample students t tests (H0 = 0) are annotated in grey (n.s. = not significant; *: $p < 0.05$; ***: $p < 0.01$).

3.5.2 TubbyCT is recruited to ER-PM junctions via interaction with E-Syt3

TubbyCT clearly co-localized with the ER-PM tethering protein E-Syt3, but not with E-Syt1/2 and Nir2/3. At first glance, this specific co-localization appeared puzzling as E-Syts are described to homo- and heterodimerize (Tremblay *et al.*, 2015) and also to co-localize with Nir2/3 (Chang *et al.*, 2013; Chang and Liou, 2015).

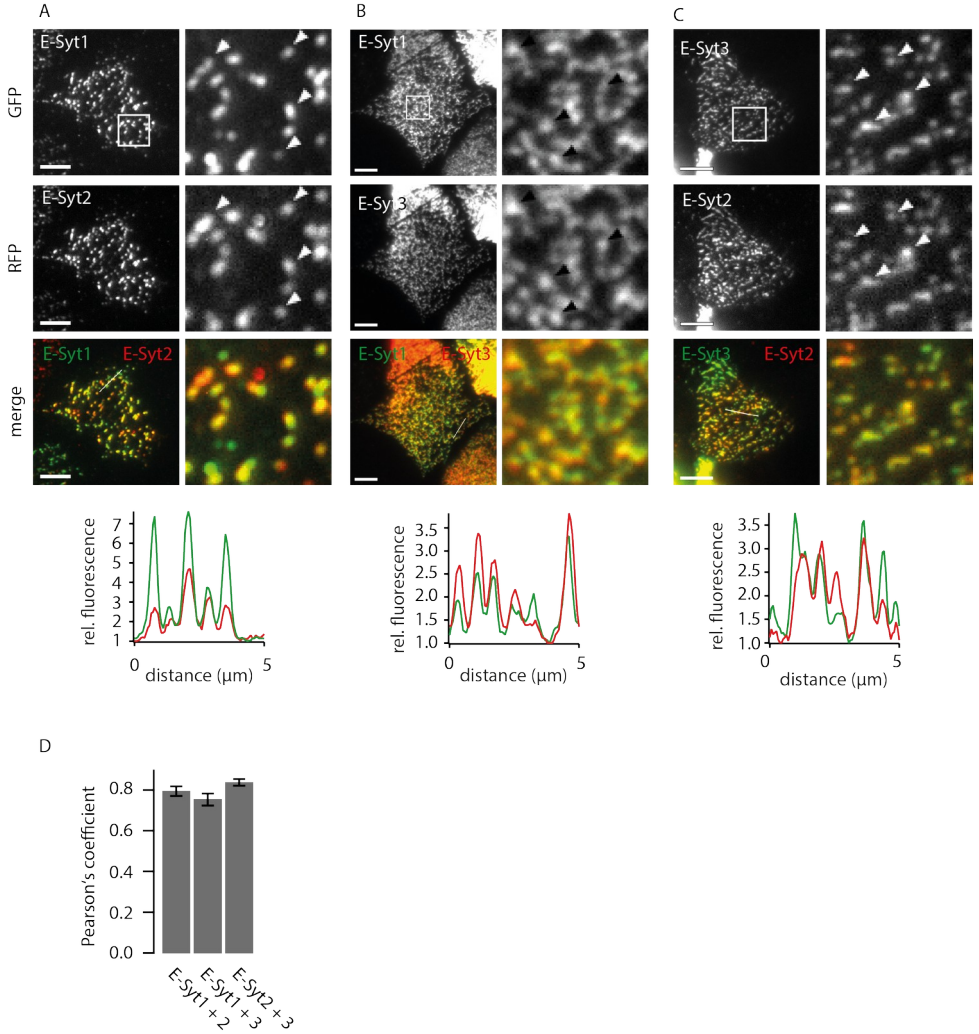

Figure 3.8: Co-localization of E-Syts with each other
(**A-C**) Example TIRF images of CHO cells co-expressing GFP-E-Syt1 and RFP-E-Syt2 (A), GFP-E-Syt1 and RFP-E-Syt3 (B) and GFP-E-Syt3 and RFP-E-Syt2 (C), respectively. Scale bar = 5 µm. Side length of enlarged frames = 5 µm. Arrows point at overlying clusters. In the first line GFP images are shown, followed by RFP and merged images. Line profiles along a distance of 5 µm are depicted below merged images. RFP and GFP fluorescence is normalized to respective minimal values. In merged images and line profiles GFP-tagged proteins are plotted in green and RFP-tagged proteins in red. Example images (A-C) were taken by Veronika Thallmair (VT). (**D**) Pearson's coefficients (mean ± SEM) from cells as in (A-C). E-Syt1 + E-Syt2: n = 17 cells (VT) + n = 17 cells (Lea Schultz; LS); E-Syt1 + E-Syt3: n = 14 cells (VT) + n = 9 cells (LS); E-Syt2 + E-Syt3: n = 13 cells (VT) + n = 13 cells (LS).

Hence, I reevaluated the co-localization of RFP- and GFP-tagged E-Syts with each other in CHO cells under resting conditions.

All three E-Syts clearly co-localized with each other as can be seen from overlying clusters in enlarged frames as well as from overlying peaks in depicted line profiles (Figure 3.8A-C). Pearson's coefficients were significantly different from zero and ranged around r = 0.8 (Figure 3.8D).

Although co-expressed E-Syts localized to the same ER-PM contact sites, only E-Syt3 co-localized with tubbyCT, when expressed individually. Hence, I wondered whether tubbyCT may be recruited to ER-PM junctions by interaction with E-Syt3 and whether E-Syt3 over-expression can evoke co-localization of tubbyCT also with other ER-PM junction proteins. In CHO cells, I co-expressed GFP-tubbyCT, CFP-E-Syt3 and RFP-E-Syt1, RFP-E-Syt2, Nir2-mcherry and Nir3-mcherry, respectively. Using TIRF microscopy, I subsequently analyzed co-localization of GFP-tubbyCT with RFP/mcherry-tagged ER-PM junction proteins in presence of CFP-E-Syt3. Over-expression of E-Syt3 elicited robust co-localization of E-Syt1 and E-Syt2 with tubbyCT as can be seen from overlying clusters in enlarged frames and line profiles (Figure 3.9A, B). Also Pearson's coefficient values were significantly increased with respect to the absence of E-Syt3 over-expression (Figure 3.9E). Pearson's coefficients did not differ from those obtained from co-localization of tubbyCT with E-Syt3. E-Syt3 over-expression also increased co-localization of tubbyCT with Nir2 and Nir3, respectively, albeit co-localization was not as robustly observed as in case of E-Syt1/2 (Figure 3.9C-E). These experiments indeed suggest that tubbyCT is recruited to ER-PM junctions by direct or indirect interaction with E-Syt3.

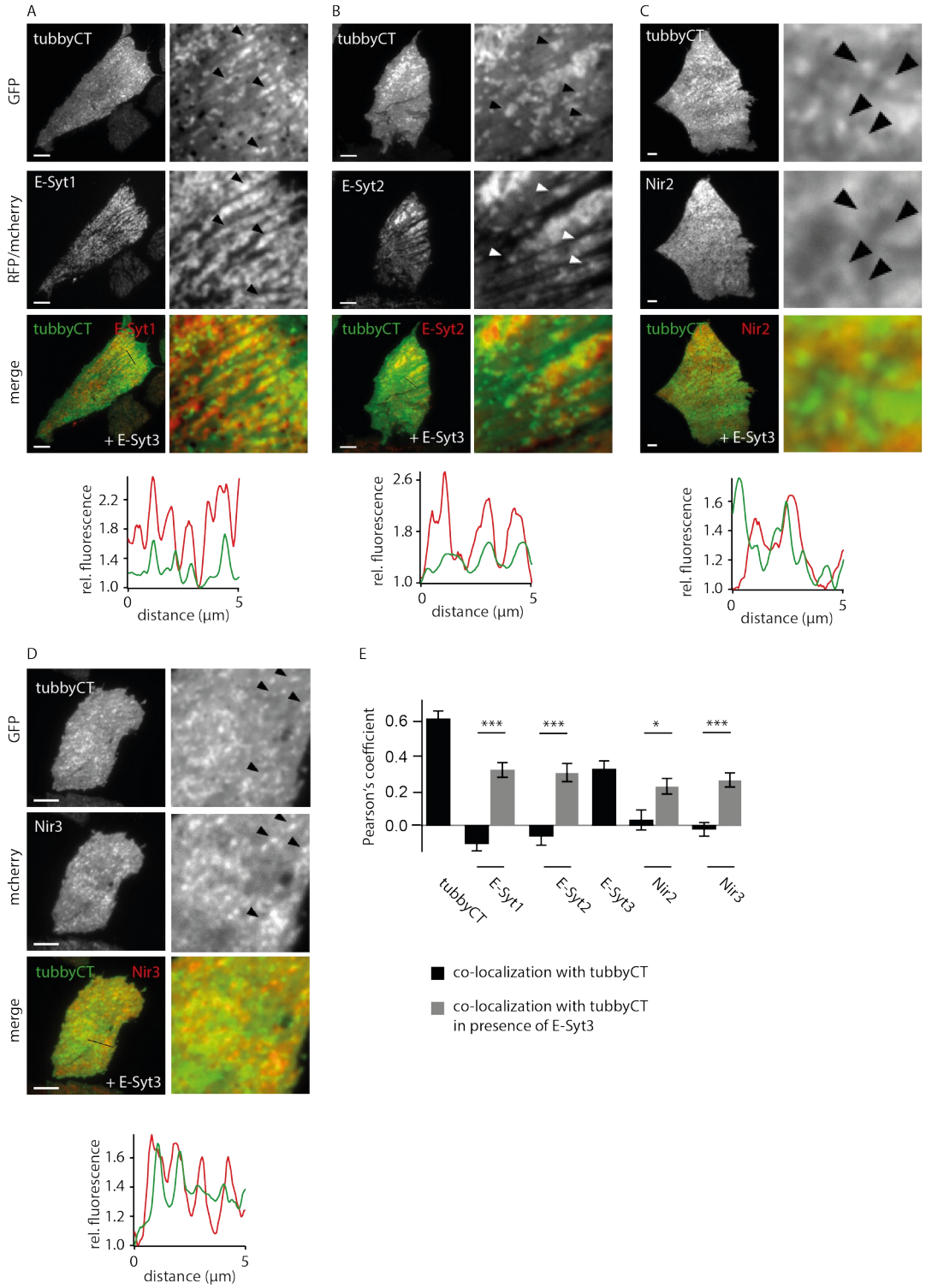

Figure 3.9: Co-localization of tubbyCT with ER-PM junction proteins in presence of E-Syt3

(**A-D**) Example TIRF images of CHO cells co-expressing GFP-tubbyCT, CFP-E-Syt3 and RFP-E-Syt1 (A), RFP-E-Syt2 (B), Nir2-mcherry (C) and Nir3-mcherry (D), respectively. In the first line GFP images are shown, followed by RFP/mcherry and merged images. Scale bar = 5 µm. Side length of enlarged frames = 5 µm. Arrows point at overlying clusters. Line profiles along a distance of 5 µm are depicted below merged images. RFP/mcherry and GFP fluorescences are normalized to respective minimal values. In merged images and line profiles GFP-tagged

proteins are plotted in green and RFP/mcherry-tagged proteins in red. Example images (A-D) were taken by Veronika Thallmair (VT). (**E**) Pearson's coefficients (mean ± SEM) from cells as in (A-D) (green) and from cells co-expressing GFP-tubbyCT and respective RFP/mcherry-tagged ER-PM junction proteins as well as RFP-tubbyCT (black). These co-localizations (black) were already shown in Figure 3.6F. E-Syt1 + tubbyCT in presence of CFP-E-Syt3: n = 9 cells (VT) + n = 16 cells (Lea Schultz; LS). Students t test: p = 0.0000000068; E-Syt2 + tubbyCT in presence of CFP-E-Syt3: n = 8 cells (VT) + n = 13 cells (LS). Students t test: p = 0.0000086; Nir2 + tubbyCT in presence of CFP-E-Syt3: n = 15 cells (VT) + n = 12 cells (LS). Students t test: p = 0.011; Nir3 + tubbyCT in presence of CFP-E-Syt3: n = 7 cells (VT) + n = 11 cells (LS). Students t test: p = 0.000054.

Thus, I wondered whether over-expression of E-Syt3 increases tubbyCT cluster formation in CHO cells and whether it can evoke cluster formation in COS-7 cells, a cell type were almost no tubbyCT clusters were observed (Figure 3.2E, F). To this end, GFP-tubbyCT was co-expressed with either RFP-E-Syt3 or free RFP (control). TubbyCT was imaged by TIRF microscopy and cluster area was analyzed.

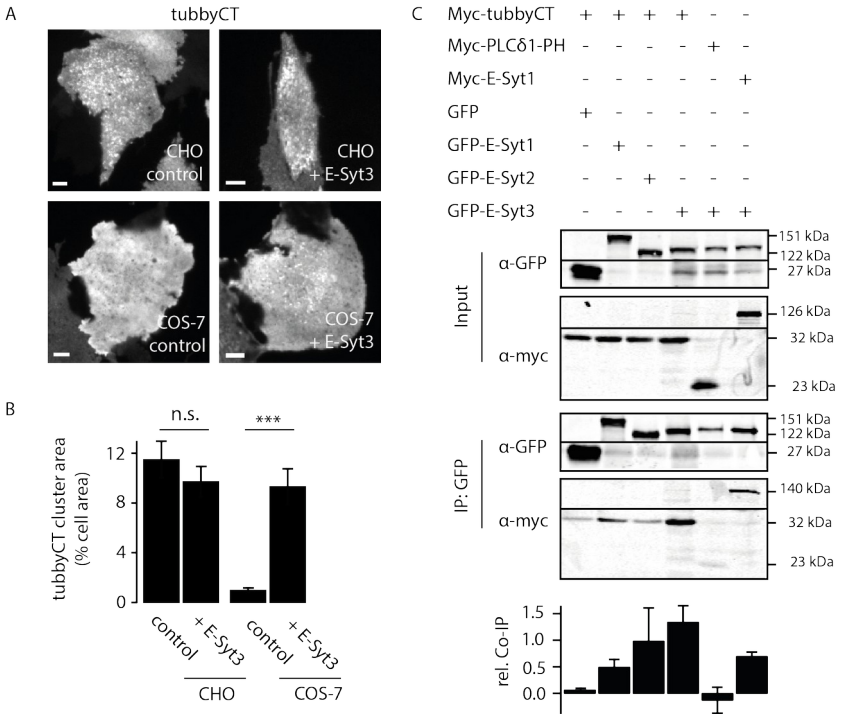

Figure 3.10: Probing tubbyCT-E-Syt3 interaction
(**A**) Example TIRF images of GFP-tubbyCT-expressing CHO and COS-7 cells. Cells additionally co-expressed free RFP (control) and RFP-E-Syt3, respectively. Scale bar = 5 µm. (**B**) TubbyCT cluster area from cells shown exemplary in (A). CHO cells: control: n = 53 cells; + RFP-E-Syt3: n =46 cells; Students t test: p = 0.189). COS-7 cells: control: n = 21 cells; + RFP-E-Syt3: n =21 cells; Students t test: p = 0.0000119). (**C**) Co-IP of myc-tubbyCT and myc-PLCδ1-PH with GFP-tagged E-Syts. CHO cells were transfected with myc- and GFP-tagged constructs as indicated. Cell lysates (input) were used for immunoprecipitation with αGFP-coated beads. Proteins were detected by Western Blotting. Quantification of co-immunoprecipitated protein amount relative to immunoprecipitated protein amount is shown below.

In CHO cells over-expression of E-Syt3 did not increase tubbyCT cluster area further, as no difference to control cells (with RFP) was observed (Figure 3.10A, B). In COS-7 cells, in contrast, E-Syt3 over-expression evoked massive tubbyCT cluster formation. Clusters covered 9.3 ± 1.5% of the cell area, which significantly exceeded clustered area of control cells (1.0 ± 0.2%; Figure 3.10A, B).

Taken together, these data suggested a protein-protein interaction between tubbyCT and E-Syt3.

This possibility was addressed by co-immunoprecipitation experiments. In CHO cells myc-tubbyCT was co-expressed with free GFP and GFP-tagged E-Syt1-3, respectively. Cell lysates were used for immunoprecipitation with αGFP beads. Immunoprecipitated and co-immunoprecipitated proteins were subsequently analyzed by western blotting. Additionally, interaction of myc-PLCδ1-PH with GFP-E-Syt3 was studied. As positive control, GFP-E-Syt1 and myc-E-Syt3 were used, as they are known to heterodimerize (Tremblay *et al*., 2015).

Myc-E-Syt1 as well as myc-tubbyCT co-immunoprecipitated with GFP-E-Syt3 in each of the individual four experiments. In contrast, myc-PLCδ1-PH did not co-immunoprecipitate with GFP-E-Syt3. Moreover, myc-tubbyCT co-immunoprecipitated with GFP-E-Syt1 and GFP-E-Syt2 in some of the individual experiments (Figure 3.10C). These findings thus show that tubbyCT and E-Syt3 interact directly or indirectly.

3.5.3 Mapping the molecular interaction interface between tubbyCT and E-Syt3

To further characterize the interaction between both proteins, I next attempted to identify the protein domains or motifs mediating the interaction. To locate interacting regions in E-Syt3, I generated (with the help of the student assistant Lea Schultz; see also methods section) RFP-E-Syt3 truncation constructs (Figure 3.11A) lacking (i) the ER-binding hairpin (E-Syt3ΔHP), (ii) additionally the SMP domain (E-Syt3 C2ABC) and (iii) additionally one or several C2 domains (E-Syt3 C2BC, E-Syt3 C2C-L, E-Syt3 C2C). The E-Syt3 C2C-L construct comprised besides the C2C domain the 177 aa-long linker region between C2B and C2C domains. As controls, RFP-E-Syt1 and RFP-E-Syt2 constructs lacking the ER-binding hairpins were also generated (E-Syt1ΔHP and E-Syt2ΔHP; Figure 3.11A).

In CHO cells, truncation constructs were co-expressed with free GFP (control) and

GFP-tubbyCT, respectively. GFP and RFP fluorescences were subsequently imaged by TIRF microscopy.

Experiments shown in Figure 3.11 were performed either by myself or by the student assistant Lea Schultz who carried out experiments conceived by me under my supervision. Data were analyzed by me. The particular origin of the data shown in Figure 3.11 is given in the figure legend.

In Figure 3.11B representative images of control cells expressing E-Syt full-length and truncation constructs are shown. Full-length constructs localized to ER-PM junctions whereas truncation constructs – all of them lacking the ER-binding hairpin – were distributed homogeneously throughout the PM. While homogeneous distribution of E-Syt1ΔHP and E-Syt2ΔHP was unaffected by co-expression of tubbyCT, E-Syt3ΔHP distribution was fundamentally altered in the presence of tubbyCT. As shown in Figure 3.11C-E, E-Syt3ΔHP was recruited into tubbyCT clusters. Co-localization of E-Syt3ΔHP with tubbyCT can be seen in the merged representative image as well as in the line profile in Figure 3.11E. Further step-wise truncation of E-Syt3 domains generated the same effect as long as the linker region region between C2B and C2C remained: TubbyCT over-expression induced cluster formation of the E-Syt3 truncation constructs E-Syt3 C2ABC (Figure 3.11F), E-Syt3 C2BC (Figure 3.11G) and E-Syt3 C2C-L (Figure 3.11H). In contrast, E-Syt3 C2C domain was not recruited into tubbyCT clusters (Figure 3.11I). Figure 3.11J shows a quantification of cluster areas of E-Syt truncation constructs in control cells and in cells co-expressing tubbyCT.

With this experiment we map the interaction region of E-Syt3 with tubbyCT to the linker between the C2B and C2C domains. Moreover, the results strongly confirm the interaction of tubbyCT with E-Syt3 and its specificity among the E-Syt isoforms.

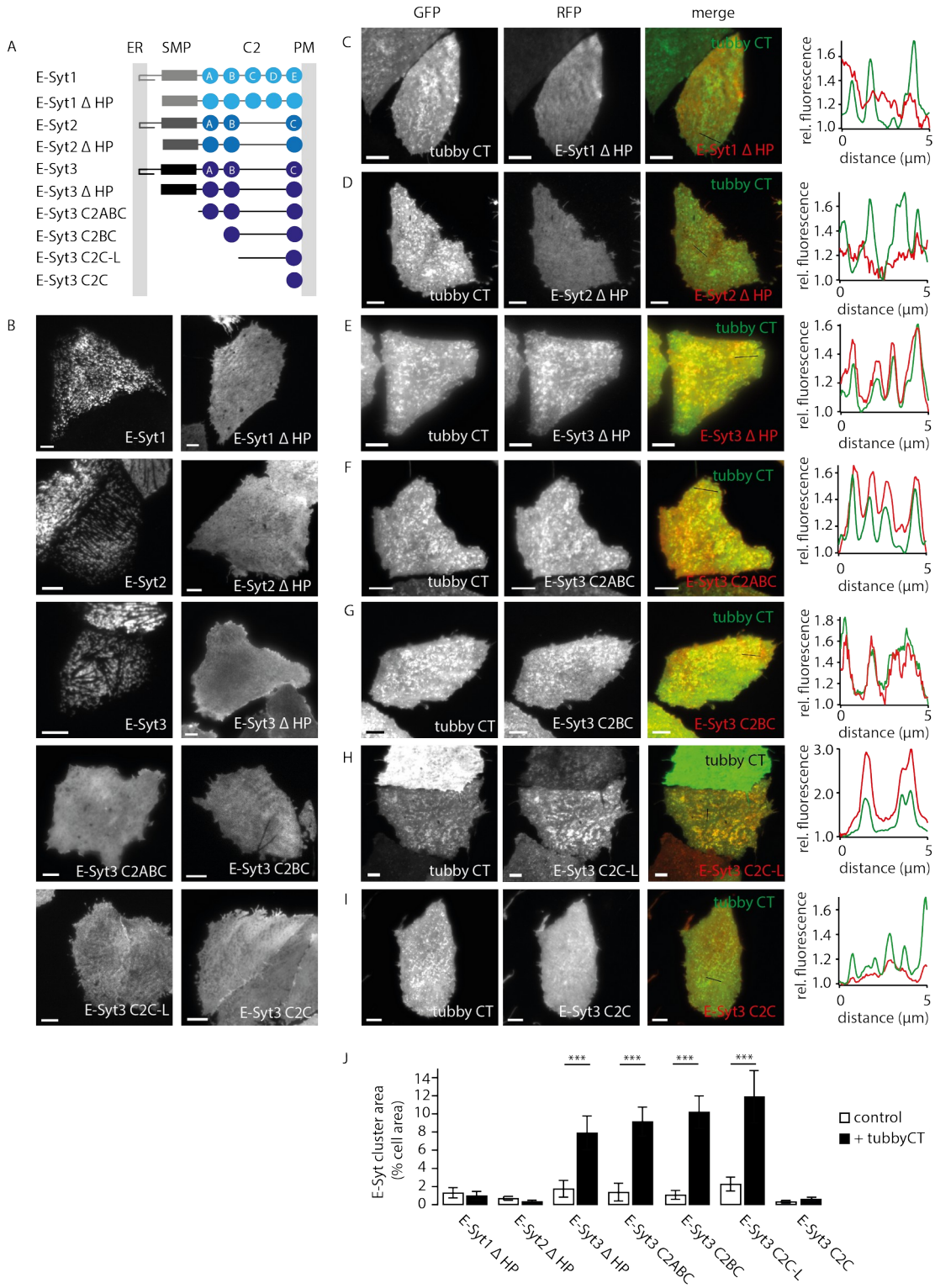

Figure 3.11: Mapping the region in E-Syt3 interacting with tubbyCT
(**A**) Schematic representation of E-Syt full-length and truncation constructs. HP = ER-binding hairpin. SMP domains are shown in gray rectangles, C2 domains in blue circles. (**B**) Example RFP TIRF images of CHO cells co-expressing RFP-E-Syt full-length and truncation constructs with free GFP, respectively. Scale bar = 5 µm. TIRF images of cells expressing E-Syt3 C2BC and E-Syt3 C2C-L were taken by Lea Schultz (LS), all other images were taken by Veronika Thallmair (VT). (**C-I**) Example TIRF images of CHO cells co-expressing GFP-tubbyCT and

RFP-tagged E-Syt truncation constructs. In the first column GFP images are shown followed by RFP and merged images. Line profiles along a distance of 5 µm are plotted on the right. GFP and RFP fluorescences were normalized to respective minimal values. In line profiles and merged images GFP fluorescence is shown in green and RFP fluorescence in red. Images shown in (C, E, F, I) were taken by VT, example cells in (D, G, H) were taken by LS. (**J**) Cell area occupied by E-Syt clusters in CHO cells co-expressing RFP-E-Syt truncation constructs together with free GFP (control, example cells shown in (B)) and GFP-tubbyCT (example cells shown in (C-I)), respectively. E-Syt1 Δ HP: control: n = 3 cells (VT) + n = 4 cells (LS); + tubbyCT: n = 1 cell (VT) + n = 7 cells (LS); E-Syt2 Δ HP: control: n = 3 cells (VT) + n = 10 cells (LS); + tubbyCT: n = 4 cells (VT) + n = 8 cells (LS); E-Syt3 Δ HP: control: n = 5 cells (VT) + n = 7 cells (LS); + tubbyCT: n = 2 cells (VT) + n = 10 cells (LS); Students t test: p = 0.00668; E-Syt3 C2ABC: control: n = 4 cells (VT) + n = 8 cells (LS); + tubbyCT: n = 6 cells (VT) + n = 7 cells (LS); Students t test: p = 0.000312; E-Syt3 C2BC: control: n = 9 cells (LS); + tubbyCT: n = 14 cells (LS); Students t test: p = 0.000127; E-Syt3 C2C-L: control: n = 12 cells (LS); + tubbyCT: n = 10 cells (LS); Students t test: p = 0.00660; E-Syt3 C2C: control: n = 8 cells (VT) + n = 10 cells (LS); + tubbyCT: n = 5 cells (VT) + n = 14 cells (LS).

3.6 Coincidence detection of E-Syt3 and PI(4,5)P_2 determines tubbyCT localization to ER-PM junctions

The results described above that reveal the interaction of E-Syt3 with tubbyCT (Figure 3.10, 3.11) make E-Syt3 a prominent candidate for tubbyCT recruitment into ER-PM junctions. Indeed, in COS-7 cells E-Syt3 over-expression induced massive tubbyCT cluster formation (Figure 3.10A, B). However, in CHO cells, co-expression with tubbyCT resulted in cluster formation of E-Syt3ΔHP, in other words, reciprocal recruitment of E-Syt3ΔHP into ER-PM junctions. This demonstrates that – at least in this cell type – tubbyCT localization to ER-PM junctions is not abrogated by ectopic over-expression of E-Syt3ΔHP. Binding of native E-Syt3 as well as high junctional PI(4,5)P_2 concentrations could account for the high affinity of tubbyCT to ER-PM junctions in CHO cells. Therefore I next studied the influence of PI(4,5)P_2 depletion on tubbyCT localization into ER-PM junctions under resting conditions. First, I analyzed the effect of PI(4,5)P_2 depletion via ci-VSP which does not increase intracellular Ca^{2+} levels and thus does not stimulate PI(4,5)P_2 resynthesis at ER-PM junctions. Figure 3.2B shows that activation of ci-VSP results in the strong translocation of tubbyCT from the PM into the cytoplasm. I further analyzed the same data set (originally recorded by Michael G. Leitner) spatially in terms of translocation dynamics in the clustered (i.e. ER-PM junctions) versus the non-clustered regions. Figure 3.12A shows that activation of ci-VSP depletes tubbyCT also from clusters, directly demonstrating the impact of PI(4,5)P_2 on binding of tubbyCT into ER-PM junctions. However, fractional dissociation of tubbyCT from the ER-PM junctions was slightly, but significantly less

compared to the non-clustered region (Figure 3.12B).

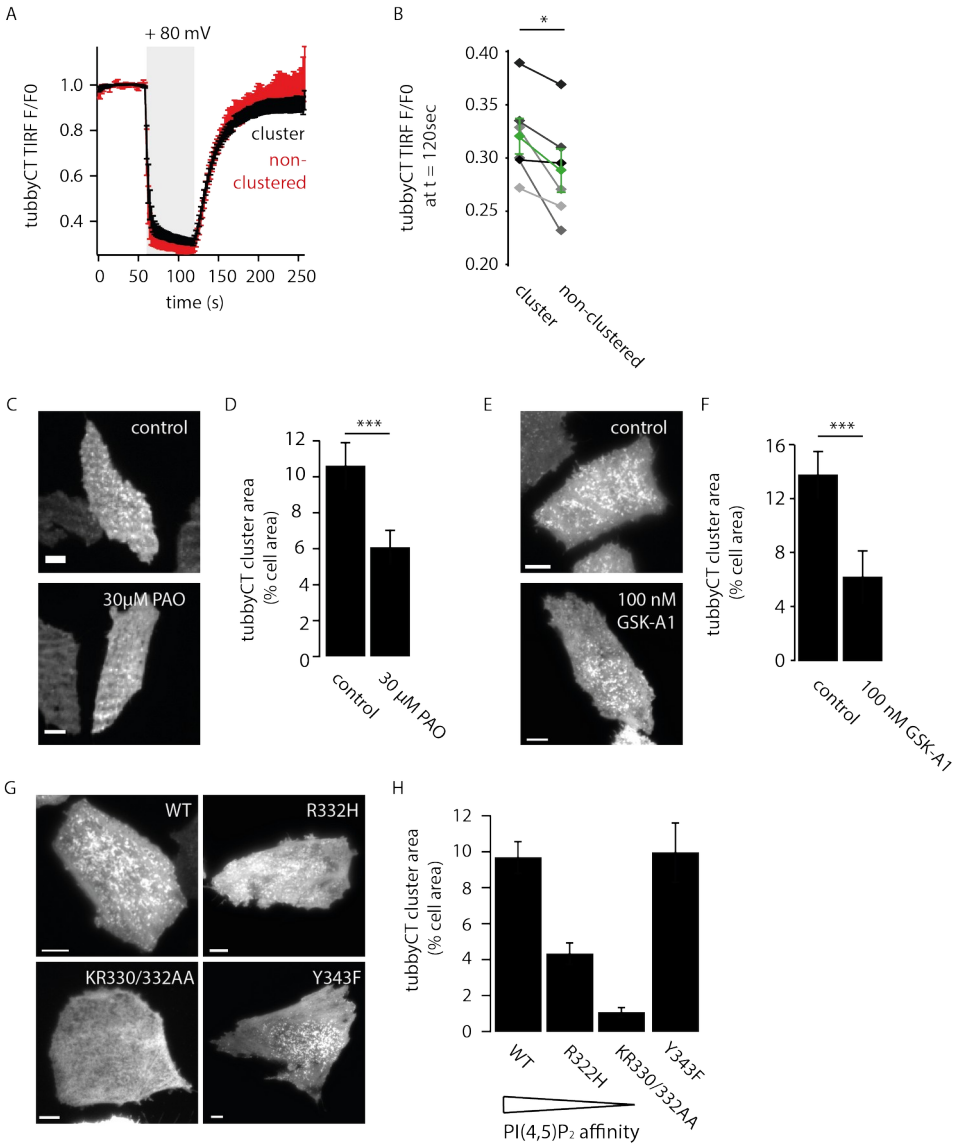

Figure 3.12: Probing the influence of PI(4,5)P_2 on tubbyCT localization to ER-PM junctions

(**A, B**) TIRF imaging of CHO cells transiently expressing GFP-tubbyCT and ci-VSP. Ci-VSP was activated by depolarization of the PM to +80 mV. Experiments were performed by Michael G. Leitner, data analysis was done by Veronika Thallmair. n = 6 cells. (A) Time course of normalized tubbyCT PM association in the clustered and non-clustered region. Mean ± SEM is shown. (B) Normalized tubbyCT response at t = 120sec in the clustered and non-clustered region of individual cells. Paired students t test: p = 0.0275. (**C-F**) TIRF imaging of CHO cells transiently expressing GFP-tubbyCT. Cells were incubated in extracellular solution (control) or PI4K inhibitors (C, D 30 µM PAO; E, F 100 nM GSK-A1) prior to imaging. (**C, E**) Example images. Scale bar = 5 µm. (**D**) TubbyCT cluster area of CHO cells shown exemplary in (C). Control: n = 16 cells, PAO: n = 14 cells; Students t test: p = 0.00695. (**F**) TubbyCT cluster area of CHO cells shown exemplary in (E). Control: n = 16 cells, GSK-A1: n = 12 cells; Students t test: p = 0.00578. (**G, H**) TIRF imaging of CHO cells transiently expressing GFP-tubbyCT wild-type (WT), R332H, KR330/332AA and Y343F mutants, respectively. (**G**) Example images. Scale bar = 5 µm. (**H**) TubbyCT cluster area of CHO cells shown exemplary in (G). WT: n = 39 cells; R332H: n = 33 cells; KR330/332AA: n = 31 cells; Y343F: n = 19 cells.

Next, I modulated PM $PI(4,5)P_2$ content by incubation of tubbyCT-expressing CHO cells in PI4K inhibitors PAO and GSK-A1. As already shown in Figure 3.5C, D, this reversed PLCβ-induced membrane dynamics, but it also resulted in reduced cluster area under resting conditions compared to control cells (Figure 3.12C-F) and thereby supports the idea that $PI(4,5)P_2$ binding is a crucial factor for localization of tubbyCT to ER-PM junctions.

If this was the case, lowering the $PI(4,5)P_2$ affinity of tubbyCT should also result in reduced clustering. In Figure 3.5B I demonstrated that lowering its $PI(4,5)P_2$ affinity dramatically affects PLCβ-induced tubbyCT dynamics. The mutant with intermediate $PI(4,5)P_2$ affinity (tubbyCT R332H) as well as the mutant with (almost) lost $PI(4,5)P_2$ binding (tubbyCT KR330/332AA) lack membrane recruitment following PLCβ activation. Here, I analyzed the same data in terms of tubbyCT clustering under resting conditions. Figure 3.12G, H illustrates that clustering was strongly affected in tubbyCT mutants with reduced $PI(4,5)P_2$ affinity. TubbyCT R332H holded a significantly reduced cluster area compared to the wild-type control and in the KR330/332AA mutant clusters were essentially lost. In contrast, in the Y343F mutant cluster formation was not affected consistent with its unchanged $PI(4,5)P_2$ affinity.

In summary, these experiments clearly demonstrate the dependence of tubbyCT localization to ER-PM contact sites on $PI(4,5)P_2$. Nevertheless, E-Syt3 can also recruit tubbyCT into clusters as seen in COS-7 cells (Figure 3.10A, B). Hence, I wondered whether this E-Syt3-mediated recruitment is also $PI(4,5)P_2$-dependent.

In CHO cells I co-expressed the $PI(4,5)P_2$ binding-deficient mutant GFP-tubbyCT KR330/332AA with RFP-E-Syt1-3, respectively. GFP and RFP fluorescence under resting conditions was imaged by TIRF microscopy. As seen in Figure 3.12G, H GFP-tubbyCT KR330/332AA labeled the PM homogeneously. Co-expression with E-Syt1 and E-Syt2 induced slight accumulation of tubbyCT KR330/332AA in stripes, which could represent stress fibers. However, these structures were not populated by E-Syt1/2, which can be seen best in merged images and line profiles (Figure 3.13A, B). Also Pearson's coefficients did not reveal co-localization of tubbyCT KR330/332AA with E-Syt1/2 (Figure 3.13D). In contrast, co-expression with E-Syt3 induced tubbyCT KR330/332AA clustering and resulting clusters clearly co-localized with E-Syt3 (Figure 3.13C, D). Clustering was significantly increased compared to control

conditions (Figure 3.13E). This clarifies that E-Syt3 binding of tubbyCT can occur independent of PI(4,5)P_2 binding.

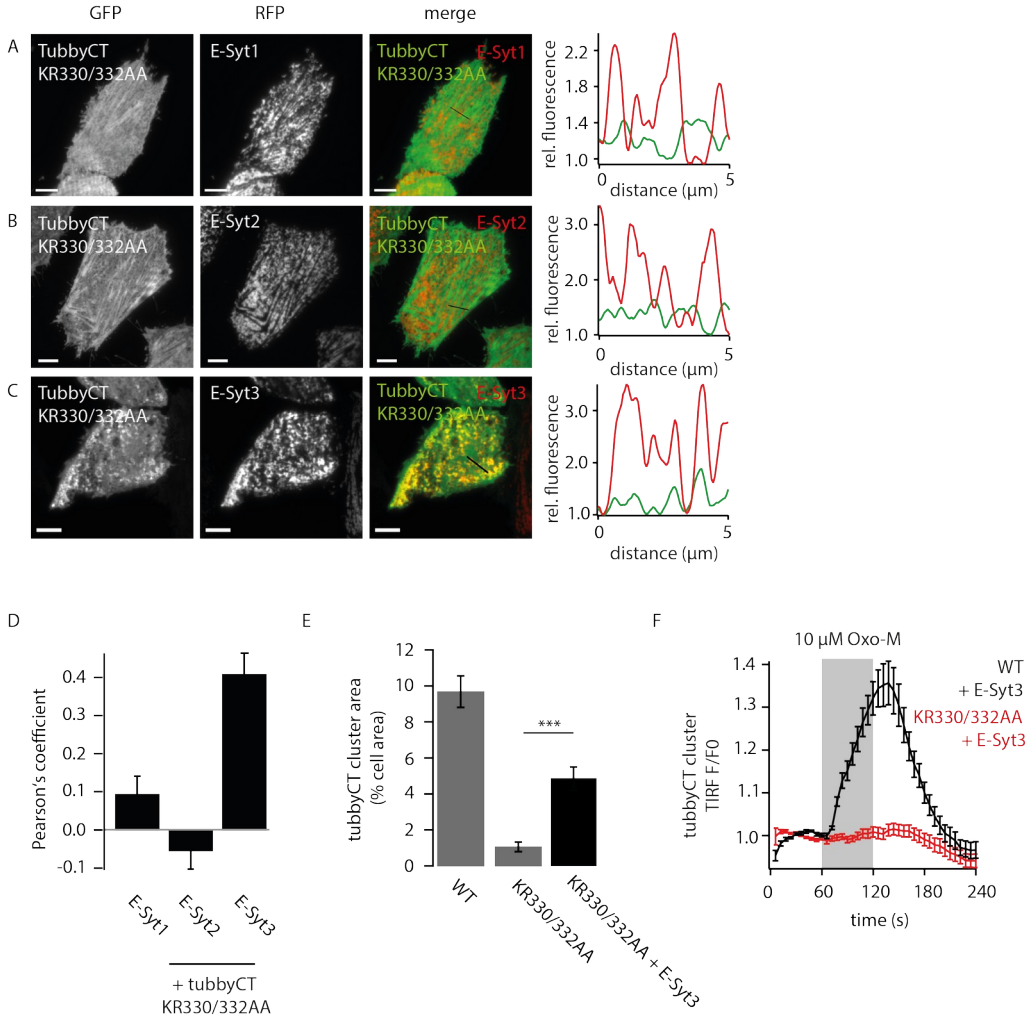

Figure 3.13: Co-expression of tubbyCT KR330/332AA mutant with E-Syts
(**A-C**) Example TIRF images of CHO cells co-expressing GFP-tubbyCT KR330/332AA and RFP-tagged E-Syt1 (A), E-Syt2 (B) and E-Syt3 (C), respectively. Scale bar = 5 µm. Line profiles over a distance of 5 µm (highlighted in merged images) are plotted on the right. Fluorescence intensities are normalized to respective minimal values. In line profiles and merged images GFP fluorescence is shown in green, RFP fluorescence in red. (**D**) Pearson's coefficients (mean ± SEM) from images shown exemplary in (A-C). TubbyCT KR330/332AA + E-Syt1: n = 27 cells. + E-Syt2: n = 26 cells. + E-Syt3: n = 30 cells. (**E**) Area of GFP- tubbyCT KR330/332AA clusters with and without co-expression of RFP-E-Syt3. Grey bars are replotted from Figure 3.12D. KR330/332AA + E-Syt3: n = 43 cells; Students t test: p = 0.00000122. (**E**) TIRF imaging of CHO cells transiently expressing RFP-E-Syt3 and GFP-tubbyCT WT and KR330/332AA mutant, respectively. Time courses (mean ± SEM) of tubbyCT cluster fluorescence upon activation of PLCβ. WT + E-Syt3: n = 14 cells. KR330/332AA + E-Syt3: n = 34 cells.

3.7 TubbyCT recruitment reflects PLCβ-induced PI(4,5)P_2 synthesis at ER-PM junctions

Coincidence binding of PI(4,5)P_2 and E-Syt3 drives tubbyCT localization to ER-PM junctions under resting conditions. In Figure 3.5C, D it is also shown that further recruitment upon PLCβ activation depends on PI4K activity and thus on PI(4,5)P_2 resynthesis. However, given that PM binding of E-Syts is also PI(4,5)P_2-dependent (Giordano *et al*., 2013), activation of PLCβ and inhibition of PI4K most likely also affect E-Syt localization to ER-PM contact sites. Consequently, it is possible that PI4K inhibition only indirectly affects tubbyCT recruitment by altering PLCβ-induced E-Syt3 dynamics. Thus, I aimed at disentangling the contributions of direct PI(4,5)P_2 binding on PLCβ-induced tubbyCT recruitment from an indirect PI(4,5)P_2 dependence via E-Syt3 binding.

Therefore, CHO cells were co-transfected with RFP-ESyt3 and GFP-tubbyCT wild-type (WT) and GFP-tubbyCT KR330/332AA, respectively. E-Syt3 co-expression induced clustering of the PI(4,5)P_2 binding deficient tubbyCT KR330/332AA (Figure 3.13C-E). TubbyCT KR330/332AA dynamics upon PLCβ activation were measured in these E-Syt3-induced clusters. Any tubbyCT membrane association dynamics of this mutant must be PI(4,5)P_2-independent and thus reports on the isolated effect of PLCβ-induced E-Syt3 recruitment on tubbyCT localization. As a control, tubbyCT WT cluster dynamics in cells co-expressing E-Syt3 were measured.

In E-Syt3-evoked tubbyCT KR330/332AA clusters PLCβ stimulation did not induce PM recruitment of the tubbyCT mutant, whereas tubbyCT WT was robustly recruited to PM clusters (Figure 3.13E). Consequently, tubbyCT recruitment to E-Syt3-containing ER-PM junctions must be driven directly by increasing PI(4,5)P_2 levels. Notably, this conclusion makes tubbyCT a suited sensor to measure PI(4,5)P_2 dynamics at E-Syt3-rich ER-PM junctions. Most importantly, however, the central conclusion is that during PLCβ stimulation, at E-Syt3-containing ER-PM junctions PI(4,5)P_2 levels rise despite the known fall of this phosphoinositide species in the bulk membrane.

A possible reason why tubbyCT is suitable for detection of local PI(4,5)P_2 resynthesis is its predominant localization to ER-PM contact sites already under resting conditions. Additionally, its PI(4,5)P_2 binding mechanism could account for this property. I wondered whether the PI(4,5)P_2 sensors PLCδ1-PH and the Epsin1 ENTH domain also

detect PI(4,5)P_2 synthesis at tubbyCT clusters. In CHO cells RFP-tubbyCT was co-expressed with PLCδ1-PH-GFP and GFP-ENTH, respectively. PLCβ was activated while RFP and GFP fluorescence was measured by TIRF microscopy. As expected, tubbyCT was recruited to its PM clusters (i.e. ER-PM junctions), whereas it was depleted in homogeneously labeled membrane regions (Figure 3.14A, D). In contrast, neither PLCδ1-PH nor the ENTH domain were recruited to the regions covered by tubbyCT clusters. Both sensors showed a robust translocation from the tubbyCT cluster region into the cytoplasm which was not significantly different from the translocation in the non-clustered area (Figure 3.14B, C, E, F). These findings indicate that the resting localization is not the only reason why tubbyCT detects local PI(4,5)P_2 synthesis.

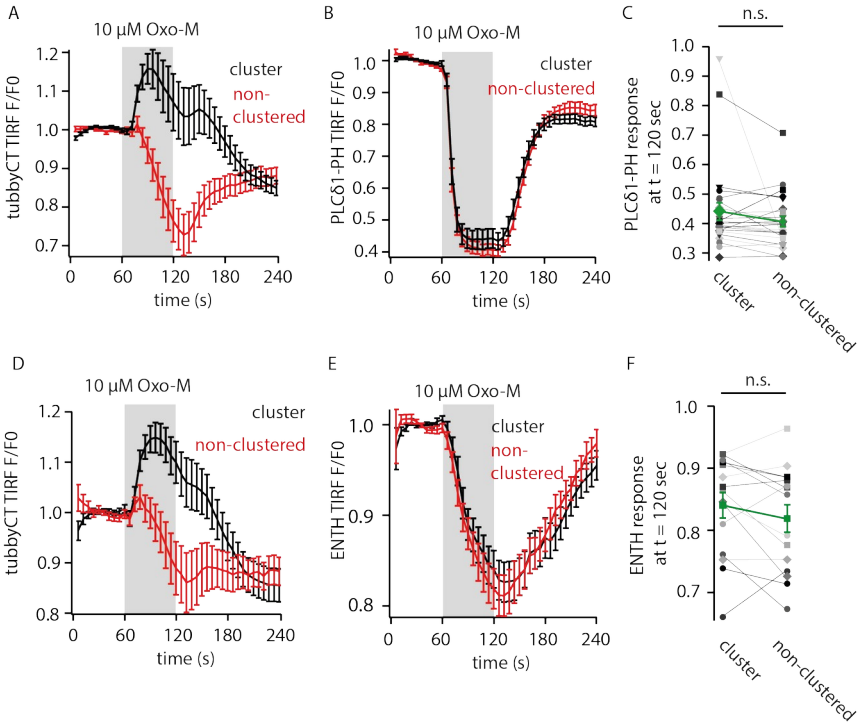

Figure 3.14: PI(4,5)P_2 sensor dynamics at tubbyCT clusters
(**A-C**) TIRF imaging of CHO cells co-expressing RFP-tubbyCT and PLCδ1-PH-GFP. PLCβ was activated by application of 10 µM Oxo-M and RFP and GFP dynamics were measured in tubbyCT clustered and non-clustered regions. n = 25 cells. (A) TubbyCT dynamics in its clustered and non-clustered regions. Mean ± SEM of normalized traces are shown. (B) PLCδ1-PH dynamics (mean ± SEM) in the same tubbyCT clustered and non-clustered regions as in (A). (C) PLCδ1-PH response at t = 120 sec of individual cells. Paired students t test: p = 0.175. (**D-F**) TIRF imaging of CHO cells co-expressing RFP-tubbyCT and GFP-Epsin1-ENTH. Experiments and data analysis was performed as described in (A-C). n = 15 cells. (F) Paired students t test: p = 0.163.

3.8 PI4P dynamics at ER-PM junctions do not differ from dynamics in the bulk PM

Since $PI(4,5)P_2$ is generated from PI by sequential phosphorylation of positions 4 and 5 of its inositol ring, I was next interested whether the intermediate PI4P also locally accumulates at ER-PM contact sites.

Hence, I analyzed PI4P dynamics at tubbyCT clusters compared to the non-clustered area. I co-transfected CHO cells with RFP-tubbyCT and with the PI4P sensor, GFP-P4M-SidMx1 (Hammond *et al.*, 2014) to synchronously monitor both phosphoinositide species. TubbyCT translocation to its clusters, as well as its depletion from the non-clustered region was detected by TIRF microscopy, as expected (Figure 3.15A). In contrast, activation of PLCβ induced dissociation of P4M-SidMx1 both from the ER-PM junctions marked by tubbyCT clustering and from the non-clustered area, with only slightly (although significant) less dissociation from the junctional area (Figure 3.15B, C). Moreover, the whole-cell P4M-SidMx1 response positively correlated with the whole-cell tubbyCT response (Figure 3.15D).

Thus, different from $PI(4,5)P_2$, PI4P is either not locally synthesized at ER-PM junctions, or if so, it is not accessible to the sensor, perhaps because it is immediately consumed by further phosphorylation to $PI(4,5)P_2$ ('metabolic channeling', see Discussion).

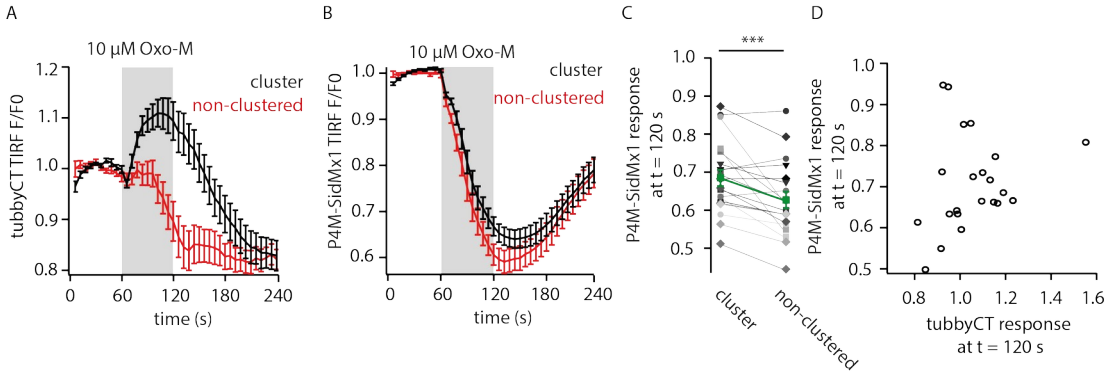

Figure 3.15: PI4P sensor dynamics at tubbyCT clusters
TIRF imaging of CHO cells co-expressing RFP-tubbyCT and GFP-P4M-SidMx1. PLCβ was activated by application of 10 µM Oxo-M and RFP and GFP dynamics were measured in tubbyCT clustered and non-clustered regions. n = 20 cells. (**A**) tubbyCT dynamics in its clustered and non-clustered regions. Mean ± SEM of normalized traces are shown. n = 20 cells. (**B**) P4M-SidMx1 dynamics (mean ± SEM) in the same tubbyCT clustered and non-clustered regions as in (A). (**C**) P4M-SidMx1 response at t = 120 sec of individual cells. n = 20 cells; paired students t test: p = 0.00123. (**D**) Correlation of PM P4M-SidMx1 and PM tubbyCT response of individual cells. n = 22 cells.

3.9 Local $PI(4,5)P_2$ increase during global $PI(4,5)P_2$ depletion maintains functionality of ER-PM junctions

Next, I aimed at understanding the role of the newly identified local increase in $PI(4,5)P_2$ concentration at ER-PM junctions. Because many ER-PM tethers including the E-Syts are ER-resident proteins which bind PM $PI(4,5)P_2$ in trans, a massive drop in junctional $PI(4,5)P_2$ concentration following PLCβ activation should affect the integrity of ER-PM contact sites and thus PI transfer activity and $PI(4,5)P_2$ resynthesis (exactly at the time when it is needed most). Therefore, I hypothesized that local $PI(4,5)P_2$ synthesis and upkeep or even increase of $PI(4,5)P_2$ is crucial for the preservation of the connectivity between ER and PM and consequently for the functionality of ER-PM contact sites.

Thus, I tested if inhibition of $PI(4,5)P_2$ resynthesis impairs ER-PM connectivity upon PLCβ activation. To this end, I investigated the effect of PI4K inhibition on E-Syt dynamics. CHO cells were transiently transfected with GFP-E-Syt1-3, respectively. PM E-Syt dynamics upon activation of PLCβ were measured by TIRF microscopy. Prior to imaging, cells were incubated in PI4K inhibitor GSK-A1 (10 nM and 100 nM) for 10 min. Control cells were incubated in extracellular solution.

E-Syt dynamics upon PLCβ activation were severely affected by PI4K inhibition. Under control conditions, E-Syt1 was transiently recruited to the PM. This recruitment was curtailed temporally (at 10 nM GSK-A1) and dramatically decreased (at 100 nM GSK-A1) by PI4K inhibition. In cells incubated with 100 nM GSK-A1, E-Syt1 PM localization was even reduced compared to baseline levels following PLCβ activation (Figure 3.16A). PLCβ activation induced reversible E-Syt2 translocation into the cytoplasm, which was strongly increased by PI4K inhibition. Moreover, recovery was delayed in cells incubated in GSK-A1 (Figure 3.16B). E-Syt3 showed a minor PLCβ-induced PM recruitment under control conditions. This recruitment was PI4K-dependent as incubation of cells in GSK-A1 induced a PLCβ-dependent translocation of E-Syt3 into the cytoplasm (Figure 3.16C).

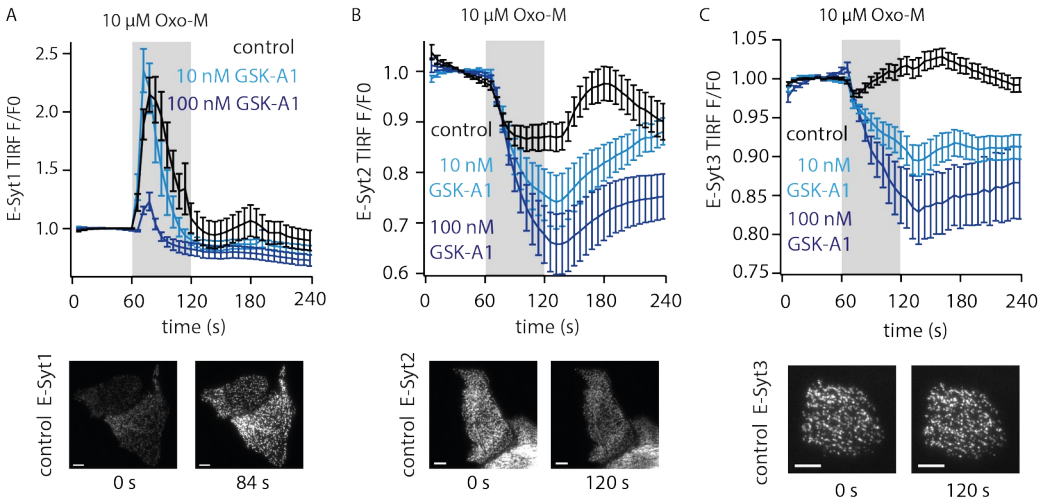

Figure 3.16: Influence of PI4K inhibition on PLCβ-induced E-Syt dynamics
TIRF imaging of CHO cells transiently expressing GFP-tagged E-Syt1 (**A**), E-Syt2 (**B**) and E-Syt3(**C**). Cells were incubated in extracellular solution (control), 10 nM and 100 nM GSK-A1, respectively prior to imaging. Time courses (mean ± SEM of normalized traces) upon activation of PLCβ are shown. Example images under resting conditions and at maximal recruitment (E-Syt1) and maximal PLCβ activation (E-Syt2/3), respectively are depicted below. Scale = 5 µm. (A) control: n = 20 cells; 10 nM GSK-A1: n = 16 cells; 100 nM GSK-A1: n = 15 cells. (B) control: n = 23 cells; 10 nM GSK-A1: n = 16 cells; 100 nM GSK-A1: n = 16 cells. (C) control: n = 42 cells; 10 nM GSK-A1: n = 27 cells; 100 nM GSK-A1: n = 26 cells.

While consistent with the previously described $PI(4,5)P_2$-dependency of PM tethering by E-Syts these findings for the first time reconcile this property with $PI(4,5)P_2$ consumption during PLC activity: locally enhanced resynthesis ensures high $PI(4,5)P_2$ levels during PLCβ activation and thereby secures unabated ER-PM tethering during this signaling modality.

3.10 Study of diverging tubbyCT dynamics in CHO and COS-7 cells

In CHO cells, tubbyCT is localized to ER-PM junctions where its further, PLCβ-induced recruitment reflects local $PI(4,5)P_2$ resynthesis. The localization to ER-PM junctions is driven by coincidence detection of $PI(4,5)P_2$ and E-Syt3. In contrast in COS-7 cells, tubbyCT does not preferentially localize to ER-PM contact sites. It is homogeneously distributed across the PM and consequently activation of PLCβ causes its translocation into the cytoplasm. Possible explanations for these cell-type specific differences could be distinct amounts of E-Syt3-mediated ER-PM junctions, varying protein and $PI(4,5)P_2$ content at ER-PM contact sites as well as different $PI(4,5)P_2$ dynamics.

In the following experiments I aimed at understanding the reasons for diverging

tubbyCT responses in COS-7 and CHO cells. In all experiments described previously in this work, CHO cells were imaged in low to intermediate density, i.e. maximum 50% of the dish surface was covered by single cells or small cell islets. As I observed a decrease of tubbyCT response with increasing cell density (Figure 15A), the approximately 50% dish coverage was selected per default as a compromise between a robust tubbyCT PM recruitment and a reasonable amount of imagable cells. However, in order to elucidate the differences between COS-7 and CHO cells, I included differentially dense grown CHO cells into the study.

3.10.1 E-Syt dynamics in CHO and COS-7 cells

In Figure 3.17A, tubbyCT dynamics upon PLCβ activation are depicted. COS-7 and single CHO cell traces are replotted from Figure 3.2G. Here, I additionally included tubbyCT dynamics in small CHO cell islets and confluently grown CHO cells. PLCβ-induced tubbyCT recruitment was decreased in small CHO cell islets and almost lost in confluent CHO cells. In COS-7 cells the sensor dissociated into the cytoplasm.

To test whether reverse tubbyCT dynamics in CHO and COS-7 cells are driven by reverse $PI(4,5)P_2$ dynamics, I studied E-Syt dynamics in these cell types. In CHO cell islets, transfected GFP-E-Syt1 was transiently recruited to ER-PM contact sites following 10 µM Oxo-M application. Also during wash-out transient recruitment to ER-PM junctions was observed in a portion of imaged cells. In contrast, PLCβ activation induced GFP-E-Syt2 dissociation, whereas GFP-E-Syt3 was slightly recruited to ER-PM junctions (Figure 3.17B).

In COS-7 cells, E-Syt1 dynamics did not differ from those in CHO cells and also E-Syt2 showed a similar fluorescence decrease. However, E-Syt2 relocalization to ER-PM junctions during Oxo-M wash-out was slower in COS-7 cells than in CHO cells. Moreover, in COS-7 cells E-Syt3 dissociated from ER-PM contact sites upon PLCβ activation (Figure 3.17C). Thus, E-Syt3 dynamics rather resembled E-Syt2 dynamics and differed fundamentally from those observed in CHO cells.

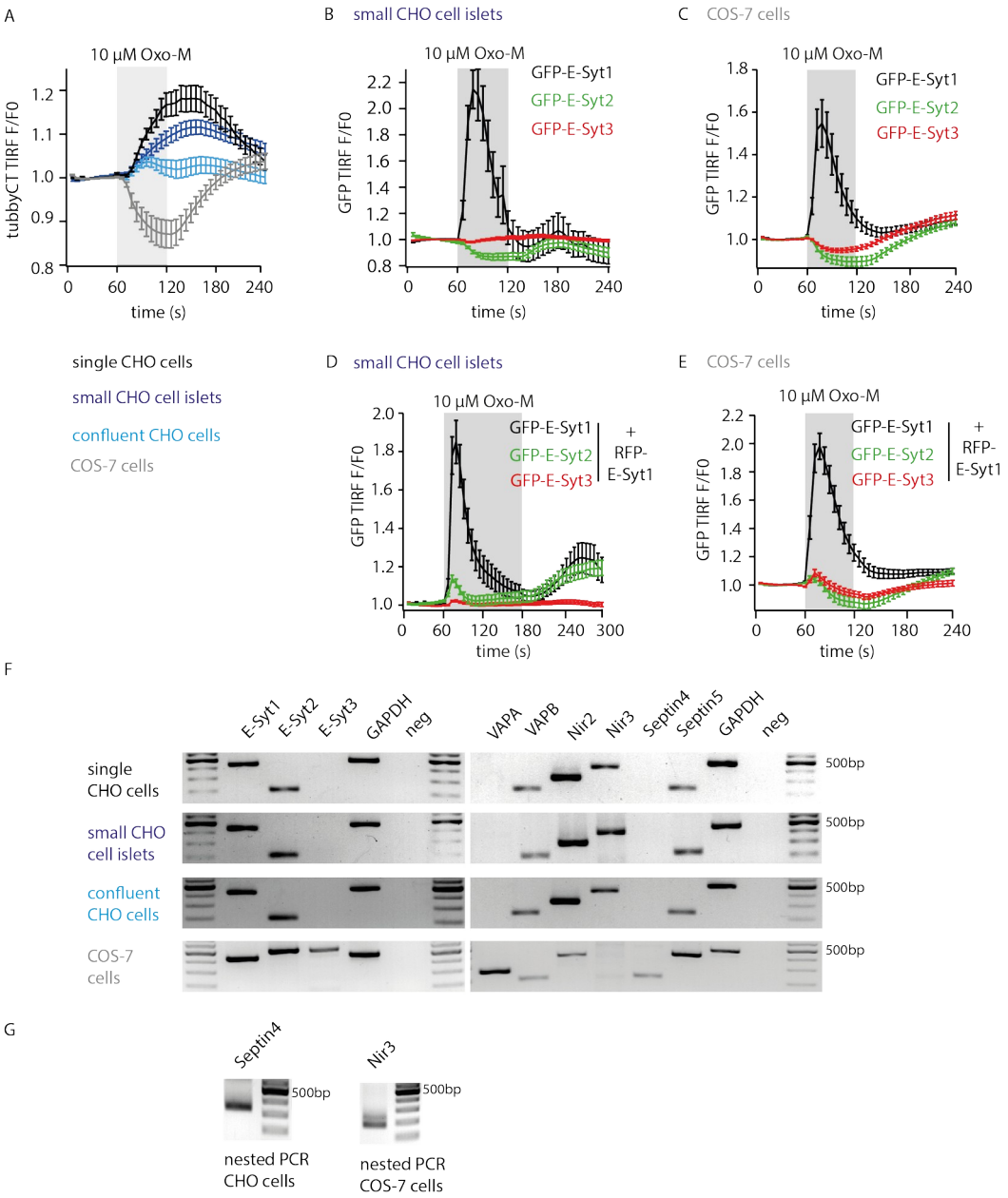

Figure 3.17: Comparison of E-Syt dynamics and gene expression in CHO and COS-7 cells (**A**) TIRF imaging of GFP-tubbyCT-expressing CHO and COS-7 cells. PM tubbyCT dynamics (mean ± SEM of normalized traces) upon activation of PLCβ are shown. CHO cells were seeded in different densities and imaging was performed on single cells (black), small cell islets (dark blue) and confluently grown cells (light blue). COS-7 cells were imaged in intermediate density. Single CHO cell and COS-7 traces were already shown in Figure 3.2H. Small CHO cell islets: n = 57 cells; Confluent CHO cells: n = 110 cells. (**B**) TIRF imaging of small CHO cell islets expressing GFP-E-Syt1, GFP-E-Syt2 and GFP-E-Syt3, respectively. Mean ± SEM of normalized traces are shown. PLCβ was activated by application of 10 µM Oxo-M. E-Syt1: n = 20 cells; E-Syt2: n = 23 cells; E-Syt3: n = 42 cells. Data has already been shown as control traces in Figure 3.16. (**C**) Same experiment as in (B), performed in COS-7 cells. E-Syt1: n = 40 cells; E-Syt2: n = 55 cells; E-Syt3: n = 55 cells. (**D**) Same experiment as in (B), with CHO cells additionally co-expressing RFP-E-Syt1. E-Syt1: n = 33 cells; E-Syt2: n = 53 cells; E-Syt3: n = 56 cells. (**E**) Same experiment as in (D), performed in COS-7 cells. E-Syt1: n = 26 cells; E-Syt2: n = 32 cells; E-Syt3: n = 36 cells. (**F**) RT-PCRs of indicated genes, GAPDH was used as

house-keeping gene control, negative control contained no RNA. RNA was extracted from CHO cells of indicated density and from COS-7 cells. (**G**) Nested PCRs on PCR products obtained from RT-PCRs shown in (F).

The PLCβ-induced dissociation of E-Syt2/3 from ER-PM junctions was unexpected, as both proteins are described to be at least transiently recruited to ER-PM contact sites under these conditions. As they are not directly Ca^{2+}-dependent, recruitment occurs via binding to E-Syt1 (Tremblay *et al*., 2015, Idevall-Hagren *et al*., 2015). In my experimental setting E-Syt1 was not additionally over-expressed, thus missing GFP-E-Syt2/3 recruitment to ER-PM contact sites could be explained by the saturation of native E-Syt1 with native, untagged E-Syt2/3. Hence, I additionally addressed GFP-E-Syt1-3 dynamics in presence of over-expressed RFP-E-Syt1. In CHO as well as in COS-7 cells, co-expression of RFP-E-Syt1 did not notably alter GFP-E-Syt1 dynamics (Figure 3.17D, E). In contrast, in both cell types RFP-E-Syt1 expression induced transient GFP-E-Syt2/3 recruitment to ER-PM contact sites which was not observed before. This translocation occurred at the same time point as E-Syt1 recruitment and most likely reflected heterodimerization with RFP-E-Syt1. E-Syt2/3 transient recruitment was followed by a dissociation to baseline levels in CHO cells (Figure 3.17D) and below baseline levels in COS-7 cells (Figure 3.17E).

In summary, PLCβ-induced dissociation of E-Syt3 from ER-PM contact sites only occurred in COS-7 but not CHO cells. This is in agreement with reverse tubbyCT dynamics in these cell types and suggests different $PI(4,5)P_2$ dynamics at E-Syt3-rich ER-PM junctions. As also E-Syt2 dynamics differed between the two cell types, $PI(4,5)P_2$ dynamics might also vary at ER-PM junctions tethered by E-Syt2.

3.10.2 Expression levels of ER-PM junctional proteins in CHO and COS-7 cells

Varying PI(4,5)P_2 dynamics might be explained by different protein compositions at ER-PM junctions in COS-7 and CHO cells. Therefore, I performed RT-PCRs to visualize mRNA levels of E-Syt1-3, Nir2/3, VAP-A/B and Septin4/5. Septins form filamentous structures and subcompartmentalize the PM. I included septin4/5 to the RT-PCRs as they are described to serve as diffusion barriers around ER-PM contact sites (Sharma *et al.*, 2013; Maléth *et al.*, 2014). GAPDH was used as house-keeping gene control. I performed RT-PCRs from cell lysates of differentially dense grown CHO cells and from COS-7 cell lysates. mRNA levels of investigated genes did not vary in CHO cells with different density (Figure 3.17F). However, substantial differences between CHO and COS-7 cells were observed (Figure 3.17F). Surprisingly, E-Syt3 could not be amplified from CHO cell mRNA, although five different primer pairs and five different nested primer pairs were tried (see also methods section, Table 5). In contrast, in COS-7 cells E-Syt3 was detected. Moreover, VAP-A expression was very low but detectable in CHO cells, whereas it was strongly expressed in COS-7 cells. Nir2/3 expression was high in CHO cells, whereas in COS-7 cells it was low and in case of Nir3 only detected with a nested PCR (Figure 3.17G). Septin4, although highly expressed in COS-7 cells, showed low expression levels in CHO cells (Nested PCR, Figure 3.17G).

Taken together, observed differences in PI(4,5)P_2 dynamics might be explained by a completely different ER-PM junction architecture in COS-7 and CHO cells, reflected in different expression levels of respective proteins. Especially observed differences in Nir3 expression might explain different local PI(4,5)P_2 levels under resting conditions and therefore distinct tubbyCT recruitment to ER-PM junctions. Moreover, divergent Nir2 expression levels could account for varying PI(4,5)P_2 dynamics upon PLCβ activation.

Therefore, I examined in the next section whether abundance of junctional proteins like E-Syt3 and Nir2/3 changes PI(4,5)P_2 synthesis as reported by tubbyCT dynamics.

3.10.3 Influence of E-Syt3 over-expression on tubbyCT dynamics

I first tested the influence of E-Syt3 over-expression on tubbyCT dynamics at ER-PM contact sites. CHO and COS-7 cells were co-transfected with GFP-tubbyCT and RFP-E-Syt3 and free RFP (control), respectively and subsequently imaged by TIRF

microscopy. As shown before (see Figure 3.10A, B) over-expression of E-Syt3 did not induce additional tubbyCT clustering in CHO cells. However, E-Syt3 over-expression significantly enhanced PLCβ-induced recruitment of tubbyCT into the ER-PM contact sites (Figure 3.18A, B). Although over-expression of E-Syt3 in COS-7 cells induced strong tubbyCT cluster formation (Figure 3.10A, B) overall tubbyCT dynamics were not changed detectably, as PLCβ activation induced the same degree of tubbyCT translocation as seen in control cells (Figure 3.18C, D). Nevertheless, dissociation of tubbyCT from the E-Syt3-induced clusters was significantly less than from the non-clustered region (Figure 3.18E, F). Taken together, over-expression of E-Syt3 slightly enhanced PI(4,5)P_2 resynthesis at ER-PM junctions.

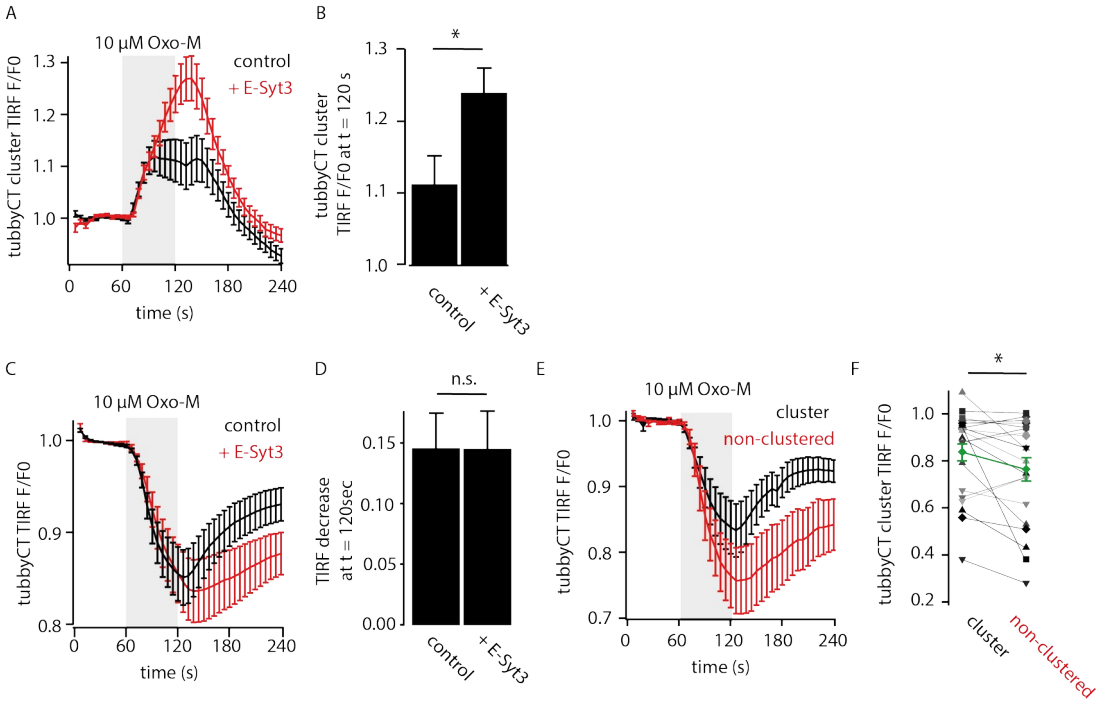

Figure 3.18: Influence of E-Syt3 over-expression on tubbyCT dynamics
(**A, B**) TIRF imaging of CHO cells transiently co-expressing GFP-tubbyCT and free RFP (control) and RFP-E-Syt3, respectively. TubbyCT cluster fluorescence upon activation of PLCβ by application of 10 µM Oxo-M. (A) Time courses (mean ± SEM) of normalized traces are plotted. (B) Normalized tubbyCT cluster fluorescence at t = 120 sec. Control: n = 27 cells; + E-Syt3: n = 33 cells. Students t test: p = 0.0210. (**C, D**) TIRF imaging of COS-7 cells transiently co-expressing GFP-tubbyCT and free RFP (control) and RFP-E-Syt3, respectively. TubbyCT PM fluorescence upon application of 10 µM Oxo-M is shown. (C) Time courses (mean ± SEM) of normalized traces. (D) Normalized fluorescence decrease (mean ± SEM) at t = 120 sec. Control: n = 21 cells; + E-Syt3: n = 22 cells. Students t test: p = 0.991. (**E, F**) TIRF imaging of COS-7 cells expressing GFP-tubbyCT and RFP-E-Syt3. Analysis of tubbyCT dynamics in E-Syt3-induced clusters as well as in the non-clustered region. PM dynamics of the same cells are shown in (C, D) (red) (E) Time courses (mean ± SEM) of normalized traces. (F) Normalized TIRF signal of tubbyCT at t = 120sec in the clustered and non-clustered regions of individual cells. n= 21 cells; Paired students t test: p = 0.0378.

3.10.4 Influence of Nir over-expression on tubbyCT localization and dynamics

I next studied the influence of over-expression of Nir2, Nir3, as well as dominant-negative Nir2 (Nir2 S164A) on tubbyCT clustering and its recruitment to PM clusters. In CHO cells GFP-tubbyCT was co-expressed with Nir2-mcherry, Nir3-mcherry, Nir2 S164A-mcherry and free RFP (control), respectively. GFP and RFP/mcherry fluorescence upon PLCβ activation was imaged by TIRF microscopy. Mutation of Nir2 S164 to alanine abolishes PI transfer (Kim *et al.*, 2013). As the recruitment of this mutant to ER-PM junctions should be unchanged, its over-expression should have a dominant-negative effect.

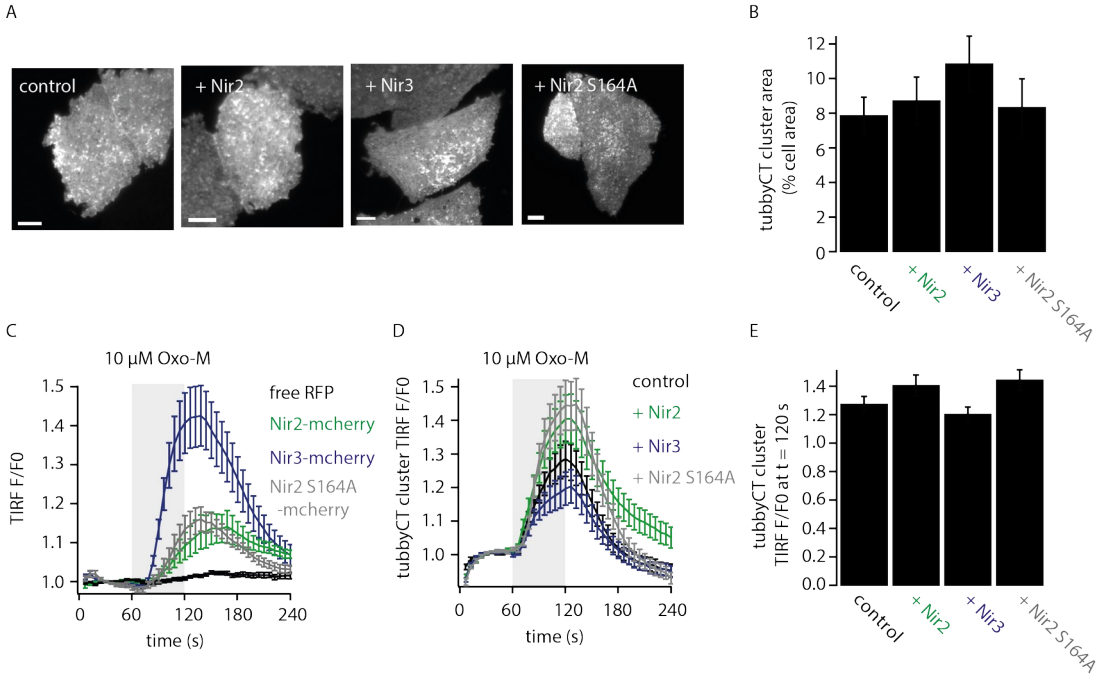

Figure 3.19: Influence of Nir2/3 on tubbyCT cluster formation and dynamics
TIRF imaging of CHO cells transiently co-expressing GFP-tubbyCT and free RFP (control), Nir2-mcherry, Nir3-mcherry and Nir2 S164A-mcherry, respectively. Imaging was performed by Lea Schultz, data anlysis was done by Veronika Thallmair. (**A**) Example images under resting conditions. Scale bar = 5 µm. (**B**) TubbyCT cluster area (mean ± SEM) under resting conditions from cells exemplary shown in (A). Control: n = 20 cells; + Nir2: n = 15 cells; + Nir3: n = 21 cells; + Nir2 S164A: n = 17 cells. (**C**) Time courses (mean ± SEM) of normalized PM RFP/mcherry fluorescence upon activation of PLCβ. (**D**) GFP-tubbyCT cluster dynamics upon activation of PLCβ. Mean ± SEM of normalized traces are shown. (**E**) Normalized tubbyCT cluster TIRF signal at t = 120 sec. Control: n = 22 cells; + Nir2: n = 21 cells; + Nir3: n = 24 cells; + Nir2 S164A: n = 20 cells.

The experiments shown in Figure 3.19 were planned by myself and realized under my supervision by the student assistant Lea Schultz. Data analysis was performed by me. Although all Nir constructs were expressed and also robustly recruited to ER-PM junctions following PLCβ activation (Figure 3.19 C), none of them changed tubbyCT

cluster formation (Figure 3.19 A, B) and cluster recruitment (Figure 3.19 D, E). These results were surprising as $PI(4,5)P_2$ synthesis depends on Nir-mediated PI transfer. However, high native Nir2/3 expression in CHO cells could explain the lack of effect of Nir2/3 over-expression. Nevertheless, if this is the case, over-expression of dominant-negative Nir2 S164A should have reduced tubbyCT clustering and recruitment to ER-PM junctions. Thus, in order to draw conclusions from this experiments other dominant-negative Nir2 mutations should be tested. Moreover, the experiment should be additionally performed in COS-7 cells where native Nir2 and Nir3 expression is lower.

3.11 Localization of tubby-like proteins to E-Syt3-rich ER-PM junctions

So far, I studied the localization and behavior of the $PI(4,5)P_2$ sensor tubbyCT which comprises the GFP-tagged C-terminal tubby domain of the tubby protein, only. Next, I investigated whether localization to ER-PM junctions, as well as its PLC-related dynamics were retained in the full-length tubby protein (tubbyFL). Moreover, since tubby is the founding member of the tubby-like protein family (TULPs), I also examined the localization and dynamics of the related TULP-family protein TULP3.

CHO cells were transiently transfected with GFP-tagged tubbyCT, tubbyFL or TULP3. Cells were imaged by TIRF microscopy and protein clustering as well as PLCβ-induced dynamics were determined.

TubbyFL as well as TULP3 showed a pronounced cluster formation under resting conditions which did not differ from tubbyCT clustering in terms of cluster area and cluster size (Figure 3.20A-C). Moreover, activation of PLCβ caused further recruitment of tubbyFL to its clusters and simultaneous depletion from the non-clustered PM regions (Figure 3.20D). In contrast, TULP3 was depleted both from its clusters and from homogeneously labeled PM regions to a similar degree (Figure 3.20E). Given that the distribution and dynamics of tubbyFL fully replicated the behavior of the C-terminal fragment, namely inverse dynamics in clustered versus the non-clustered PM regions, tubbyFL most likely localized to the same E-Syt3-rich ER-PM junctions occupied by tubbyCT. In contrast, the distinct dynamic behavior of TULP3 at its clusters raised the question whether the TULP3 clusters represent E-Syt3-rich ER-PM junctions as well.

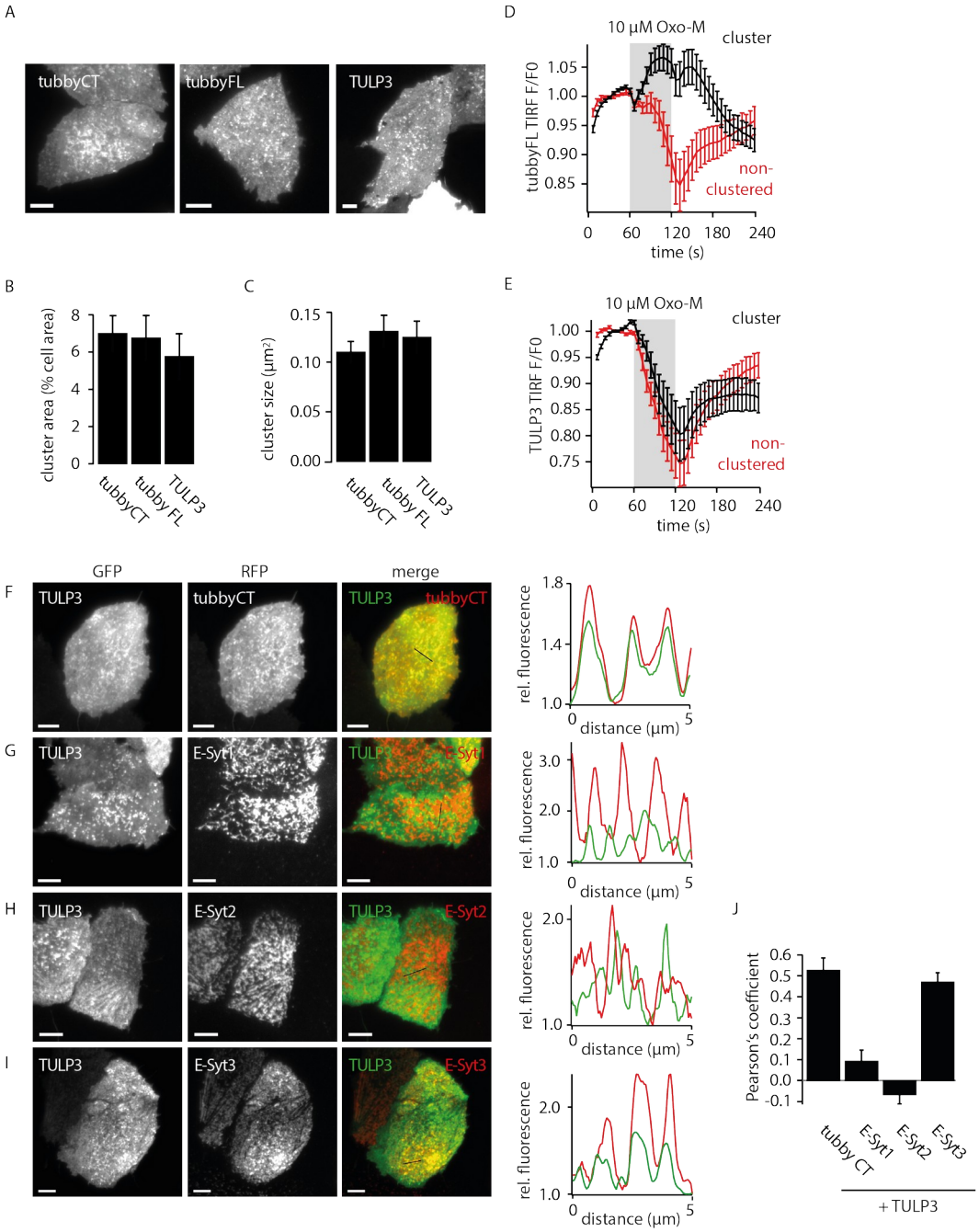

Figure 3.20: Tubby full-length and TULP3 localization and dynamics
(**A**) Example TIRF images of CHO cells expressing GFP-tagged tubbyCT, tubby full-length (tubbyFL) and TULP3, respectively. Scale bar = 5 µm. (**B, C**) Quantification of cluster area (B) and cluster size (C) from cells exemplary shown in (A). Mean ± SEM are plotted. TubbyCT: n = 37 cells; TubbyFL: n = 16 cells; TULP3: n = 17 cells. (**D, E**) TIRF imaging of CHO cells expressing GFP-tubbyFL (D) and GFP-TULP3 (E), respectively. PLCβ-induced GFP dynamics in the clustered and non-clustered PM regions. Mean ± SEM of normalized traces are plotted. (D) n = 15 cells. (E) n = 16 cells. (**F-I**) Example TIRF images of CHO cells co-expressing GFP-TULP3 and RFP-tagged tubbyCT (F), E-Syt1 (G), E-Syt2 (H) and E-Syt3 (I), respectively. Scale bar = 5 µm. In the first column GFP images are shown, followed by RFP and merged images. Line profiles along a distance of 5 µm are depicted on the right. RFP and GFP fluorescence is normalized to respective minimal values. In merged images and line profiles TULP3 is plotted in green and RFP-tagged proteins in red. (**J**) Pearson's coefficients from co-

localization experiments shown exemplary in (F-I). Mean ± SEM are plotted. TULP3 + tubbyCT: n = 23 cells. + E-Syt1: n = 16 cells. + E-Syt2: n = 28 cells. + E-Syt3: n = 27 cells.

To this end, I investigated co-localization of TULP3 with tubbyCT and E-Syt1-3. CHO cells were co-transfected with GFP-TULP3 and RFP-tagged tubbyCT and E-Syt1-3, respectively. Resting RFP and GFP fluorescence was imaged by TIRF microscopy and co-localization of TULP3 with RFP-tagged proteins was analyzed by means of line profiles and Pearson's coefficients (Figure 3.20F-J). TULP3 clearly co-localized with tubbyCT as well as with E-Syt3 (Figure 3.20F, I, J). In contrast, no co-localization between TULP3 and E-Syt1/2 was observed as line profiles do not show overlying peaks and respective Pearson's coefficients range around zero (Figure 3.20G, H, J).
This experiment clarifies that the localization of tubby to E-Syt3-rich ER-PM junctions also holds true for TULP3. The conserved localization of TULP family proteins to ER-PM contact sites raises the question of their putative junctional functions. So far, TULP function is mainly related to primary cilia where they are crucial adapter proteins for GPCR delivery (Mukhopadhyay *et al.*, 2010; Badgandhi *et al.*, 2017). In a first attempt to address junctional function of tubby, I investigated the effect of tubbyCT and tubbyFL over-expression on E-Syt dynamics.

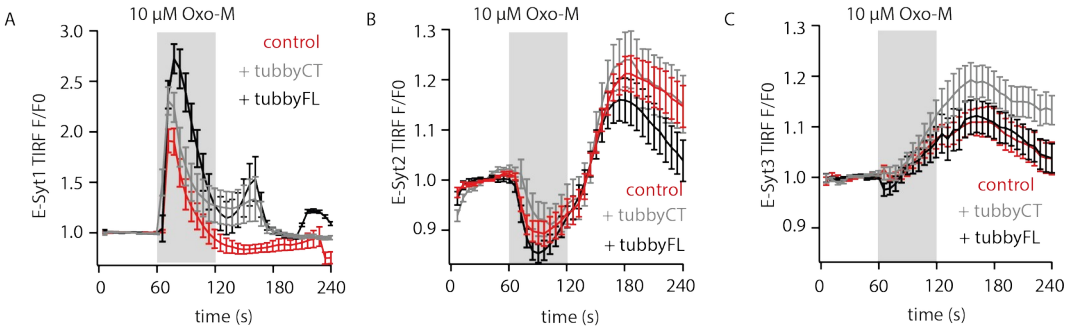

Figure 3.21: Influence of tubby over-expression on PLCβ-induced E-Syt dynamics
(**A-C**) TIRF imaging of CHO cells expressing RFP-tagged E-Syt1 (A), E-Syt2 (B) and E-Syt3 (C) together with free GFP, GFP-tubbyCT and GFP-tubby full-length (tubbyFL), respectively. Normalized E-Syt dynamics (mean ± SEM) upon activation of PLCβ are plotted. (A) E-Syt1 + free GFP: n = 19 cells; + tubbyCT: n = 12 cells; + tubbyFL: n = 13 cells. (B) E-Syt2 + free GFP: n = 24 cells; + tubbyCT: n = 16 cells; + tubbyFL: n = 18 cells. (C) E-Syt3 + free GFP: n = 19 cells; + tubbyCT: n = 17 cells; + tubbyFL: n = 14 cells.

CHO cells were transiently co-transfected with RFP-tagged E-Syts and GFP-tagged tubbyCT and tubbyFL, respectively. RFP-E-Syt dynamics upon PLCβ activation were subsequently measured as a proxy for ER-PM function. As a control, RFP-E-Syt dynamics in presence of free GFP were determined. As shown in Figure 3.21A over-

expression of tubbyCT and tubbyFL increased E-Syt1 recruitment to ER-PM junctions. In contrast, E-Syt2 dynamics were not affected by tubbyCT or tubbyFL over-expression (Figure 3.21B). E-Syt3 recruitment to ER-PM contact sites was slightly increased in presence of tubbyCT, but not tubbyFL (Figure 3.21C). Consequently, tubby might alter E-Syt dynamics following activation of PLCβ.

4 Discussion

4.1 Functionally distinct and spatially separated PI(4,5)P_2 pools

In the present work, I identified the preferential targeting of the PI(4,5)P_2 sensor tubbyCT to ER-PM junctions. This association was mediated by coincidence detection of PI(4,5)P_2 and the ER-PM tethering protein E-Syt3 and allowed for the first time imaging of PLCβ-induced PI(4,5)P_2 synthesis at ER-PM contact sites. Moreover, as tubbyCT labeled also the bulk membrane, this sensor permitted simultaneous imaging of PI(4,5)P_2 depletion outside the ER-PM junctions. Hence, by use of tubbyCT, I could demonstrate the existence of metabolically distinct PI(4,5)P_2 pools. The lateral segregation of PI(4,5)P_2 into functionally distinct lipid subpopulations has been highly discussed as a prerequisite of its multifunctionality (Hammond, 2016). Indeed, superresolution microscopy revealed inhomogeneous distribution of PI(4,5)P_2 across the PM and its clustering into nanodomains of ~ 65-70 nm in size (van den Bogaart *et al*., 2012; Wang and Richards, 2012). Van den Boogart *et al*. (2012) found that lipid clustering was independent of cholesterol and rather depended on interaction with a polybasic amino acid stretch in syntaxin-1A. However, PI(4,5)P_2 is also enriched in cholesterol-rich 'lipid rafts' (Hope and Pike, 1996; Pike and Miller, 1998). But as super-resolution imaging is performed on fixed cells and the study of 'lipid rafts' involves membrane disrupting detergents, observed PI(4,5)P_2 clustering in these experiments might be artificially evoked. Consequently, the physiological relevance of described findings is under discussion, especially as the experimental prove of different PI(4,5)P_2 pools in living cells is rare. Nevertheless, in T cells, depletion of 'non-raft' PI(4,5)P_2 induced filopodia formation and cell spreading, whereas depletion of a 'raft' associated PI(4,5)P_2 pool generated smooth T cells of strikingly different morphology (Johnson and Rodgers, 2008). This clearly argues for the existence of spatially separated and functionally distinct PI(4,5)P_2 pools. Such pools might be generated, as in this example, by accumulation of PI(4,5)P_2 within the 'lipid raft' fraction, but also sequestration of PI(4,5)P_2 via electrostatic interaction with polybasic amino acid stretches like e.g. within the natively unfolded MARCKS proteins are considered to participate in PI(4,5)P_2 clustering (Denisov *et al.*, 1998; reviewed in McLaughlin and Murray, 2005). Moreover, locally defined PI(4,5)P_2 synthesis might contribute to the generation of

various PI(4,5)P_2 pools and individual PIP5Ks were related to specific PI(4,5)P_2 functions (reviewed in van den Bout and Divecha, 2009; reviewed in Kwiatkowska, 2010). In my thesis, I provide for the first time direct evidence for the existence of a PI(4,5)P_2 pool located at ER-PM junctions. Moreover, my data suggests that this pool is generated by the local production of PI(4,5)P_2 at the site of PI transfer.

4.2 Local synthesis of PI(4,5)P_2 at ER-PM junctions

PI(4,5)P_2 synthesis crucially depends on the PI transfer from the ER to the PM (reviewed in Pemberton, Kim and Balla, 2020). This transfer is mainly mediated by the activity of Nir2/3 which localize to E-Syt containing ER-PM contact sites (Chang *et al*., 2013; Kim *et al*., 2013; Chang and Liou, 2015; Kim *et al*., 2015). Ensuing PI (and PI4P) phosphorylation to generate PI(4,5)P_2 might occur directly at ER-PM junctions, however PI (or PI4P) diffusion into the bulk membrane and subsequent phosphorylation within the entire membrane is also possible. This question has never been addressed experimentally, probably due to the lack of an appropriate PI(4,5)P_2 reporter. With tubbyCT, I now provide a PI(4,5)P_2 sensor with which junctional PI(4,5)P_2 dynamics can be measured. Moreover, as tubbyCT also labels the bulk PM, bulk PI(4,5)P_2 levels can be analyzed at the same time. By use of tubbyCT, I identified PLCβ-induced local PI(4,5)P_2 production at E-Syt3-containing ER-PM junctions during simultaneous global PI(4,5)P_2 consumption.

For such spatially confined PI phosphorylation, ER-PM junctions need to be equipped with PI4 and PI4P5 kinases. PI4KIIIα accounts for the majority of PM PI4P production in mammalian model cells (Balla *et al*., 2005; Balla *et al*., 2008; Nakatsu *et al*., 2012; Bojjireddi *et al*., 2014). It forms a complex with TTC7, FAM126A and EFR3 (Nakatsu *et al*., 2012; Baskin *et al*., 2016) or alternatively with TMEM150 and EFR3 (Chung *et al.*, 2015b). Localization of PI4KIIIα (or any of its complex components) to ER-PM junctions has never been shown, but its homologue in yeast Stt4 localizes to 'PI kinase patches' at the PM (Baird *et al.*, 2008) which might represent ER-PM contact sites in mammalian cells (Nakatsu *et al*., 2012). Indeed, Stt4 comprises a FFAT motif which mediates binding to the ER-resident VAP-A/B homologues Scs2/22 (Nakatsu *et al.*, 2012; Stefan *et al.*, 2011). The Stt4 FFAT motif is partially conserved in mammalian PI4KIIIα (Nakatsu *et al*., 2012), however, binding of the latter to VAP-A/B has not been explored. However, together with the PM binding of the PI4KIIIα interaction partner

EFR3 (Nakatsu *et al*., 2012), ER anchoring of PI4KIIIα complex would result in its localization to ER-PM junctions.

PI4P 5-kinases occur in three isoforms, PIP5Kα-γ, and several splice variants exist of each of them. Endogenous PIP5K isoforms and respective splice variants show unique subcellular distributions and are thought to specifically generate individual $PI(4,5)P_2$ pools (Loijens and Anderson, 1996; Ishihara *et al.*, 1996; Ishihara *et al.*, 1998; reviewed in van den Bout and Divecha, 2009; reviewed in Pemberton, Kim and Balla, 2020). Moreover, (auto)phosphorylation modulates PIP5K activity and confers additional complexity to $PI(4,5)P_2$ production (Itoh *et al.*, 2000; Park, Itoh and Takenawa, 2001; Di Paolo *et al.*, 2002; Ling *et al.*, 2002). However, to the best of my knowledge, association with ER-PM junctions has never been assigned to any of the PIP5K variants. Still, $PI(4,5)P_2$ but no PI4P accumulation at tubbyCT-labeled ER-PM contact sites indicates immediate PI4P phosphorylation to $PI(4,5)P_2$. Indeed, metabolic channeling has emerged as important mechanism to enhance efficiency in multienzymatic reactions. Generation of $PI(3,4,5)P_3$ for example occurs in a multienzymatic complex comprising all involved enzymes, i.e. PI4KIIIα, PIP5Kα and PI3K. Kinase assembly and the integration of the individual phosphorylation steps is achieved by the scaffolding protein IQGAP1 (Choi *et al.*, 2016). My data suggest a similar scaffolding of $PI(4,5)P_2$ production at ER-PM junctions. According to this model, transferred PI would be immediately used for PI4P and subsequent $PI(4,5)P_2$ generation. Notably, the model is also in line with unexpectedly low PM PI levels discovered only recently (Pemberton *et al*., 2020; Zewe *et al*., 2020) and the lack of PI4P build-up at ER-PM contact sites. Interestingly, PIP5Ks are activated by PA (Moritz *et al*., 1992; Jenkins, Fisette and Anderson, 1994; Ishihara *et al*., 1996; Ishihara *et al*., 1998; Jarquin-Pardo *et al*., 2007), which is generated during PLCβ signaling. PI4KIIIα might be similarly up-regulated by a PLCβ derived messenger, e.g. via Ca^{2+}, as PI4K has been suggested to be activated by the neuronal calcium sensor NCS-1 (Gamper *et al.*, 2004; Delmas *et al.*, 2005; Winks *et al.*, 2005). However, locally defined educt accumulation might also drive the individual phosphorylation steps. The hypothesis of metabolic phosphoinositide channeling for $PI(4,5)P_2$ production fits well to the observation that the majority of (detectable) PI4P in the (bulk) PM is not used for $PI(4,5)P_2$ synthesis (Hammond, Schiavo and Irvine, 2009; Hammond *et al*., 2012;

Bojjireddi *et al*., 2014). PI4KIIIα inhibition by GSK-A1 did not affect basal PI(4,5)P_2 levels (Bojjireddi *et al*., 2014), however, incubation of cells in GSK-A1 reduced basal tubbyCT clustering. This suggests that the junctional PI(4,5)P_2 pool depends on continuous PI phosphorylation by PI4KIIIα and is indeed metabolically distinct from PI(4,5)P_2 in the bulk membrane.

4.3 PI(4,5)P_2 content at ER-PM junctions

Without restriction of its lateral diffusion, PI(4,5)P_2 distributes rapidly across the membrane and thus local synthesis not necessarily generates domains with high PI(4,5)P_2 levels (Golebiewska *et al.*, 2008; reviewed in Kwiatkowska, 2010; Golebiewska *et al.*, 2011). However, there is evidence that the lateral mobility of PI(4,5)P_2 is delimited in the inner leaflet when compared to its diffusion in the outer leaflet, but also when compared to the mobility of other lipids (Golebiewska *et al*., 2008). Molecular barriers, like e.g. formed by septins might restrict PI(4,5)P_2 diffusion (Golebiewska *et al*., 2011; reviewed in Trimble and Grinstein, 2015). Alternatively, PI(4,5)P_2 might also be sequestered by PI(4,5)P_2 binding proteins (Denisov *et al*., 1998; reviewed in McLaughlin and Murray, 2005). Likewise, my data suggest local PI(4,5)P_2 enrichment at ER-PM contact sites during activation of PLCβ, but also under resting conditions. TubbyCT cluster were not easily abrogated by over-expression of E-Syt3 truncation mutants, that lack the ER-binding hairpin and therefore homogeneously distribute across the PM. vice versa, these E-Syt3 deletion constructs were rather recruited into tubbyCT cluster. Of note, this high affinity of tubbyCT to ER-PM junctions could also derive from binding to native E-Syt3. However, coarse-grained molecular dynamics simulations recently revealed a second PI(4,5)P_2 binding site in tubbyCT which is parallel oriented to its conservative binding pocket and thus allows simultaneous binding of two PI(4,5)P_2 molecules. Even beyond that, stable PM targeting of tubbyCT requires occupancy of both binding pockets (Thallmair *et al*., 2020a). This dual binding mode explains the disproportionate accumulation of tubbyCT at PI(4,5)P_2-rich domains (Thallmair *et al*., 2020b). Consistently, PLCδ1-PH, which only holds one PI(4,5)P_2 binding site, was only slightly enriched at tubbyCT-labeled ER-PM junctions.

Moreover, tubbyCT sequesters approximately four PI(4,5)P_2 molecules in its vicinity (Thallmair *et al*., 2020a), hence the recruitment of tubbyCT to ER-PM junctions might

positively influence their $PI(4,5)P_2$ content. Interestingly, divalent cations are also known to sequester $PI(4,5)P_2$ (Levental *et al.*, 2009), thus increased Ca^{2+} levels during PLCβ signaling might additionally stabilize $PI(4,5)P_2$-rich domains at ER-PM junctions. Such $PI(4,5)P_2$-enriched microdomains at ER-PM junctions have been proposed before (Maléth *et al.*, 2014), however, to the best of my knowledge, we provide the first direct evidence for their existence.

4.4 Function of junctional $PI(4,5)P_2$ pools

The $PI(4,5)P_2$ sensor tubbyCT preferentially detects a $PI(4,5)P_2$ pool at ER-PM junctions. This pool is replenished during PLCβ activation and thus during global $PI(4,5)P_2$ depletion. Moreover, my data suggest $PI(4,5)P_2$ enrichment at ER-PM junctions also under resting conditions. As explained below, an obvious function of this junctional $PI(4,5)P_2$ pool would be to establish and maintain the connection from the ER to the PM via binding of ER-PM tether proteins. Typically, ER-PM tethers are ER-resident proteins which bind the PM in trans (Giordano *et al*., 2013; Chung *et al*., 2015a; Besprozvannaya *et al*., 2018). In case of the E-Syt proteins, PM association is mediated via $PI(4,5)P_2$ binding of their C-terminal C2 domains (Giordano *et al*., 2013). Binding of E-Syt1 to $PI(4,5)P_2$ is Ca^{2+}-dependent, and Ca^{2+} is therefore considered as the signal that mediate tightening of ER-PM contact sites during PLCβ signaling (Giordano *et al*., 2013; Chang *et al*., 2013; Fernández-Busnadiego *et al*., 2015). However, activation of PLCβ depletes bulk $PI(4,5)P_2$, which predicts that without independent regulation of the junctional $PI(4,5)P_2$ levels, ER-PM connectivity would be rapidly lost, despite increasing Ca^{2+} levels. As ER-PM junctions are known to be essential for providing the $PI(4,5)P_2$ precursor PI to the PM, such loss of integrity would result in impaired $PI(4,5)P_2$ replenishment. Hence, increasing junctional $PI(4,5)P_2$ levels may be necessary to secure $PI(4,5)P_2$ recovery following massive loss of bulk $PI(4,5)P_2$ due to activation of PLCβ. Consistently, the disturbance of junctional $PI(4,5)P_2$ dynamics by incubation of the cells in the PI4K inhibitor GSK-A1, resulted in reduced ER-PM connectivity following activation of PLCβ. Due to the specific enrichment of tubbyCT at E-Syt3-containing ER-PM junctions, my current data reveal the increase in junctional $PI(4,5)P_2$ only for contact sites comprising E-Syt3. However, as PI4K inhibition also affected E-Syt1/2 dynamics, I hypothesize that $PI(4,5)P_2$ synthesis is a more general feature of ER-PM contact sites and also applies for other subtypes,

especially for those comprising E-Syt1 and E-Syt2. It might also hold true for STIM1-Orai-tethered junctions, as phosphoinositides including PI(4,5)P_2 play an important role during store-operated Ca^{2+} entry (SOCE) (Walsh *et al.*, 2010). Following Ca^{2+} store depletion e.g. due to activation of PLCβ, SOCE leads to the refilling of internal Ca^{2+} stores (Zhang *et al*., 2005; Luik *et al*., 2006; Orci *et al.*, 2009). In this process, the Ca^{2+} sensor STIM1 translocates to ER-PM junctions in a phosphoinositide dependent manner where it then interacts and activates the Ca^{2+} channel Orai1 (Zhang *et al*., 2005; Luik *et al*., 2006; Walsh *et al*., 2010). Again, depletion of junctional PI(4,5)P_2 via PLCβ would impair this mechanism needed for Ca^{2+} homeostasis and ongoing receptor activation. Indeed, inhibition of PI4K impairs STIM1 recruitment and SOCE (Walsh *et al*., 2010), arguing for PLCβ-induced replenishment of the PI(4,5)P_2 pool at STIM1-containing ER-PM junctions.

4.5 Existence of different types of E-Syt-tethered ER-PM junctions

My work points to the existence of different types of E-Syt-tethered ER-PM contact sites. TubbyCT enrichment occurs specifically at those junctions containing E-Syt3. Its specific interaction with E-Syt3 was substantiated consistently by co-localization experiments, co-immunoprecipitations and by recruitment of E-Syt3ΔHP, but not E-Syt1ΔHP and E-Syt2ΔHP into ER-PM contact sites. Nevertheless, E-Syt proteins are known to form heterodimers (Schauder *et al*., 2014, Giordano *et al*., 2015, Tremblay *et al*., 2015, Idevall-Hagren *et al*., 2015) and consistently, (over-expressed) E-Syt3 recruited E-Syt1/2 into tubbyCT containing ER-PM junctions. Moreover, over-expression of E-Syt1 altered E-Syt2/3 dynamics in such way that a transient PM recruitment following PLCβ activation was observed. However, individual E-Syt isoforms exhibited different PLCβ-induced dynamics. Although the particular behavior of E-Syt1 may be partially explained by the Ca^{2+}-dependence of its PM association (Giordano *et al*., 2013, Chang *et al*., 2013; Bian, Saheki and De Camilli, 2018), the observed contrast between dissociation of E-Syt2 and recruitment of E-Syt3 is not. Since PM binding of both E-Syt proteins should solely depend on PI(4,5)P_2 (Giordano *et al*., 2013), opposite dynamics strongly point towards localization predominantly at different subtypes of ER-PM junctions. Notably, inverse behavior of E-Syt2 and E-Syt3 following PLCβ activation was observed before (Dickson *et al*., 2016). Interestingly, Dickson *et al*. (2016) discovered co-localization of E-Syt2 with Sac1, an ER-resident

phosphatase which dephosphorylates PI4P and thereby also affects PM PI(4,5)P_2 levels. Reduction in E-Syt2-mediated ER-PM connectivity (most likely induced by a drop in associated junctional PI(4,5)P_2 levels), impairs access of Sac1 to the PM and thereby promotes PI(4,5)P_2 recovery following PLCβ activation (Dickson *et al*., 2016). My data now revealed that at E-Syt3-mediated ER-PM junctions, PI(4,5)P_2 levels increase upon PLCβ activation, resulting in slight E-Syt3 recruitment. Hence, opposite E-Syt and most likely also opposite PI(4,5)P_2 dynamics at two subtypes of ER-PM junctions may have a synergistic role in supporting PI(4,5)P_2 replenishment following PLCβ activation.

4.6 Cell type-dependent junctional recruitment of tubbyCT

TubbyCT localizes to ER-PM junctions by coincidence detection of PI(4,5)P_2 and E-Syt3, but the portion of junctional tubbyCT depends on the cell type under investigation. In CHO cells, strong junctional localization was observed, whereas in COS-7 cells tubbyCT distributed homogeneously across the PM. Missing junctional recruitment might be explained by low E-Syt3 expression, low junctional PI(4,5)P_2 levels, or a different architecture of the ER-PM contact sites. Because in COS-7 cells, tubbyCT was recruited to ER-PM junctions by ectopic over-expression of E-Syt3, I propose that endogenous E-Syt3 levels are too low for tubbyCT junctional association. Indeed, in COS-7 cells, E-Syt3 expression was lower than E-Syt1 and E-Syt2 expression, although E-Syt3 mRNA could be robustly detected. Unexpectedly, my experiments failed to detect E-Syt3 mRNA in CHO cells, which might be due to technical reasons as available sequence information for E-Syt3 of *Cricetulus griseus* was limited to a predicted sequence (XM_027436637.2). Additional careful experiments to analyze E-Syt3 expression in CHO cells will be required to resolve this issue.

In my work, I could show that in CHO cells, PI(4,5)P_2 is enriched at E-Syt3-containing ER-PM junctions. High PI(4,5)P_2 content can be established by high expression of Nir proteins or PI and PI4P kinases or by reduced diffusion of PI(4,5)P_2 molecules. Indeed, in CHO cells Nir2 and Nir3 expression is elevated compared to COS-7 cells. Nir3 maintains basal PI(4,5)P_2 concentrations (Chang and Liou, 2015) and its high expression might result in local enrichment in PI(4,5)P_2 under resting conditions. In contrast, Nir2 activity restores PI(4,5)P_2 levels following strong Gq-coupled receptor stimulation (Chang and Liou, 2015). Together, low Nir2 and Nir3 expression in COS-7 cells can result in low basal junctional PI(4,5)P_2 levels as well as altered PI(4,5)P_2

dynamics following activation of PLCβ. Indeed, besides tubbyCT, over-expressed E Syt3 showed pronounced dissociation from ER-PM junctions in COS-7 cells, which directly argues for different PI(4,5)P_2 dynamics compared to CHO cells. Differential junctional PI(4,5)P_2 content could also result from different lateral diffusion speed of PI(4,5)P_2. Septin4 and Septin5 have been proposed as diffusion barriers at ER-PM junctions (Sharma *et al*., 2013). However, as their mRNA levels in COS-7 cells exceeded the levels in CHO cells, their expression does not obviously explain the observed differences in tubbyCT localization. Nevertheless, I cannot exclude that PI(4,5)P_2 diffusion in COS-7 is faster than in CHO cells.

4.7 TubbyCT as junctional PI(4,5)P_2 pool-specific sensor

PLCδ1-PH is the most commonly used PI(4,5)P_2 sensor, but its use is compromised by its high I(1,4,5)P_3 affinity (Cifuentes, Delaney and Rebecchi, 1994; Garcia *et al*., 1995; Lemmon *et al*., 1995). Hence, its dissociation from the PM following PLCβ activation might be caused by a reduction in PM PI(4,5)P_2, an increase in I(1,4,5)P_3 concentration or a combination of both. TubbyCT lacks I(1,4,5)P_3 binding (Quinn, Behe and Tinker, 2008; Szentpetery *et al*., 2009) and thus might report PM PI(4,5)P_2 changes more accurately than PLCδ1-PH. However, despite its lower PI(4,5)P_2 affinity (Halaszovich, Schreiber and Oliver, 2009; Thallmair *et al*., 2020a), tubbyCT fails to dissociate reliably from the PM following PLCβ activation (Quinn, Behe and Tinker, 2008; Szentpetery *et al*., 2009), a characteristic which limited its application. In my work, I discovered its preferential localization at E-Syt3-rich ER-PM junctions. As it also labels the bulk membrane, it allows simultaneous imaging of junctional and bulk PI(4,5)P_2 dynamics. During PLCβ signaling and hence during global PI(4,5)P_2 consumption, PI(4,5)P_2 levels increase at tubbyCT-labeled ER-PM contact sites. Consequently, net tubbyCT dynamics, measured across the entire PM, depend on the respective PI(4,5)P_2 pool dynamics, but also on the portion of tubbyCT bound to ER-PM junctions. This portion depends on the cell type under investigation, which might explain different net tubbyCT dynamics in different cell types and tissues (Quinn, Behe and Tinker, 2008; Szentpetery *et al*., 2009; Hackelberg and Oliver, 2018). Nevertheless, tubbyCT provides a so far unique possibility to study junctional PI(4,5)P_2 dynamics. However, for dissecting them from the dynamics in the bulk membrane, tubbyCT cluster need to be detected and analyzed independently from the bulk membrane. As cluster detection is challenging in cell types

with low cluster density, tubbyCT usage as junctional PI(4,5)P_2 sensor is restricted to cell types with pronounced tubbyCT clustering. Besides E-Syt-mediated enrichment at ER-PM contact sites, unique PI(4,5)P_2 binding properties additionally contribute to the suitability as a sensor for junctional PI(4,5)P_2 dynamics. Molecular dynamics simulations recently revealed a second PI(4,5)P_2 binding site, in addition to the well studied conventional binding pocket. For stable PM binding, both binding sites need to be occupied by PI(4,5)P_2 molecules, which explains its accumulation at PI(4,5)P_2-rich membrane domains (Thallmair *et al*., 2020a). Moreover, the moderate PI(4,5)P_2 affinity favors translocation from PI(4,5)P_2-depleted PM regions to domains with ongoing PI(4,5)P_2 synthesis. PLCδ1-PH lacks this dual PI(4,5)P_2 binding properties (Thallmair *et al*., 2020a) which may contribute to its only weak accumulation at tubbyCT-labeled ER-PM junctions with high PI(4,5)P_2 content. However, PI(4,5)P_2 binding properties do not explain the observed dissociation of PLCδ1-PH and also Epsin1 ENTH domain from tubbyCT clusters and hence from sites with rising PI(4,5)P_2 levels. In case of PLCδ1-PH, this translocation may reflect binding to cytosolic I(1,4,5)P_3. However, this does not account for Epsin1 ENTH domain, which lacks I(1,4,5)P_3 affinity (Leitner *et al*., 2019). A highly speculative explanation for PLCδ1-PH and ENTH dissociation from ER-PM contact sites during PLCβ activation is a hypothetical initial transient drop in PI(4,5)P_2 levels. It seems reasonable that PI(4,5)P_2 resynthesis kicks in slightly delayed to its hydrolysis and thus (assuming PLCβ accessibility to ER-PM contact sites) junctional PI(4,5)P_2 levels should also drop transiently. TubbyCT may fail to report such initial PI(4,5)P_2 depletion due to binding to E-Syt3, whereas such a transient may be sufficient to displace PLCδ1-PH and ENTH from ER-PM junctions.

When using tubbyCT as a sensor for PI(4,5)P_2 levels at ER-PM junctions, one should keep in mind, that molecular dynamics simulations recently revealed sequestration of PI(4,5)P_2 molecules by tubbyCT (Thallmair *et al*., 2020a). Hence, recruitment of tubbyCT to ER-PM contact sites might positively influence local PI(4,5)P_2 accumulation. Indeed, tubby over-expression moderately altered E-Syt dynamics. Consequently, dynamics of over-expressed tubbyCT might slightly over-estimate PI(4,5)P_2 synthesis under native conditions.

In general, pool-specific PI(4,5)P_2 sensors are rare, but important tools to study PI(4,5)P_2 multifunctionality. Domain-selective sensors have also been engineered by

fusion of PI(4,5)P_2 binding domains to proteins or domains that bias cellular localization, resulting in coincidence detection very much like the properties of tubbyCT discovered here. E.g. the fusion of auxilin to PLCδ1-PH produced a sensor which specifically reports PI(4,5)P_2 dynamics from endocytic clathrin-associated structures (He *et al*., 2017). But also common PI(4,5)P_2 binding domains may – like tubbyCT – preferentially detect a specific lipid subpopulation.

4.8 Function of tubby and TULPs at ER-PM junctions

Consistent with the localization of its C-terminal domain, full-length tubby is enriched at E-Syt3-rich ER-PM junctions. Moreover, it also dissociates from the bulk membrane and further accumulates at ER-PM contact sites during stimulation of Gq/11-coupled receptors. Tubby is the founder member of the family of tubby-like proteins (TULPs) and its resting localization to E-Syt3-rich ER-PM junctions also applies to its closest relative, TULP3. However, in contrast to tubby, TULP3 dissociates from ER-PM contact sites during activation of PLCβ. Like tubby, the C-terminal domain of TULP3 holds the recently identified second PI(4,5)P_2 binding site (Thallmair *et al*., 2020a), which explains its accumulation at regions with high PI(4,5)P_2 content. Moreover, its specific co-localization with E-Syt3 suggests coincidence detection of this ER-PM tether protein. Dissociation of TULP3 from ER-PM contact sites during PLCβ activation may reflect different E-Syt3 or PI(4,5)P_2 binding affinities. Together with a hypothetical initial brief decrease in junctional PI(4,5)P_2 levels (see also 4.7), this may explain junctional TULP3 dynamics. However, dissociation of TULP3 might also reflect its binding to another protein or lipid, maybe in a Ca^{2+}-dependent manner.

TULP family proteins deliver G protein-coupled receptors (GPCRs) to primary cilia (Mukhopadhyay *et al*., 2010; Sun *et al*., 2012; Loktev and Jackson, 2013; Badgandi *et al*., 2017). Interestingly, all GPCRs provided to primary cilia by tubby, like the somatostatin receptor subtype 3 (Sstr3), Melanin-concentrating hormone receptor 1 (Mchr1) and the neuropeptide Y receptor NPY2R, are linked to obesity syndromes (Chen *et al*., 2002; Davenport *et al*., 2007; Wang *et al*., 2009; Loktev and Jackson, 2013). Hence, the late-onset obesity observed in tubby-deficient mice can be explained by impaired ciliary functions (Coleman and Eicher, 1990; Stubdal *et al*., 2000). In contrast, the function of TULPs at E-Syt3-rich ER-PM junctions remains elusive. Interestingly, E-Syt3 has been recently shown to promote food intake and glucose

intolerance in hypothalamic proopiomelanocortin (POMC)-expressing neurons (Zhang *et al.*, 2020). E-Syt3 knock-out mice showed increased processing of POMC to α-MSH, a neuropeptide which is known to negatively shift energy balance. Moreover, E-Syt3 produced ER stress, which in turn prevents POMC processing and thus promotes obesity (Zhang *et al*., 2020). In the end, Zhang *et al.* (2020) attribute the anti-obesity phenotype in E-Syt3 knock-out mice to increased DAG levels (Saheki *et al*., 2016) and hence increased PKC activity (Zhang *et al*., 2020). However, as tubby prevents obesity, E-Syt3 might additionally sequester tubby at ER-PM junctions and prevent GPCR delivery to primary cilia.

Moreover, TULP proteins might contribute to $PI(4,5)P_2$ enrichment at ER-PM contact sites by limiting its lateral diffusion, as molecular dynamics simulations revealed sequestering of $PI(4,5)P_2$ molecules by tubbyCT. Recruitment of tubby to ER-PM junctions during PLCβ activation might serve as positive feedback to ensure rising $PI(4,5)P_2$ levels and consequently might positively influence integrity of ER-PM contact sites. Indeed, tubby over-expression moderately increased E-Syt1 and E-Syt3 recruitment to ER-PM junctions during activation of PLCβ.

4.9 Outlook

In my work – by use of the $PI(4,5)P_2$ sensor tubbyCT – I provide for the first time evidence for $PI(4,5)P_2$ synthesis at E-Syt3-rich ER-PM junctions. I could show that $PI(4,5)P_2$, but not PI4P accumulates at the site of PI transfer which suggests metabolic channeling of PI for $PI(4,5)P_2$ production. However, the proposed enzymatic complex comprising PI4KIIIα, PIP5K and a scaffold protein has not been investigated in this work. Its identification and localization will require further investigations.

Moreover, in my thesis, I discovered metabolically distinct $PI(4,5)P_2$ pools. TubbyCT offers the opportunity to simultaneously study a $PI(4,5)P_2$ pool being consumed and a pool being resynthesized during PLCβ signaling. Beyond that, the multifunctionality of $PI(4,5)P_2$ suggests the existence of a multitude of different $PI(4,5)P_2$ pools (reviewed in Di Paolo and De Camilli, 2006). Also the heterogeneity of ER-PM junctions points to separate junctional $PI(4,5)P_2$ dynamics (reviewed in Saheki and De Camilli, 2017). However, selective enrichment of tubbyCT at E-Syt3-rich ER-PM contact sites allowed for examination of this junctional subtype only. Hence, for a better understanding of spatially restricted $PI(4,5)P_2$ dynamics and also of ER-PM junctional biology, more

pool-specific PI(4,5)P_2 sensors are needed. A promising approach therefore is the fusion of a PI(4,5)P_2 binding domain to a protein of known, restricted localization, as previously done successfully in engineering of a endocytosis-specific PI(4,5)P_2 sensor (He *et al*., 2017). To this end, fusion proteins of tubbyCT with different ER-PM tethers may allow for the characterization of PI(4,5)P_2 dynamics from different subtypes of ER-PM junctions in the future.

Finally, I could show that the localization of tubby at E-Syt3-rich ER-PM junctions is conserved among TULP family proteins. This indicates a conserved junctional function of TULPs. Interestingly, E-Syt3 and tubby are highly expressed in the hypothalamus (Zhang *et al*., 2020; Kleyn *et al.*, 1996) were both function in energy balance, albeit in a reverse manner (Zhang *et al*., 2020; Coleman and Eicher, 1990; Stubdal *et al*., 2000). E-Syt3 decreases synthesis of α-MSH via decreased PKC activity and decreased transcription of POMC-processing enzymes PC1/3 and PC2. Moreover, E-Syt3 decreases synthesis of α-MSH by production of ER stress. As α-MSH prevents obesity, E-Syt3 positively shifts the energy balance (Zhang *et al*., 2020). In contrast, tubby protects mice from obesity (Coleman and Eicher, 1990; Stubdal *et al*., 2000), suggesting that tubby negatively regulates the E-Syt3-PKC pathway. The mechanism of such inhibitory action needs to be addressed in further investigations.

5 References

Aikawa, Y., Hara, H. and Watanabe, T. (1997) 'Molecular Cloning and Characterization of Mammalian Homologues of the Drosophila retinal degeneration B Gene', *Biochem Biophys Res Commun.*, 236(3), pp. 559–564.

Aikawa, Y. *et al.* (1999) 'Involvement of PITPnm, a mammalian homologue of Drosophila rdgB, in phosphoinositide synthesis on Golgi membranes', *Journal of Biological Chemistry*, 274(29), pp. 20569–20577. doi: 10.1074/jbc.274.29.20569.

Amarilio, R. *et al.* (2005) 'Differential Regulation of Endoplasmic Reticulum Structure through VAP-Nir Protein Interaction', *Journal of Biological Chemistry*, 280(7), pp. 5934–5944. doi: 10.1074/jbc.M409566200.

Anderie, I., Schulz, I. and Schmid, A. (2007) 'Direct interaction between ER membrane-bound PTP1B and its plasma membrane-anchored targets', *Cellular Signalling*, 19(3), pp. 582–592. doi: 10.1016/j.cellsig.2006.08.007.

Badgandi, H. B. *et al.* (2017) 'Tubby family proteins are adapters for ciliary trafficking of integral membrane proteins', *The Journal of cell biology*, 216(3), pp. 743–760. doi: 10.1083/jcb.201607095.

Baird, D. *et al.* (2008) 'Assembly of the PtdIns 4-kinase Stt4 complex at the plasma membrane requires Ypp1 and Efr3', *Journal of Cell Biology*, 183(6), pp. 1061–1074. doi: 10.1083/jcb.200804003.

Balla, A. *et al.* (2005) 'A Plasma Membrane Pool of Phosphatidylinositol 4- Phosphate Is Generated by Phosphatidylinositol 4-Kinase Type-III Alpha : Studies with the PH Domains of the Oxysterol Binding Protein and FAPP1', *Molecular Biology of the Cell*, 16, pp. 1282–1295. doi: 10.1091/mbc.E04.

Balla, A. *et al.* (2008) 'Maintenance of Hormone-sensitive Phosphoinositide Pools in the Plasma Membrane Requires Phosphatidylinositol 4-Kinase IIIalpha', *Molecular Biology of the Cell*, 19, pp. 711–721. doi: 10.1091/mbc.E07.

Balla, T. (2013) 'Phosphoinositides: tiny lipids with giant impact on cell regulation', *Physiological reviews*, 93(3), pp. 1019–1137. doi: 10.1152/physrev.00028.2012.

Baskin, J. M. *et al.* (2016) 'The leukodystrophy protein FAM126A (hyccin) regulates PtdIns(4)P synthesis at the plasma membrane', *Nature cell biology*, 18(1), pp. 132–8. doi: 10.1038/ncb3271.

Besprozvannaya, M. *et al.* (2018) 'GRAM domain proteins specialize functionally distinct ER-PM contact sites in human cells', *eLife*, 7, p. e31019.

Bian, X., Saheki, Y. and De Camilli, P. (2018) 'Ca2+ releases E-Syt1 autoinhibition to couple ER-plasma membrane tethering with lipid transport', *The EMBO Journal*, 37(2), pp. 219–234. doi: 10.15252/embj.201797359.

van den Bogaart, G. *et al.* (2012) 'Membrane protein sequestering by ionic protein-lipid interactions', *Nature*, 479(7374), pp. 552–555. doi: 10.1016/j.biotechadv.2011.08.021.Secreted.

Bojjireddy, N. *et al.* (2014) 'Pharmacological and Genetic Targeting of the PI4KA Enzyme Reveals Its Important Role in Maintaining Plasma Membrane Phosphatidylinositol 4-Phosphate and Phosphatidylinositol 4,5-Bisphosphate Levels', *The Journal of biological chemistry*, 289(9), pp. 6120–6132. doi: 10.1074/jbc.M113.531426.

van den Bout, I. and Divecha, N. (2009) 'PIP5K-driven PtdIns(4,5)P2 synthesis: regulation and cellular functions', *Journal of Cell Science*, 122(21), pp. 3837–3850. doi: 10.1242/jcs.056127.

Carrasco, S. and Mérida, I. (2007) 'Diacylglycerol, when simplicity becomes complex', *Trends in Biochemical Sciences*, 32(1), pp. 27–36. doi: 10.1016/j.tibs.2006.11.004.

Casares, D., Escribá, P. V. and Rosselló, C. A. (2019) 'Membrane Lipid Composition: Effect on Membrane and Organelle Structure, Function and Compartmentalization and Therapeutic Avenues', *International Journal of Molecular Sciences*, 20(9), p. 2167.

Chang, C.-L. *et al.* (2013) 'Feedback Regulation of Receptor-Induced Ca2+ Signaling Mediated by E-Syt1 and Nir2 at Endoplasmic Reticulum-Plasma Membrane Junctions', *Cell Reports*. The Authors, 5(3), pp. 813–825. doi: 10.1016/j.celrep.2013.09.038.

Chang, C.-L. and Liou, J. (2015) 'Phosphatidylinositol 4,5-Bisphosphate Homeostasis Regulated by Nir2 and Nir3 Proteins at Endoplasmic Reticulum-Plasma Membrane Junctions', *Journal of Biological Chemistry*, 290(23), pp. 14289–14301. doi: 10.1074/jbc.M114.621375.

Chen, Y. *et al.* (2002) 'Targeted Disruption of the Melanin-Concentrating Hormone Receptor-1 Results in Hyperphagia and Resistance to Diet-Induced Obesity', *Endocrinology*, 143(7), pp. 2469–2477.

Choi, S. *et al.* (2016) 'Agonist-stimulated phosphatidylinositol-3,4,5-trisphosphate generation by scaffolded phosphoinositide kinases', *Nature Cell Biology*, 18(12), pp. 1324–1335. doi: 10.1038/ncb3441.

Choy, C. H., Han, B.-K. and Botelho, R. J. (2017) 'Phosphoinositide Diversity, Distribution, and Effector Function: Stepping Out of the Box', *BioEssays*, 39(12), p. 1700121. doi: 10.1002/bies.201700121.

Chung, J. *et al.* (2015a) 'PI4P/phosphatidylserine countertransport at ORP5- and ORP8-mediated ER-plasma membrane contacts', *Science*, 349(6246), pp. 428–432. doi: 10.1126/science.aab1370.

Chung, J. *et al.* (2015b) 'Plasticity of PI4KIIIα interactions at the plasma membrane', *EMBO reports*, 16(3), pp. 312–320. doi: 10.15252/embr.201439151.

Cifuentes, M. E., Delaney, T. and Rebecchi, M. J. (1994) 'D-myo-Inositol 1,4,5-Trisphosphate Inhibits Binding of Phospholipase C-δ1 to Bilayer Membranes', *Journal of Biological*

Chemistry, 269(3), pp. 1945–1948.

Cifuentes, M. E., Honkanen, L. and Rebecchi, M. J. (1993) 'Proteolytic Fragments of Phosphoinositide-specific phospholipase C-δ1. Catalytic and membrane binding properties', *Journal of Biological Chemistry*, 268(16), pp. 11586–11593.

Coleman, D. L. and Eicher, E. M. (1990) 'Fat (fat) and Tubby (tub): Two Autosomal Recessive Mutations Causing Obesity Syndromes in the Mouse', *Journal of Heredity*, 81(6), pp. 424–427. doi: 10.1093/oxfordjournals.jhered.a111019.

Cooper, G.M. (2000) 'Structure of the Plasma Membrane' in ‚The cell, 2nd edition. A molecular approach', Sunderland (MA), Sinauer Associates, ISBN-10: 0-87893-106-6.

Corradi, V. *et al.* (2018) 'Lipid-Protein Interactions Are Unique Fingerprints for Membrane Proteins', *ACS Central Science*, 4(6), pp. 709–717. doi: 10.1021/acscentsci.8b00143.

D'Angelo, G. *et al.* (2008) 'The multiple roles of PtdIns(4)P - not just the precursor of PtdIns(4,5)P2', *Journal of Cell Science*, 121(12), pp. 1955–1963. doi: 10.1242/jcs.023630.

Davenport, J. R. *et al.* (2007) 'Conditional disruption of intraflagellar transport in adult mice leads to hyperphagia-induced obesity and slow onset cystic kidney disease', *Current Biology*, 17(18), pp. 1586–1594.

Denisov, G. *et al.* (1998) 'Binding of basic peptides to membranes produces lateral domains enriched in the acidic lipids phosphatidylserine and phosphatidylinositol 4,5-bisphosphate: An electrostatic model and experimental results', *Biophysical Journal*, 74(2 I), pp. 731–744. doi: 10.1016/S0006-3495(98)73998-0.

Dickson, E. J. *et al.* (2016) 'Dynamic formation of ER–PM junctions presents a lipid phosphatase to regulate phosphoinositides', *The Journal of Cell Biology*, 213(1), pp. 33–48. doi: 10.1083/jcb.201508106.

Dickson, E. J. and Hille, B. (2019) 'Understanding phosphoinositides: rare, dynamic, and essential membrane phospholipids', *Biochemical Journal*, 476(1), pp. 1–23. doi: 10.1042/BCJ20180022.

Epand, R. M. (2008) 'Proteins and cholesterol-rich domains', *Biochimica et Biophysica Acta*, 1778(7–8), pp. 1576–1582. doi: 10.1016/j.bbamem.2008.03.016.

Ferguson, K. M. *et al.* (1995) 'Structure of the High Affinity Complex of lnositol Trisphosphate with a Phospholipase C Pleckstrin Homology Domain', *Cell*, 83(6), pp. 1037–1046.

Fernández-Busnadiego, R., Saheki, Y. and De Camilli, P. (2015) 'Three-dimensional architecture of extended synaptotagmin-mediated endoplasmic reticulum–plasma membrane contact sites', *Proceedings of the National Academy of Sciences*, 112(16), pp. E2004–E2013. doi: 10.1073/pnas.1503191112.

Gamper, N. *et al.* (2004) 'Phosphatidylinositol 4,5-bisphosphate signals underlie receptor-specific Gq/11-mediated modulation of N-type Ca2+ channels', *The Journal of neuroscience*, 24(48), pp. 10980–10992. doi: 10.1523/JNEUROSCI.3869-04.2004.

Garcia, P. *et al.* (1995) 'The Pleckstrin Homology Domain of Phospholipase C-δ1 Binds with High Affinity to Phosphatidylinositol 4,5-Bisphosphate in Bilayer Membranes', *Biochemistry*, 34(49), pp. 16228–16234. doi: 10.1021/bi00049a039.

Gatta, A. T. *et al.* (2015) 'A new family of StART domain proteins at membrane contact sites has a role in ER-PM sterol transport', *eLife*, 4, p. e07253. doi: 10.7554/eLife.07253.

Giordano, F. *et al.* (2013) 'PI(4,5)P2 dependent and Ca2+ -regulated ER-plasma membrane interactions mediated by the extended-synaptotagmins', *Cell*, 153(7), pp. 1494–1509. doi: 10.1016/j.cell.2013.05.026.PI).

Golebiewska, U. *et al.* (2008) 'Diffusion Coefficient of Fluorescent Phosphatidylinositol 4,5-bisphosphate in the Plasma Membrane of Cells', *Molecular Biology of the Cell*, 19, pp. 1663–1669. doi: 10.1091/mbc.E07.

Golebiewska, U. *et al.* (2011) 'Evidence for a fence that impedes the diffusion of phosphatidylinositol 4,5-bisphosphate out of the forming phagosomes of macrophages', *Molecular Biology of the Cell*, 22(18), pp. 3498–3507. doi: 10.1091/mbc.E11-02-0114.

Hackelberg, S. and Oliver, D. (2018) 'Metabotropic Acetylcholine and Glutamate Receptors Mediate PI(4,5)P2 Depletion and Oscillations in Hippocampal CA1 Pyramidal Neurons in situ', *Scientific Reports*. Springer US, 8, p. 12987. doi: 10.1038/s41598-018-31322-8.

Halaszovich, C. R., Schreiber, D. N. and Oliver, D. (2009) 'Ci-VSP is a Depolarization-activated Phosphatidylinositol-4,5-bisphosphate and Phosphatidylinositol-3,4,5-trisphosphate 5'-Phosphatase', *Journal of Biological Chemistry*, 284(4), pp. 2106–2113. doi: 10.1074/jbc.M803543200.

Hammond, G. R. V., Schiavo, G. and Irvine, R. F. (2009) 'Immunocytochemical techniques reveal multiple, distinct cellular pools of PtdIns4P and PtdIns(4,5)P2', *Biochemical Journal*, 422(1), pp. 23–35. doi: 10.1042/BJ20090428.

Hammond, G. R. V. *et al.* (2012) 'PI4P and PI(4,5)P2 Are Essential But Independent Lipid Determinants of Membrane Identity', *Science*, 337(6095), pp. 727–730. doi: 10.1126/science.1222483.

Hammond, G. R. V., Machner, M. P. and Balla, T. (2014) 'A novel probe for phosphatidylinositol 4-phosphate reveals multiple pools beyond the Golgi', *Journal of Cell Biology*, 205(1), pp. 113–126. doi: 10.1083/jcb.201312072.

Hammond, G. R. V. and Balla, T. (2015) 'Polyphosphoinositide binding domains: key to inositol lipid biology', *Biochim Biophys Acta*, 1851(6), pp. 746–758. doi: 10.1016/j.bbalip.2015.02.013.Polyphosphoinositide.

Hammond, G.R.V. (2016) 'Does PtdIns(4,5)P2 concentrate so it can multi-task?', *Biochemical Society transactions* 44(1), pp. 228-233. doi: 10.1042/BST20150211.

He, K. *et al.* (2017) 'Dynamics of phosphoinositide conversion in clathrin-mediated endocytic traffic', *Nature*. Nature Publishing Group, 552(7685), pp. 410–414. doi: 10.1038/nature25146.

Herdman, C. and Moss, T. (2016) 'Extended-Synaptotagmins (E-Syts); the extended story', *Pharmacological Research*. Elsevier Ltd, 107, pp. 48–56. doi: 10.1016/j.phrs.2016.01.034.

Hirose, K. *et al.* (1999) 'Spatiotemporal Dynamics of Inositol 1,4,5-Trisphosphate That Underlies Complex Ca2+ Mobilization Patterns', *Science*, 284(5419), pp. 1527–1530. doi: 10.1126/science.284.5419.1527.

Hope, H. R. and Pike, L. J. (1996) 'Phosphoinositides and Phosphoinositide-utilizing Enzymes in Detergent-insoluble Lipid Domains', *Molecular biology of the cell*, 7(6), pp. 843–851.

Idevall-Hagren, O. *et al.* (2015) 'Triggered Ca2+ influx is required for extended synaptotagmin 1-induced ER-plasma membrane tethering.', *The EMBO journal*, 34(17), pp. 2291–2305. doi: 10.15252/embj.201591565.

Inoue, T. *et al.* (2005) 'An inducible translocation strategy to rapidly activate and inhibit small GTPase signaling pathways', *Nat Methods*, 2(6), pp. 415–418. doi: 10.1038/jid.2014.371.

Ishihara, H. *et al.* (1996) 'Cloning of cDNAs Encoding Two Isoforms of 68-kDa Type I Phosphatidylinositol-4-phosphate 5-Kinase', *Journal of Biological Chemistry*, 271(39), pp. 23611–23614. doi: 10.1074/jbc.271.39.23611.

Ishihara, H. *et al.* (1998) 'Type I phosphatidylinositol-4-phosphate 5-kinases. Cloning of the third isoform and deletion/substitution analysis of members of this novel lipid kinase family', *Journal of Biological Chemistry*, 273(15), pp. 8741–8748. doi: 10.1074/jbc.273.15.8741.

Itoh, T. *et al.* (2000) 'Autophosphorylation of Type I Phosphatidylinositol Phosphate Kinase Regulates Its Lipid Kinase Activity', *The Journal of biological chemistry*, 275(25), pp. 19389–19394. doi: 10.1074/jbc.M000426200.

Jarquin-Pardo, M. *et al.* (2007) 'Phosphatidic acid regulates the affinity of the murine phosphatidylinositol 4-phosphate 5-kinase-Ibeta for phosphatidylinositol-4-phosphate', *J. Cell Biochem.* 100, pp. 112-128. doi: 10.1002/jcb.21027.

Jenkins, G. H., Fisette, P. L. and Anderson, R. A. (1994) 'Type I phosphatidylinositol 4-phosphate 5-kinase isoforms are specifically stimulated by phosphatidic acid', *Journal of Biological Chemistry*, 269(15), pp. 11547–11554.

Johnson, C. M. and Rodgers, W. (2008) 'Spatial Segregaton of Phosphatidylinositol 4,5-Bisphosphate (PIP2) Signaling in Immune Cell Functions', *Immunol Endocr Metab Agents Med Chem.*, 8(4), pp. 349–357.

Kadamur, G. and Ross, E. M. (2013) 'Mammalian Phospholipase C', *Annu. Rev. Physiol.*, 75, pp. 127–154. doi: 10.1146/annurev-physiol-030212-183750.

Kaiser, S. E. *et al.* (2005) 'Structural Basis of FFAT Motif-Mediated ER Targeting', *Structure*, 13(7), pp. 1035–1045. doi: 10.1016/j.str.2005.04.010.

Kim, S. *et al.* (2013) 'The phosphatidylinositol-transfer protein Nir2 binds phosphatidic acid and positively regulates phosphoinositide signalling', *EMBO reports*. Nature Publishing

Group, 14(10), pp. 891–899. doi: 10.1038/embor.2013.113.

Kim, Y. J. *et al.* (2015) 'Phosphatidylinositol-Phosphatidic Acid Exchange by Nir2 at ER-PM Contact Sites Maintains Phosphoinositide Signaling Competence', *Developmental cell*. Elsevier Inc., 33(5), pp. 549–561. doi: 10.1016/j.devcel.2015.04.028.

Kleyn, P. W. *et al.* (1996) 'Identification and Characterization of the Mouse Obesity Gene tubby: A Member of a Novel Gene Family', *Cell*, 85, pp. 281–290.

Kwiatkowska, K. (2010) 'One lipid, multiple functions: How various pools of PI(4,5)P2 are created in the plasma membrane', *Cellular and Molecular Life Sciences*, 67(23), pp. 3927–3946. doi: 10.1007/s00018-010-0432-5.

Lees, J. A. *et al.* (2017) 'Lipid transport by TMEM24 at ER–plasma membrane contacts regulates pulsatile insulin secretion', *Science*, 355(6326), p. eaah6171. doi: 10.1126/science.aah6171.Lipid.

Leitner, M.G. *et al*. (2019) 'The N-terminal homology (ENTH) domain of Epsin 1 is a sensitive reporter of physiological PI(4,5)P_2 dynamics', *Biochim Biophys Acta Mol Cell Biol Lipids,* 1864(3)*,* pp. 433-442. doi: 10.1016/j.bbalip.2018.08.005.

Lemmon, M. A. *et al.* (1995) 'Specific and high-affinity binding of inositol phosphates to an isolated pleckstrin homology domain', *Proceedings of the National Academy of Sciences of the United States of America*, 92(23), pp. 10472–10476. doi: 10.1073/pnas.92.23.10472.

Lemmon, M. A. (2003) 'Phosphoinositide Recognition Domains', *Traffic*, 4(4), pp. 201–213. doi: 10.1034/j.1600-0854.2004.00071.x.

Lemmon, M. A. (2007) 'Pleckstrin Homology (PH) domains and phosphoinositides', *Biochem Soc Symp.*, 74, pp. 81–93. doi: 10.1042/BSS0740081.Pleckstrin.

Lev, S. *et al.* (1999) 'Identification of a Novel Family of Targets of PYK2 Related to Drosophila Retinal Degeneration B (rdgB) Protein', *Molecular and cellular biology*, 19(3), pp. 2278–2288.

Lev, S. *et al.* (2008) 'The VAP protein family : from cellular functions to motor neuron disease', *Trends in Cell Biology*, 18(6), pp. 282–290. doi: 10.1016/j.tcb.2008.03.006.

Levental, I. *et al.* (2009) 'Calcium-dependent lateral organization in phosphatidylinositol (4,5) bisphosphate (PIP2)- and cholesterol containing monolayers', *Biochemistry*, 48(34), pp. 8241–8248. doi: 10.1021/bi9007879.Calcium-dependent.

Levine, T. P. and Munro, S. (2002) 'Targeting of Golgi-Specific Pleckstrin Homology Domains Involves Both PtdIns 4-Kinase-Dependent and -Independent Components', *Current Biology*, 12(9), pp. 695–704.

Ling, K. *et al.* (2002) 'Type Iγ phosphatidylinositol phosphate kinase targets and regulates focal adhesions', *Nature*, 420(6911), pp. 89–93. doi: 10.1038/nature01082.

Lingwood, D. and Simons, K. (2010) 'Lipid Rafts As a Membrane-Organizing Principle', *Science*, 327(5961), pp. 46–50. doi: 10.1126/science.1174621.

Loewen, C. J. R., Roy, A. and Levine, T. P. (2003) 'A conserved ER targeting motif in three families of lipid binding proteins and in Opi1p binds VAP', *The EMBO journal*, 22(9), pp. 2025–2035.

Loijens, J. C. and Anderson, R. A. (1996) 'Type I Phosphatidylinositol-4-phosphate 5-Kinases Are Distinct Members of This Novel Lipid Kinase Family', *Journal of Biological Chemistry*, 271(51), pp. 32937–32943. doi: 10.1074/jbc.271.51.32937.

Loktev, A. V and Jackson, P. K. (2013) 'Neuropeptide Y Family Receptors Traffic via the Bardet-Biedl Syndrome Pathway to Signal in Neuronal Primary Cilia', *CellReports*. The Authors, 5, pp. 1316–1329. doi: 10.1016/j.celrep.2013.11.011.

Luik, R. M. *et al.* (2006) 'The elementary unit of store-operated Ca2+ entry: local activation of CRAC channels by STIM1 at ER–plasma membrane junctions', *The Journal of Cell Biology*, 174(6), pp. 815–825. doi: 10.1083/jcb.200604015.

Maléth, J. *et al.* (2014) 'Translocation between PI(4,5)P2-poor and PI(4,5)P2-rich microdomains during store depletion determines STIM1 conformation and Orai1 gating', *Nature communications*, 5, p. 5843. doi: 10.1038/ncomms6843.

Martin, T. F. J. (2001) 'PI(4,5)P2 regulation of surface membrane traffic', *Current Opinion in Cell Biology*, 13(4), pp. 493–499. doi: 10.1016/S0955-0674(00)00241-6.

McLaughlin, S. and Murray, D. (2005) 'Plasma membrane phosphoinositide organization by protein electrostatic', *Nature*, 483, pp. 605–611.

Min, S.-W., Chang, W.-P. and Südhof, T. C. (2007) 'E-Syts, a family of membranous Ca2+-sensor proteins with multiple C2 domains', *Proc Natl Acad Sci U S A*, 104(10), pp. 3823–3828. doi: 10.1073/pnas.0611725104.

Moritz, A.. *et al.* (1992) 'Phosphatidylinositol 4-kinase and phosphatidylinositol-4-phosphate 5-kinase from bovine brain membranes', *Methods Enzymol*. 209, pp. 202-211. doi: 10.1016/0076-6879(92)09024-w.

Morris, N. J. *et al.* (1999) 'Cloning and preliminary characterization of a 121 kDa protein with multiple predicted C2 domains', *Biochimica et Biophysica Acta*, 1431(2), pp. 525–530.

Mukhopadhyay, S. *et al.* (2010) 'TULP3 bridges the IFT-A complex and membrane phosphoinositides to promote trafficking of G protein-coupled receptors into primary cilia', *Genes and Development*, 24(19), pp. 2180–2193. doi: 10.1101/gad.1966210.

Mukhopadhyay, S. and Jackson, P. K. (2011) 'The tubby family proteins', *Genome biology*, 12(6), p. 225.

Murata, Y. *et al.* (2005) 'Phosphoinositide phosphatase activity coupled to an intrinsic voltage sensor', *Nature*, 435, pp. 1239–1243. doi: 10.1038/nature03650.

Nakatsu, F. *et al.* (2012) 'PtdIns4P synthesis by PI4KIIIα at the plasma membrane and its impact on plasma membrane identity', *Journal of Cell Biology*, 199(6), pp. 1003–1016. doi: 10.1083/jcb.201206095.

Oancea, E. *et al*. (2005) ‘Green fluorescent protein (GFP)-tagged cysteine-rich domains from protein kinase C as fluorescent indicators for diacylglycerol signaling in living cells‘, *Journal of Cell Biology,* 140(3), pp.485-498. doi: 10.1083/jcb.140.3.485.

Okeke, E. *et al.* (2016) ‘Endoplasmic reticulum–plasma membrane junctions: structure, function and dynamics’, *The Journal of physiology*, 594(11), pp. 2837–2847. doi: 10.1113/JP271142.

Orci, L. *et al.* (2009) ‘STIM1-induced precortical and cortical subdomains of the endoplasmic reticulum’, *Proc Natl Acad Sci U S A*, 106(46), pp. 19358–19362.

Owen, D. M. *et al.* (2012) ‘The lipid raft hypothesis revisited - New insights on raft composition and function from super-resolution fluorescence microscopy’, *BioEssays*, 34(9), pp. 739–747. doi: 10.1002/bies.201200044.

Di Paolo, G. *et al.* (2002) ‘Recruitment and regulation of phosphatidylinositol phosphate kinase type 1γ by the FERM domain of talin’, *Nature*, 420(6911), pp. 85–89. doi: 10.1038/nature01147.

Di Paolo, G. and De Camilli, P. (2006) ‘Phosphoinositides in cell regulation and membrane dynamics’, *Nature*, 443(7112), pp. 651–657. doi: 10.1038/nature05185.

Park, S. J., Itoh, T. and Takenawa, T. (2001) ‘Phosphatidylinositol 4-Phosphate 5-Kinase Type I Is Regulated through Phosphorylation Response by Extracellular Stimuli’, *The Journal of biological chemistry*, 276(7), pp. 4781–4787. doi: 10.1074/jbc.M010177200.

Pemberton, J. G. *et al.* (2020) ‘Defining the subcellular distribution and metabolic channeling of phosphatidylinositol’, *The Journal of cell biology*, 219(3). doi: 10.1083/jcb.201906130.

Pemberton, J. G., Kim, Y. J. and Balla, T. (2020) ‘Integrated regulation of the phosphatidylinositol cycle and phosphoinositide-driven lipid transport at ER-PM contact sites’, *Traffic*, 21(2), pp. 200–219. doi: 10.1111/tra.12709.

Petkovic, M. *et al.* (2014) ‘The SNARE Sec22b has a non-fusogenic function in plasma membrane expansion’, *Nature Cell Biology*, 16(5), pp. 434–444. doi: 10.1038/ncb2937.

Phillips, M. J. and Voeltz, G. K. (2016) ‘Structure and function of ER membrane contact sites with other organelles’, *Nat Rev Mol Cell Biol.*, 17(2), pp. 69–82. doi: 10.1038/nrm.2015.8.Structure.

Pike, L. J. (2006) ‘Rafts defined: a report on the Keystone symposium on lipid rafts and cell function’, *Journal of Lipid Research*, 47, pp. 1597–1598. doi: 10.1194/jlr.E600002-JLR200.

Pike, L. J. and Miller, J. M. (1998) ‘Cholesterol depletion delocalizes phosphatidylinositol bisphosphate and inhibits hormone-stimulated phosphatidylinositol turnover’, *Journal of Biological Chemistry*, 273(35), pp. 22298–22304. doi: 10.1074/jbc.273.35.22298.

Quinn, K. V., Behe, P. and Tinker, A. (2008) ‘Monitoring changes in membrane phosphatidylinositol 4,5-bisphosphate in living cells using a domain from the transcription factor tubby’, *The Journal of physiology*, 586(12), pp. 2855–2871. doi:

10.1113/jphysiol.2008.153791.

Saheki, Y. *et al.* (2016) 'Control of plasma membrane lipid homeostasis by the extended synaptotagmins', *Nature cell biology*, 18(5), pp. 504–15. doi: 10.1038/ncb3339.

Saheki, Y. and De Camilli, P. (2017) 'Endoplasmic Reticulum-Plasma Membrane Contact Sites', *Annu. Rev. Biochem.*, 86, pp. 659–684.

Sahoo, H. (2011) 'Förster resonance energy transfer - A spectroscopic nanoruler: Principle and applications', *Journal of Photochemistry and Photobiology C: Photochemistry Reviews*. Elsevier B.V., 12(1), pp. 20–30. doi: 10.1016/j.jphotochemrev.2011.05.001.

Santagata, S. *et al.* (2001) 'G-protein Signaling Through Tubby Proteins', *Science*, 292(5524), pp. 2041–2050. doi: 10.1126/science.1061233.

Schauder, C. M. *et al.* (2014) 'Structure of a lipid-bound extended synaptotagmin indicates a role in lipid transfer', *Nature*. Nature Publishing Group, 510(7506), pp. 552–555. doi: 10.1038/nature13269.

Schink, K. O., Tan, K.-W. and Stenmark, H. (2016) 'Phosphoinositides in Control of Membrane Dynamics', *Annu. Rev. Cell Dev. Biol.*, 32, pp. 143–171. doi: 10.1146/annurev-cellbio-111315-125349.

Sclip, A. *et al.* (2016) 'Extended Synaptotagmin (ESyt) Triple Knock-Out Mice Are Viable and Fertile without Obvious Endoplasmic Reticulum Dysfunction', *PLoS ONE*, 11(6), p. e0158295. doi: 10.1371/journal.pone.0158295.

Sezgin, E. and Schwille, P. (2011) 'Fluorescence Techniques to Study Lipid Dynamics', *Cold Spring Harbor perspectives in biology*, 3(11), p. a009803.

Sharma, S. *et al.* (2013) 'An siRNA screen for NFAT activation identifies septins as coordinators of store-operated Ca2+ entry', *Nature*. Nature Publishing Group, 499(7457), pp. 238–242. doi: 10.1038/nature12229.

Simons, K. and Sampaio, J. L. (2011) 'Membrane Organization and Lipid Rafts', *Cold Spring Harb Perspect Biol*, 3(10), p. a004697. doi: 10.1097/00019616-199311000-00013.

Stauffer, T. P., Ahn, S. and Meyer, T. (1998) 'Receptor-induced transient reduction in plasma membrane PtdIns(4 ,5)P2 concentration monitored in living cells', *Current Biology*, 8(6), pp. 343–346.

Stefan, C. J. *et al.* (2011) 'Osh proteins regulate phosphoinositide metabolism at ER-plasma membrane contact sites', *Cell*. Elsevier Inc., 144(3), pp. 389–401. doi: 10.1016/j.cell.2010.12.034.

Stubdal, H. *et al.* (2000) 'Targeted Deletion of the tub Mouse Obesity Gene Reveals that tubby Is a Loss-of-Function Mutation', *Molecular and cellular biology*, 20(3), pp. 878–882.

Suh, P.-G. *et al.* (2008) 'Multiple roles of phosphoinositide-specific phospholipase C isozymes', *BMB reports*, 41(6), pp. 415–434. doi: 10.5483/bmbrep.2008.41.6.415.

Sun, E. W. *et al.* (2019) 'Lipid transporter TMEM24/C2CD2L is a Ca 2+-regulated component

of ER–plasma membrane contacts in mammalian neurons', *Proceedings of the National Academy of Sciences of the United States of America*, 116(12), pp. 5775–5784. doi: 10.1073/pnas.1820156116.

Sun, X. *et al.* (2012) 'Tubby is required for trafficking G protein-coupled receptors to neuronal cilia', *Cilia*. Cilia, 1(1), p. 21. doi: 10.1186/2046-2530-1-21.

Szentpetery, Z. *et al.* (2009) 'Live cell imaging with protein domains capable of recognizing phosphatidylinositol 4,5-bisphosphate; a comparative study', *BMC cell biology*, 10, p. 67. doi: 10.1186/1471-2121-10-67.

Thallmair, V. *et al*. (2020a) 'A second PI(4,5)P_2 binding site determines PI(4,5)P_2 sensitivity of the tubby domain', bioRxiv 2020.09.23.309492.

Thallmair, V. *et al*. (2020b) 'Local PI(4,5)P_2 pool dynamics detected by the coincidence biosensor tubbyCT maintain the integrity of ER-PM junctions during PLC signaling', bioRxiv 2020.09.25.313403.

Traynor-Kaplan, A. *et al.* (2017) 'Fatty-acyl chain profiles of cellular phosphoinositides', *Biochim Biophys Acta*, 1862(5), pp. 513–522. doi: 10.1016/j.physbeh.2017.03.040.

Tremblay, M. G. *et al.* (2015) 'Extended Synaptotagmin Interaction with the Fibroblast Growth Factor Receptor Depends on Receptor Conformation, Not Catalytic Activity', *Journal of Biological Chemistry*, 290(26), pp. 16142–16156. doi: 10.1074/jbc.M115.656918.

Trimble, W. S. and Grinstein, S. (2015) 'Barriers to the free diffusion of proteins and lipids in the plasma membrane', *Journal of Cell Biology*, 208(3), pp. 259–271. doi: 10.1083/jcb.201410071.

Trivedi, D. and Padinjat, R. (2007) 'RdgB proteins: Functions in lipid homeostasis and signal transduction', *Biochimica et Biophysica Acta*, 1771(6), pp. 692–699. doi: 10.1016/j.bbalip.2007.04.014.

Várnai, P. and Balla, T. (1998) 'Visualization of phosphoinositides that bind pleckstrin homology domains: Calcium- and agonist-induced dynamic changes and relationship to myo-[3H]inositol-labeled phosphoinositide pools', *Journal of Cell Biology*, 143(2), pp. 501–510. doi: 10.1083/jcb.143.2.501.

Walsh, C. M. *et al.* (2010) 'Role of phosphoinositides in STIM1 dynamics and store-operated calcium entry', *Biochemical Journal*, 425(1), pp. 159–168. doi: 10.1042/BJ20090884.

Wang, J. and Richards, D. A. (2012) 'Segregation of PIP2 and PIP3 into distinct nanoscale regions within the plasma membrane', *Biology Open*, 1(9), pp. 857–862. doi: 10.1242/bio.20122071.

Wang, S.-Q. *et al.* (2001) 'Ca2+ signalling between single L-type Ca2+ channels and ryanodine receptors in heart cells', *Nature*, 410(6828), pp. 592–596.

Wang, S. Q. *et al.* (2004) 'The quantal nature of Ca2+ sparks and in situ operation of the ryanodine receptor array in cardiac cells', *Proc Natl Acad Sci U S A*, 101(11), pp. 3979–

3984.

Wang, Z. *et al.* (2009) ‘Adult Type 3 Adenylyl Cyclase – Deficient Mice Are Obese’, *PLoS ONE*, 4(9), p. e6979. doi: 10.1371/journal.pone.0006979.

West, M. *et al.* (2011) ‘A 3D analysis of yeast ER structure reveals how ER domains are organized by membrane curvature’, *The Journal of Cell Biology*, 193(2), pp. 333–346. doi: 10.1083/jcb.201011039.

Wilke, B. U. *et al.* (2014) ‘Diacylglycerol mediates regulation of TASK potassium channels by Gq-coupled receptors’, *Nature Communications*, 5, p. 5540. doi: 10.1038/ncomms6540.

Winks, J. S. *et al.* (2005) ‘Relationship between membrane phosphatidylinositol-4,5-bisphosphate and receptor-mediated inhibition of native neuronal M channels’, *The Journal of neuroscience*, 25(13), pp. 3400–3413. doi: 10.1523/JNEUROSCI.3231-04.2005.

Wu, H., Carvalho, P. and Voeltz, G. K. (2018) ‘Here, there, and everywhere: The importance of ER membrane contact sites’, *Science*, 361(6401), p. eaan5835. doi: 10.1126/science.aan5835.

Yagisawa, H. *et al.* (1994) ‘Expression and Characterization of an Inositol 1,4,5-Trisphosphate Binding Domain of Phosphatidylinositol-specific Phospholipase C-δ1’, *Journal of Biological Chemistry*, 269(31), pp. 20179–20188.

Yang, Y. R. *et al.* (2013) ‘The physiological roles of primary phospholipase C’, *Advances in Biological Regulation*, 53(3), pp. 232–241. doi: 10.1016/j.jbior.2013.08.003.

Zewe, J. P. *et al.* (2020) ‘Probing the subcellular distribution of phosphatidylinositol reveals a surprising lack at the plasma membrane’, *The Journal of cell biology*, 219(3). doi: 10.1083/jcb.201906127.

Zhang, S. L. *et al.* (2005) ‘STIM1 is a Ca2+ sensor that activates CRAC channels and migrates from the Ca2+ store to the plasma membrane’, *Nature*, 437(7060), pp. 902–905.

Zhang, Y. *et al.* (2020) ‘Hypothalamic extended synaptotagmin-3 contributes to the development of dietary obesity and related metabolic disorders’, *Proceedings of the National Academy of Sciences*, 117(33), pp. 20149–20158. doi: 10.1073/pnas.2004392117.

FIGURES

Figure 1.1: Phosphoinositide structure and interconversion 14
Figure 1.2: The PI cycle 17
Figure 1.3: ER-PM contact sites involved in lipid homeostasis 21
Figure 1.4: Activation of PLCβ activates Nir-mediated PI transfer at ER-PM contact sites 23
Figure 1.5: Structure of E-Syt1-3 24
Figure 1.6: Structure of Nir proteins 1-3 26

Figure 2.1: Scheme of subcloning procedure 35
Figure 2.2: Principle of performed co-immunoprecipitation 42
Figure 2.3: Principle of Fluorescence Resonance Energy Transfer 45
Figure 2.4: Background fluorescences 47
Figure 2.5: CFP bleed through and YFP false excitation 48
Figure 2.6: Principle of TIRF imaging 50
Figure 2.7: Principle of cluster detection algorithm 52

Figure 3.1: FRET between PI(4,5)P_2 sensors 56
Figure 3.2: PI(4,5)P_2 sensor dynamics upon PI(4,5)P_2 depletion 58
Figure 3.3: Co-localization of tubbyCT with the PM marker lyn11 and the PI(4,5)P_2 sensors PLCδ1-PH and Epsin1 ENTH 60
Figure 3.4: PLCβ-induced tubbyCT dynamics in clustered and non-clustered PM regions 62
Figure 3.5: Probing DAG and PI(4,5)P_2 dependence of tubbyCT PM recruitment 64
Figure 3.6: Co-localization of tubbyCT with ER-PM junction proteins 66
Figure 3.7: Co-localization of PLCδ1-PH with ER-PM junction proteins 68
Figure 3.8: Co-localization of E-Syts with each other 69
Figure 3.9: Co-localization of tubbyCT with ER-PM junction proteins in presence of E-Syt3 71
Figure 3.10: Probing tubbyCT-E-Syt3 interaction 72
Figure 3.11: Mapping the region in E-Syt3 interacting with tubbyCT 75
Figure 3.12: Probing the influence of PI(4,5)P_2 on tubbyCT localization to ER-PM junctions 77
Figure 3.13: Co-expression of tubbyCT KR330/332AA mutant with E-Syts 79
Figure 3.14: PI(4,5)P_2 sensor dynamics at tubbyCT clusters 81
Figure 3.15: PI4P sensor dynamics at tubbyCT clusters 82
Figure 3.16: Influence of PI4K inhibition on PLCβ-induced E-Syt dynamics 84

Figure 3.17: Comparison of E-Syt dynamics and gene expression in CHO and COS-7 cells 86
Figure 3.18: Influence of E-Syt3 over-expression on tubbyCT dynamics 89
Figure 3.19: Influence of Nir2/3 on tubbyCT cluster formation and dynamics 90
Figure 3.20: Tubby full-length and TULP3 localization and dynamics 92
Figure 3.21: Influence of tubby over-expression on PLCβ-induced E-Syt dynamics 93

TABLES

Table 1: Used expression vectors 34
Table 2: Protocols of individual subcloning steps 36
Table 3: PCR protocol used for gene-specific cDNA amplification 39
Table 4: Gene-specific primer and nested primer pairs used for cDNA amplification 40
Table 5: Gene-specific CHO cell E-Syt3 primer and nested primer pairs 41
Table 6: Gel and buffer recipes for SDS-PAGE and Western Blotting 44

DANKSAGUNG

Ganz herzlich möchte ich mich bei allen bedanken die mich bei der Anfertigung meiner Doktorarbeit unterstützt haben.

Allen voran bedanke ich mich bei Dominik Oliver, für die gute Betreuung, die stets offene Tür, die vielen Diskussionen und vor allem auch für die Freiheit eigenen Ideen nachzugehen. Danke auch dafür, dass du nie ein kritisches Wort darüber verloren hast, wenn ich Yaël früher aus der Kita holen musste oder sie krank war.

Mein Dank gilt auch der gesamten Arbeitsgruppe für die stete Hilfe, die vielen Anregungen, guten Gespräche und einfach für die schöne Zeit. Besonders bedanken möchte ich mich bei Michael Leitner und Christian Halaszovich für die Unterstützung bei technischen Fragen, bei Gisela Fischer und Eva Naudascher für die Hilfe in der Molekularbiologie und bei Olga Ebers und Nesli Özen für die Zellkultur. Mein besonderer Dank geht auch an Lea Schultz, die mir in dem letzten Jahr eine super studentische Hilfskraft war und mir bei den letzten Experimenten sehr geholfen hat.

Natürlich möchte ich auch meiner Familie ein großes Dankeschön sagen. Meinen Eltern, die mir stets ein stabiler Anker im Leben waren und sind, meinem Bruder Sebastian für die MD Simulationen und die gute Zusammenarbeit, meinem Mann Christian für die vielen kritischen (projektbezogenen) Fragen, das Mitdenken und die vielen Ideen für weitere Experimente. Und meinen beiden Töchtern Yaël und Laura möchte ich danken, dass sie, wenn ich arbeiten musste, so oft ruhig neben mir gespielt haben und mich dann wenn ich fertig war (und manchmal auch schon früher) sofort auf andere Gedanken gebracht haben.

LEBENSLAUF

Veronika Katharina Thallmair
Zum Feldlager 126
34128 Kassel

geboren am 12.11.1986 in München

November 2016 – Oktober 2020	Mitglied im Graduiertenkolleg GRK2213 ‚Membrane Plasticity in Tissue Development and Remodeling‘, Philipps-Universität Marburg
April 2013 – Oktober 2020	Doktorandin in der Arbeitsgruppe Neurophysiologie (Prof. Oliver), Institut für Physiologie und Pathophysiologie, Philipps-Universität Marburg
Oktober 2012 – Januar 2013	Wissenschaftliche Mitarbeiterin in der Arbeitsgruppe Ott, Institut für Genetik, Ludwig-Maximilians-Universität München
Oktober 2009 – September 2012	Stipendium des Max-Weber-Programms der Studienstiftung des deutschen Volkes
Oktober 2010 – September 2012	Master Studium der Biologie, Ludwig-Maximilians-Universität München
Oktober 2007 – August 2010	Bachelor Studium der Biologie, Ludwig-Maximilians-Universität München
Oktober 1997 – Juni 2006	Graf-Rasso-Gymnasium Fürstenfeldbruck

PUBLIKATIONEN

Thallmair, V., Schultz, L., Evers, S., Goecke, C., Thallmair, S., Leitner, M.G., Oliver, D. (2020) ‘Local PI(4,5)P_2 pool dynamics detected by the coincidence biosensor tubbyCT maintain the integrity of ER-PM junctions during PLC signaling‘, bioRxiv 2020.09.25.313403.

Thallmair, V., Schultz, L., Marrink, S.J., Oliver, D., Thallmair, S. (2020) ‘A second PI(4,5)P_2 binding site determines PI(4,5)P_2 sensitivity of the tubby domain‘, bioRxiv 2020.09.23.309492.

Leitner, M.G., **Thallmair, V.**, Wilke, B.U., Neubert, V., Kronimus, Y., Halaszovich, C.R., Oliver, D. (2019) ‘The N-terminal homology (ENTH) domain of Epsin 1 is a sensitive reporter of physiological PI(4,5)P_2 dynamics’, *BBA - Mol Cell Biol Lipids* 1864(3), pp.433-442. doi: 10.1016/j.bbalip.2018.08.005.

Mavrantoni, A., **Thallmair, V.**, Leitner, M.G., Schreiber, D.N., Oliver, D., Halaszovich, C.R. (2015) ‘A method to control phosphoinositides and to analyze PTEN function in living cells using voltage sensitive phosphatases’, *Front Pharmacol* 6, pp.68. doi: 10.3389/fphar.2015.00068.

Rjasanow, A., Leitner, M.G., **Thallmair, V.**, Halaszovich, C.R., Oliver, D. (2015) ‘Ion channel regulation by phosphoinositides analyzed with VSPs – PI(4,5)P_2 affinity, phosphoinositide selectivity, and PI(4,5)P_2 pool accessibility’, *Front Pharmacol* 6, pp.127. doi: 10.3389/fphar.2015.00127.

VERZEICHNIS DER AKADEMISCHEN LEHRER

Meine akademischen Lehrer waren die Damen und Herren in …

… München (Deutschland)

Boshart, Böttger, Brachmann, Cremer, Döbbeler, Facher, Fischer, Grupe, Haszprunar, Heubl, Jung H., Jung K., Laforsch, Lahaye, Leibold, Leister, Leonhardt, Marín, Nickelsen, Ott, Parniske, Renner, Soll, Schüssler, Wanner, Weiß

… Wien (Österreich)

Gosch, Stich

… Sheffield (UK)

Whitfield

… Marburg (Deutschland)

Oliver

EHRENWÖRTLICHE ERKLÄRUNG

Ich erkläre ehrenwörtlich, dass ich die dem Fachbereich Medizin Marburg zur Promotionsprüfung eingereichte Arbeit mit dem Titel ‚**The coincidence biosensor tubbyCT reveals local phosphatidylinositol-4,5-bisphosphate synthesis at endoplasmic reticulum-plasma membrane junctions‘** im Institut für Physiologie und Pathophysiologie unter Leitung von Herrn Prof. Dr. Dominik Oliver mit Unterstützung durch Herrn Prof. Dr. Dominik Oliver ohne sonstige Hilfe selbst durchgeführt und bei der Abfassung der Arbeit keine anderen als die in der Dissertation aufgeführten Hilfsmittel benutzt habe. Ich habe bisher an keinem in- oder ausländischen Medizinischen Fachbereich ein Gesuch um Zulassung zur Promotion eingereicht, noch die vorliegende oder eine andere Arbeit als Dissertation vorgelegt.
Ich versichere, dass ich sämtliche wörtlichen oder sinngemäßen Übernahmen und Zitate kenntlich gemacht habe. Mit dem Einsatz von Software zur Erkennung von Plagiaten bin ich einverstanden.
Teile der Arbeit wurden mit dem Titel ‚Local PI(4,5)P_2 pool dynamics detected by the coincidence biosensor tubbyCT maintain the integrity of ER-PM junctions during PLC signaling‘ im BioRxiv (2020.09.25.313403) veröffentlicht.

Marburg, 28.09.2020

Veronika Thallmair

Die Hinweise zur Erkennung von Plagiaten habe ich zur Kenntnis genommen.

Marburg, 28.09.2020

Prof. Dr. Dominik Oliver